MULTI SCALE SIMULATIONS FOR EFFICIENT MULTI-STEP REACTION CASCADES

By

Kanchan Suklal Chavan

A DISSERTATION

Submitted to
Michigan State University
in partial fulfillment of the requirements
for the degree of

Chemical Engineering—Doctor of Philosophy

2020

ABSTRACT

MULTI SCALE SIMULATIONS FOR EFFICIENT MULTI-STEP REACTION CASCADES

By

Kanchan Suklal Chavan

Efficient multi-step reaction cascades are vital for the pharmaceutical industry and electrochemical devices. Conventionally, one-pot synthesis has been used to carry out such multi-step reaction cascades, which have poor selectivity and yield due to lack of control over the transport of chemical species and kinetics in the system. Therefore, it is desirable to engineer an integrated catalytic system with highly selective catalysts and efficient transport mechanisms.

Nature has developed highly efficient transport mechanisms via strategic architectures that use electrostatic interactions, physical confinement, and swing arm techniques to reduce diffusional losses. Such controlled transport is known as 'substrate channeling'. These natural mechanisms provide essential clues to design novel catalytic platforms. The physical confinement of an intermediate pathway has the potential for 100% intermediate transport. This provides motivation to study the transport in nanoscale confinement. Maximum intermediate retention with minimum bulk access is a key to obtain maximum channeling efficiency.

In this work, we study the effect of nanoscale confinement using continuum modeling and molecular dynamics approaches. Continuum modeling of tunnel structures that have active sites confined within shows that increasing confined distance between active site and bulk improves product yield significantly in a kinetically limited system. Molecular dynamics study of interactions between intermediate and tunnel geometry

demonstrates that Knudsen diffusion lowers the effective diffusivity of the intermediate. The orientation of solvent molecules inside the tunnel plays a major role in enhancing Knudsen diffusion inside the tunnel. Finally, to increase the intermediate retention, charged molecules may be introduced at the tunnel ends, and retention is highly sensitive to the polarity of the intermediates.

Further, we studied existing integrated catalytic platforms for carbon dioxide reduction reaction (CO_2RR) and glycerol oxidation reaction cascades. Microkinetic modeling of CO_2RR combined with the density functional theory (DFT) technique demonstrates that CO_2RR dominates at lower potential with a high surface coverage of carboxylate, a stable intermediate. Nudged elastic band theory calculations of transition states were used to define the transition state of each step of the reaction.

A one-dimensional continuum model study of the glycerol oxidation cascade reveals the sensitivity of convective forces in the system on the intermediate transport. Overall, in this work, various aspects of transport and kinetics of the multi-step reaction cascades were studied computationally. This work acts as a primary guide to design novel integrated catalytic platforms for efficient multi-step reaction cascades.

Dedicated to Aai and Papa.

ACKNOWLEDGMENTS

I want to express my sincere gratitude to my advisor, Dr. Scott Calabrese Barton, for his constant support and guidance throughout my Ph.D. journey. He encouraged me to think creatively and gave me the freedom to explore computational methods in the field of energy and provided the resources required along the way.

I am thankful for the funding support from Army research office MURI (#W911NF1410263) via the University of Utah. I would like to thank all of my Ph.D. committee members, Dr. Tim Hogan, Dr. Alexei Bazavov, and Dr. David Hickey to provide me their expert comments and valuable feedback on my work. I am also grateful to the Army research office for funding my work through Dr. Shelly Minteer at the University of Utah. I am thankful to our collaborators, Plamen Atanassov and Tristan Asset from the University of Irvine, California, and Nalin Andersen and Ivana Matanovic from the University of New Mexico. Their constant feedback and frequent exchange of ideas helped me to shape my work.

I express my gratitude to my lab-mates – Alex, Yuanchao, Manali, Yan, and Jim, and all the members of the Chemical Engineering and Material Science department at Michigan State University. Big cheers to my CHEMS friends and family – Hongkang, Natalia, David, Gouree, Tridip Da, Aseel, Neda, Iman, Sanket. I am very thankful and feel lucky to have found amazing friends at Michigan State University who kept me sane in this crazy journey.

Big shout out to Mayank, Sabyasachi, Sap Da, Aritra, Preetam, and Sayli for all the support, love, and care. I collected beautiful gems as I was growing up from school (Ashu, Prachi, Radha, Neha, and Madhura), Undergrad (Shabdiki, Deeksha, Kruti, Rohit, Abhirag), who encouraged me to take bold steps and fly high. Thank you, and I love you guys so much.

Most importantly, I would like to thank Aai, papa, Didi, Pranav, and Utsavi for the constant love and support from thousands of miles away. Thank you for everything!

TABLE OF CONTENTS

LIST OF TABLES

LIST OF FIGURES

Chapter 1

Introduction

Designing efficient multi-step reaction cascades can directly benefit the manufacturing process of advanced materials, specialty chemicals, and energy conversion/storage applications such as biofuel cells. A conventional method to carry out such a successive reaction scheme involves stepwise batch or continuous reactor operation with intermediate purification and separation processes. With possible process optimization techniques one can either optimize process parameters to increase energy efficiency and therefore reduce operational cost or reduce the number of reaction steps with the help of advanced research to reduce capital cost. Reduction in the number of reaction steps to a single reaction step requires a common window of operating parameters that are difficult to achieve.

One can design a multifunctional catalyst, or tandem catalyst, to perform multi-step, successive chemical reactions in a single reactor, known as one-pot synthesis.[1] Until now, chemists have successfully carried out alcohol oxidation and methylenation, synthesis of ketones from aldehydes, asymmetric Aza-Claisen reaction and olefin metathesis, benzofuran synthesis, oxidative ketonylation, and Diels–Alder reaction by using mono/multi-functional catalyst.[2,3] Figure 1.1. depicts the one-pot synthesis of a three-step reaction to produce dihydroquinolinone using multi-metal catalysts (Rh/Pd/Cu).[4] However, these syntheses are largely carried out in batch reactor mode, without extensive optimization, and could be further improved by increased control of intermediate transport at the nanoscale.[2]

An efficient multi-step reaction cascade features high yield and selectivity of desired intermediates/products with little to no requirement for separation or purification. Such reaction cascades require precise control over the transport of intermediates and highly active catalytic sites. Figure 1.2 shows an example of an integrated catalytic platform consist of a strategic organization of different types of catalysts, such as a molecular catalyst on a DNA scaffold, that also facilitates transport between active sites. This conceptual design is for a two-step oxidation reaction of tartronic acid to oxalic acid with an intermediate, mesoxalic acid. TEMPO, a molecular catalyst, and RuPt nanoparticles are the two catalysts anchored on a DNA scaffold that ensures controlled intermediate transport between the sites.[5,6] To design such a novel catalytic platform, a better understanding of the reaction mechanism, nature of intermediates, transport between active sites, and the contribution of the kinetics of the reaction on the overall multi-step reaction cascade is required.[2]

The challenges to engineering multi-step reaction cascades are to 1) find an efficient intermediate transport mechanism between sites, and 2) design an efficient and selective

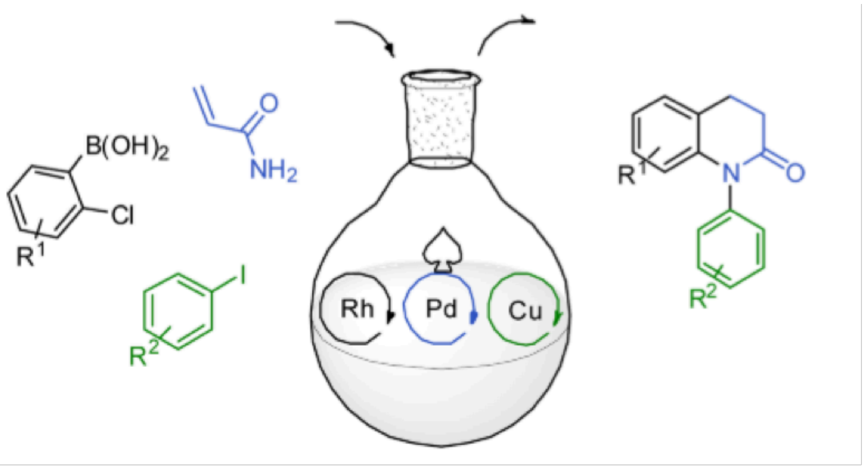

Figure 1.1 A one-pot synthesis of dihydroquinolinones using a Rh/Pd/Cu catalytic system.[4]

catalyst. In this dissertation, we try to meet both challenges by understanding existing transport mechanisms for a natural reaction cascades and by studying the mechanistic behavior of a catalyst for a multi-step carbon dioxide reduction reaction.

1.1 Substrate Channeling Mechanisms for efficient intermediate transport

A living cell carries out thousands to millions of reactions per second, via metabolic pathways comprised of sequential reactions. These reaction cascades achieve high yield by avoiding equilibration of intermediates in bulk solution.[7] Understanding of natural multi-step reaction cascades can provide essential clues to develop novel catalytic systems to enhance the yield of multi-step reaction cascades.[8]

Biological catalysts in sequential reactions often incorporate mechanisms to transport intermediates between sites without diffusing into the bulk. Such substrate channeling mechanisms isolate intermediates from competing reactions, avoid unfavorable equilibria and bulk reactions,[7] reduce time constants, *e.g.* lag time to reach steady-state,[9] and avoid high energetics of substrate dissolution.[10] These enzymes sterically restrict intermediate exposure to the bulk by forming a molecular tunnel between sites[11–15] or spatially organizing themselves and covalently binding intermediate to swing arms on the

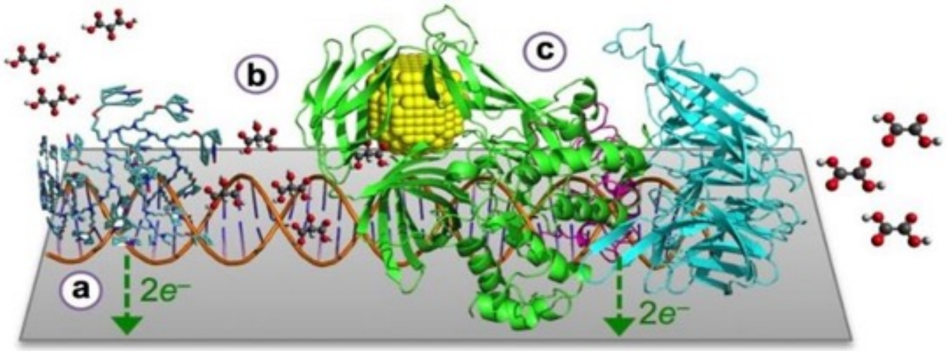

Figure 1.2 An example of integrated catalytic platform for oxidation of Tartronic acid to oxalic acid. a) Tartronic acid oxidation to mesoxalic acid at TEMPO catalyst. b) Facilitated transport of mesoxalic acid along the DNA scaffold. c) oxidation of mesoxalic acid to oxalic acid via catalysis by PtRu nanoparticle.

pathway.[16–18] In some enzymes, a reaction intermediate electrostatically interacts with enzyme surface to reduce bulk exposure, known as electrostatic channeling.[10,19–22] These mechanisms are discussed further in this chapter.

1.1.1 Molecular tunneling

In this type of substrate channeling, two sites are connected through a tunnel, built with the molecular assembly around the path. A well-known example of substrate

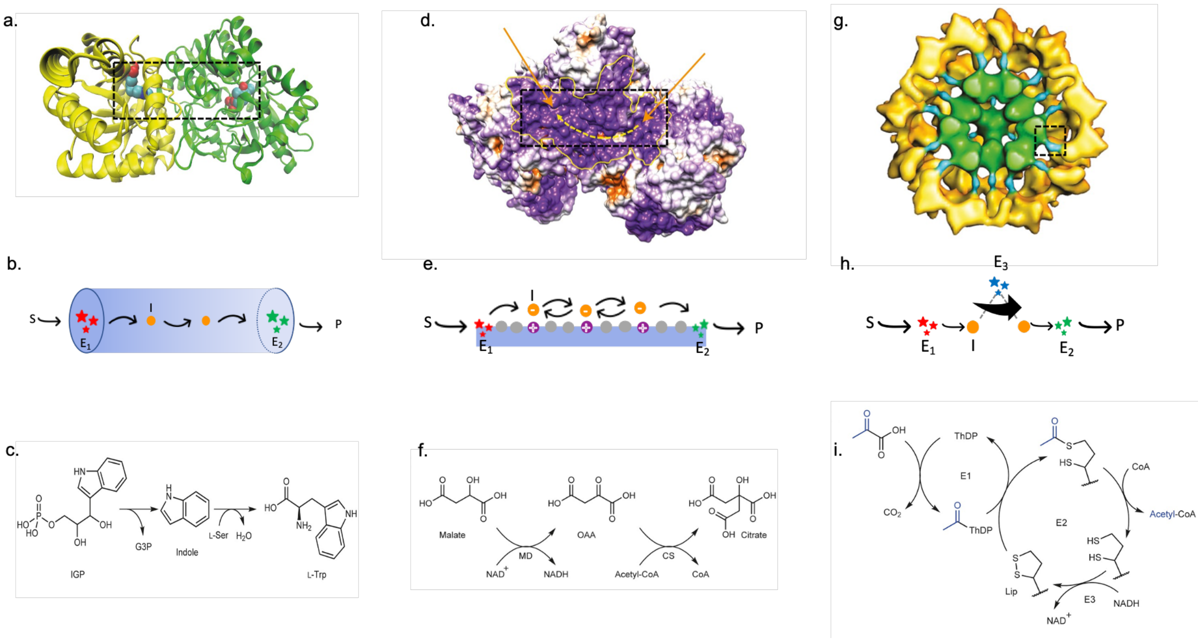

Figure 1.3 Substrate channeling Mechanisms. a) The crystal structure of Tryptophan Synthase. Indole molecule is shown inside the tunnel. α and β subunits are shown in yellow and green colors, respectively. b) Simplified and generalized molecular tunneling mechanism representation. c) Reaction cascade of L-tryptophan synthesis from Indole-3-glyceraldehyde-phosphate (IGP) via indole intermediate. d) The crystal structure of malate dehydrogenase (MD)- citrate synthase (CS) within the tricarboxylic acid (TCA) cycle metabolon. Purple, orange and white color shows positive, negative and neutral charged surface respectively. Dashed yellow lines shows approximate intermediates pathway between two enzymes. e) simplified and generalized electrostatic channeling mechanism representation. f) Reaction cascade of citrate formation from malate via oxaloacetate intermediate. g) The crystal structure of eukaryotic pyruvate dehydrogenase complex. E1 and E2 enzymes are shown in yellow and green colored respectively. Both enzymes are connected by linkers shown in blue color. h) simplified and generalized representation of substrate channeling via swing arm mechanism. Above panel is reproduced from Wheeldon et.al.[8]

channeling through a molecular tunnel is tryptophan synthase. Tryptophan synthase (TS) catalyzes the reaction of indole-3-glycerol phosphate to produce L-tryptophan with indole as the intermediate.[23] X-ray crystallography of tryptophan synthase suggests that two sites, α, and β subunits, are separated by a 25 Å long hydrophobic tunnel, revealing the effective transport of indole from one site to another. (Figure 1.3 a-c)

Similarly, carbonyl phosphate synthases (CPS) assemble carbonyl phosphate by the four sequential reactions of bicarbonate, glutamine, and 2 molecules of MgATP producing glutamate, phosphate, and 2 molecules of MgADP. CPS includs a 96 Å long tunnel between the substrate consumption site to the ultimate product formation site.[15] Glutamine phosphoribosyl-pyrophosphate amidotransferase catalyzes the reaction between glutamine and phosphoribosyl-pyrophosphate (PRPP) by transporting ammonia from glutamine domain to PRPP domain through 20 Å long hydrophobic tunnel to form glutamate, phosphoribosyl-amine (PRA), and pyrophosphate.[24] A molecular tunnel between aldolase-dehydrogenase complex is also observed.[25,26] Synchronously, all the examples of molecular tunneling found in nature show potential for the design of controlled diffusion and flux of the intermediates with little to no exposure to the bulk.

1.1.2 Electrostatic Channeling

Electrostatic channeling guides charged intermediate from one site to another through electrostatic interaction with an oppositely charged surface. There are two very well-established examples found in the literature - bifunctional thymidylate synthase-dihydrofolate reductase (TS-DHFR) and the TCA cycle enzymes, malate dehydrogenase (MD) and citrate synthase (CS). (Figure 1.3 d-f)

In bifunctional TS-DHFR enzyme, the TS active site produces negatively charged dihydrofolate (FH_2) intermediate and DHFR active site consumes FH_2.[27] FH_2, carrying -2 formal charge, transports to DHFR, which is ~40Å apart from TS, with the guidance of γ-glutamate linkers, each carrying +1 charge, present in the interior of the protein.[28] FH_2 transfer shows strong ionic-strength dependence and reveals the electrostatic highway mechanism.[28]

Similarly, channeling of oxaloacetate, produced during the tricarboxylic acid (TCA) cycle at malate dehydrogenase (MD), to the citrate synthase (CS) where it gets converted into citrate, also shows electrostatic channeling mechanism.[29] Electrostatically guided mechanisms are effective only for charged intermediates, and the intermediates pathway is exposed to the bulk hence increasing the probability of diffusional losses.

1.1.3 Spatial Organization and Covalent Bonding

The formation of a functional supermolecular complex, or “metabolon”, is often observed in metabolic pathways for channeling of intermediates. Metabolon formation is initiated due to the presence of membrane-bound proteins, and propagates because of specific interactions between soluble enzymes.[30] In *E. coli*, the pyruvate dehydrogenase complex, comprising three enzymes E_1, E_2, and E_3, catalyzes the conversion of pyruvate to acetyl coenzyme-A. (Figure 1.3 g-i) The E_2 enzyme is symmetrically arranged in the core of an octahedrally shaped complex, whereas E_1 and E_3 are arranged on the outer surface. In this three-step sequential reaction cascade, decarboxylation of pyruvate to the acetyl group is catalyzed by E_1 and the acetyl group is transferred to the lipoamide swing arm of E_2. An acetyl moiety is then transferred to free enzyme, CoASH, and produces Acetyl-Co-A. E_3 reactivates the lipoamine swing arm and deprotonates NADH.[16,31] Intermediates produced in fatty acid synthase and polyketide synthases, get attached to acyl carrier proteins, which channel in the metabolic pathway because of protein-protein interactions.[8] Protein-protein interaction is anticipated as the mode of substrate channeling in 10-step, 6-enzymes catalyzed synthesis of Purines in the living cell.[32]

From the above examples, it is found that intermediates can be transferred by covalent bonding with the enzymes in an assembled architecture. Also, channeling of intermediates due to protein-protein interactions is independent of electronic charges of intermediate and shows bounded diffusion to enhance the transfer efficiency of substrate channeling.[8]

1.2 Recent Developments

As substrate channeling mechanisms reveal mechanistic information, many researchers took inspiration to artificially synthesize these assemblies. In the past decade,

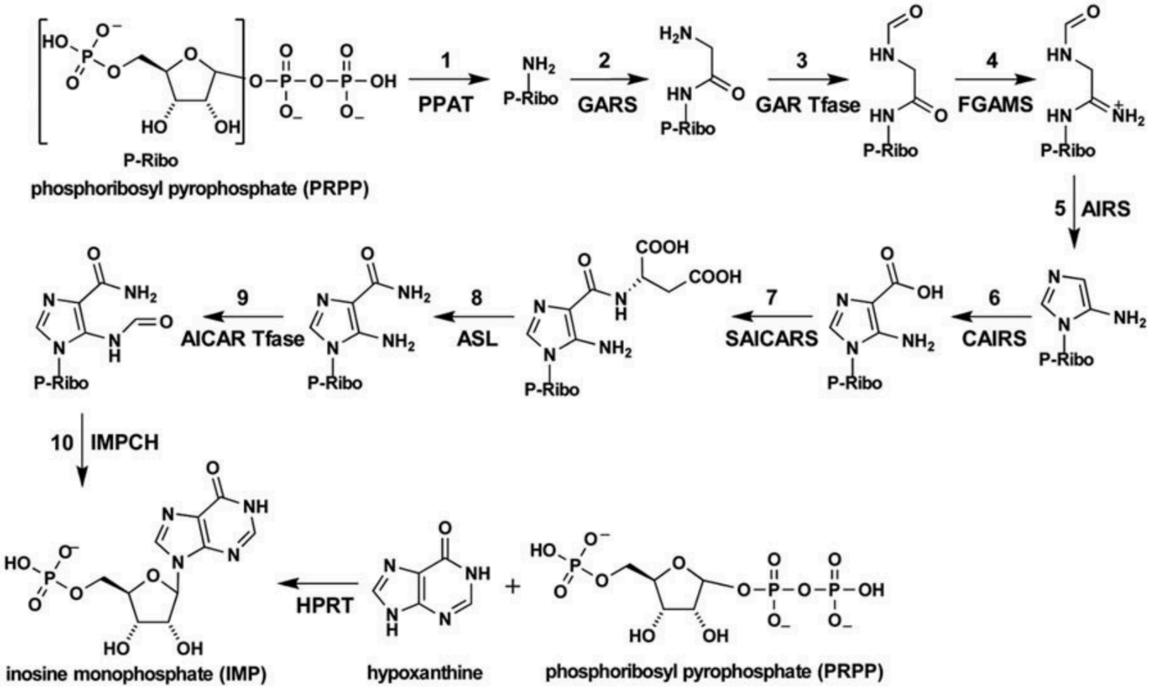

Figure 1.4 10 step chemical reaction of inosine monophosphate (IMP) formation from phosphoribosyl pyrophosphate (PRPP) in eukaryotic living cell.[32]

multi-functional nanostructured catalysts,[33] proteins,[34] polymers,[35] and nucleic acid scaffolds[36] have been engineered to co-localize and assemble enzymes to increase the overall catalytic efficiency of multistep reaction cascades. Examples of such architectures are provided in this section.

Channeling by proximity, in which two sites are positioned close to each other, is the conceptually simplest form. Proximity channeling has been studied experimentally by anchoring glucose oxidase-horseradish peroxidase (GOx-HRP) conjugates on a DNA scaffold,[36–38] by enzyme fusion,[39] and by enzyme crosslinking GOx-HRP.[40] (Figure 1.4)

A chemical swing arm mechanism is used for substrate channeling using a DNA scaffold. A two-step reaction is modeled and coupled with DNA nanostructure, in which glucose-6-phosphate dehydrogenase (G6pDH) and malate dehydrogenase (MDH) are

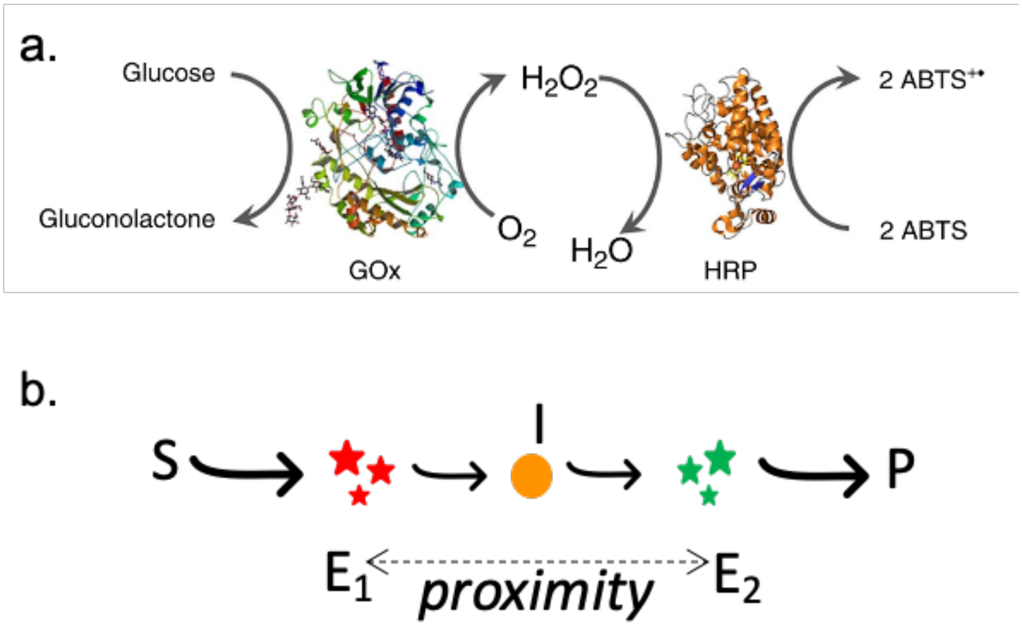

Figure 1.5 a) A schematic of glucose oxidase-horseradish peroxidase (GOx-HRP) reaction cascade.[40] b) Generalized and simplified representation of substrate channeling mechanism by proximity(Adapted from Wheeldon et.al.[8]

assembled spatially on DNA scaffold. NAD^+ functionalized swing-arm strand is assembled between both enzymes for reduction and oxidation of NADH, respectively.[38]

Protein scaffolds are prepared using cohesive docking in protein-protein interactions to illustrate three-step reaction cascade.[41] Triosephosphate isomerase, aldolase and fructose 1,6- bisphosphatase catalyzes the conversion of glyceraldehyde-3-phosphate (G3P) to dihydroxyacetone phosphate (DHAP), aldol condensation of G3P and DHAP to fructose-1,6-bisphosphate (F16P), F16P to fructose-6-phosphate respectively, in glycolysis and gluconeogenesis pathway. The result of this protein scaffolding shows an increased reaction rate at the minimum usage amount of enzyme and also, metabolite degradation is prevented.

Multi-step reaction cascade of GOx/HRP enzyme coupling is designed on the backbone of polymer also called polymersome.[42,43] In this cascade, GOx is assembled at the core, and HRP is assembled on the outer surface of the polymer. Co-localization and positional assembly on the polymer backbone resulted in a sevenfold increase in the initial enzymatic activity, which was calculated when the GOx/HRP enzyme couple was placed inside the polymer.

Core–shell Pd@IRMOF-3 nanostructures have been synthesized for two-step reaction cascade for the production of 2-(4-aminobenzylidene) - malononitrile by Knoevenagel condensation of 4-nitrobenzaldehyde and produces intermediate 2-(4-nitrobenzylidene) malononitrile.[44] Intermediate diffusion is controlled by the metal framework and enhanced catalytic efficiency is observed. Similar core-shell nanostructures for deprotonation and condensation reaction are designed using acid-functional groups in core and basic-functional groups in the silica shell. Once aldehyde is diffused in the core through silica pores, the reaction occurs on the acid-core and carbonyl intermediate is produced, which then condenses on the amine-functionalized shell.[45]

Polymersomes and core-shell structures are the examples of compartmentalization where transport of intermediates is confined by the positional assembly of active sites. Although the transport of intermediate is confined in compartmentalization techniques, it was aimed to create the positional assembly of active sites and intermolecular tunnels mimicry was not considered.

With the help of advanced fabrication techniques, nano-scaled inter-enzyme tunnels were fabricated by using self-assembled DNA and anodic aluminum oxide membranes.[36,46] Channeling mechanisms were further modeled using different simulation techniques to set the design rules for artificial integrated catalytic platforms.

1.3 Simulation Approach I

Chemical processes modeling enables detailed understanding of the phenomena and provides strong arguments to predict the outcome of the processes. With increasing computational capabilities, quantifying the macroscopic phenomena of chemical processes at different time and length scale has improved our understanding of the mechanisms and prediction accuracy of the models. Figure 1.6 shows existing simulation techniques at different length and time scale.[47]

1.3.1 Continuum Modeling

Continuum theory ignores the effect of atomic and molecular interactions on the properties of the body so that if a body is divided into infinitesimal elements, each element possesses same property as the bulk. Such models are highly accurate at length scales far

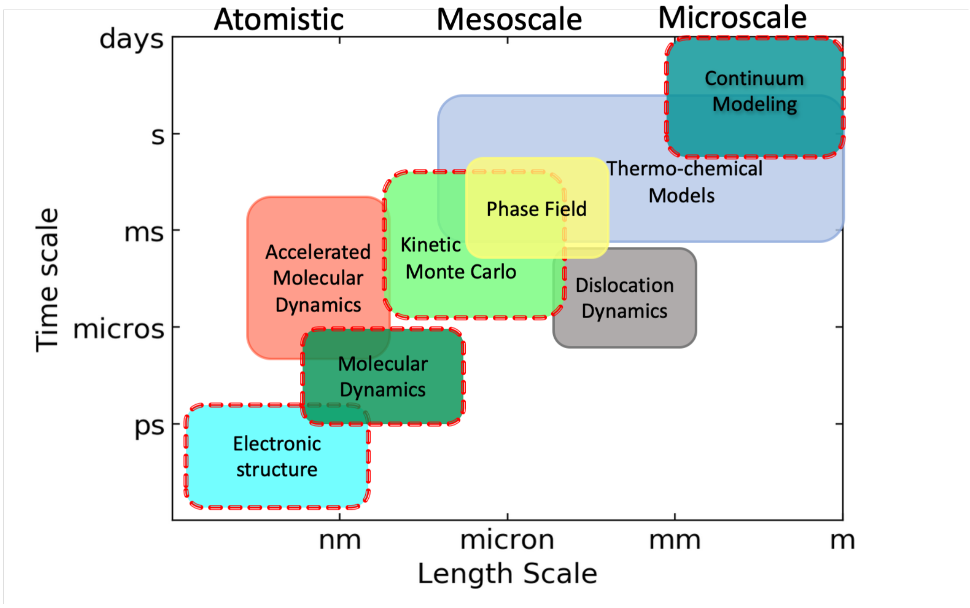

Figure 1.6. Multi-scale modeling and simulation schemes at different times and length scales. Methods used in this thesis are highlighted in red. This graph is adapted from Stan

more than the interatomic lengths (Å). Theories based on continuity can be quantified using numerical methods, such as finite element method (FEM). In FEM, a geometry of interest (2D or 3D) can be divided into small and finite sized elements. Each element represents the physics of the system by a mathematical model defined by partial differential equations (PDEs). All PDEs then can be solved simultaneously with well-defined boundary conditions to calculate physical parameters of the system.[48]

Substrate channeling has been studied via continuum modeling by using law of mass conservation, experimentally obtained transport (*e.g.,* diffusivity) and kinetic parameters (*e.g.,* reaction rate constants) and spatial constraints (*e.g.,* boundary conditions).[49] Earl et. al studied electrostatic channeling by considering a two-site, continuum model with a solid, charged bridge between two sites, wherein the effect of channeling was measured by the product yield.[20] Electrostatic channeling was shown to achieve yields of more than 90% for realistic kinetic rates, matching observations of some naturally occurring processes. Eun et.al. modeled two-step, sequential reaction with and without electrostatic charges on enzyme and intermediates. His continuum study found that long range enzyme interactions affects overall channeling in all cases.[22] A kinetic reaction pathway analysis via continuum modeling suggested that for non-linear reactions, direct proximity channeling is more suitable than the molecular tunneling.[50]

Continuum modeling of substrate channeling mechanisms proved that these mechanisms are the key phenomena for an efficient reaction cascade. However, due to smaller length scale of these mechanisms, it is very important to consider molecular interactions and learn the effect of mesoscopic phenomena on microscopic system.

1.3.2 Molecular Simulations

Motion of molecules and atoms is governed by well-known Langevin equation given as follow :[51,52]

$$\frac{d\dot{y}}{dt} + \beta\dot{y} = F(t)$$

Where, *y(t)* is a particle position, β the friction coefficient and *F(t)* a random fluctuating forces of the system. Langevin equation is consist of three parts, 1) forces arising due to particle interaction, 2) forces arising from the moment of inertia and 3) random forces. In molecular dynamics (MD) simulation, all above three parts contributes to defining motion of particle and maintains temperature and pressure of the system. Brownian dynamics (BD) is a special case of Langevin equation in which forces arising from the moment of inertia of the previous step do not contribute to the motion of particle.[52] Brownian dynamics is computationally efficient modeling techniques over molecular dynamics, since it uses statistically equivalent random forces for the molecular interactions that are insignificant for the problem. In MD, all the forces present in the system need to be calculated and used as an input for the subsequent calculation, regardless of its significance.

Substrate channeling mechanisms has been quantified by Brownian dynamics and molecular dynamics techniques. Brownian dynamics study by Bauler et. al. revealed that effect of proximity channeling collectively depends upon the orientation of sites, the distance between sites and the diameter of sites.[53] Fu et. al. artificially synthesized and modeled two-step, glucose oxidase and horseradish peroxidase (GOx/HRP) enzyme cascade using Brownian Diffusion Model and reported highest channeling efficiency when active sites are 10 nm apart.[38] However, work of Zhang et.al. for same GOx- HRP model system at steady state reveals a strong effect of pH and activity of the slower enzyme on the overall throughput of the cascade and claimed the presence of no effect of proximity in the activity enhancement of reaction cascade.[40] Recent quantification study of the same work by Kuzmak et.al. proved possible significant activity enhancement under diffusion-limited condition.[54] Observed inefficiency and ambiguous results of proximity channeling in the literature are under investigation. The observed inefficiency and ambiguity of proximity channeling led us to consider alternative approaches for the efficient substrate channeling.

Molecular dynamics simulations of electrostatic channeling show good agreement with the experimental results of classic DHFR-TS enzyme cascade.[27] The enzyme system is designed by introducing electrostatic interaction between substrate and enzyme to control the molar flux.[55] Along with our collaborators, we have recently reported models of electrostatic channeling using molecular dynamics and continuum approaches.[20,56] Earl et. al considered a two-site, continuum model with a solid, charged bridge between two sites, wherein the effect of electrostatic channeling was measured by the product yield.[20] Such continuum models do not consider detailed molecular interactions, a limitation that can be overcome through molecular dynamics simulations. Liu et. al. simulated a positively charged peptide chain with different negatively charged intermediates, concluding that these electrostatic interactions can constrain the intermediate without impeding transport between sites. [56]

1.4 Kinetic Modeling of multi-step CO_2 Reduction Reaction

Increased CO_2 concentration in the atmosphere is considered a main cause of global warming.[57] Converting emitted CO_2 into useful chemicals is one of the strategies to reduce CO_2 emission.[58] (Figure 1.7) Along with our collaborators, we propose a reaction cascade of CO_2 reduction to ethane on the surface consist of two different catalytic active sites.

CO_2 can be reduced to small chain carbon molecules (C_1-C_3) such as carbon monoxide (CO), formic acid/formate (HCOOH), methane (CH_4), ethylene (C_2H_4), and

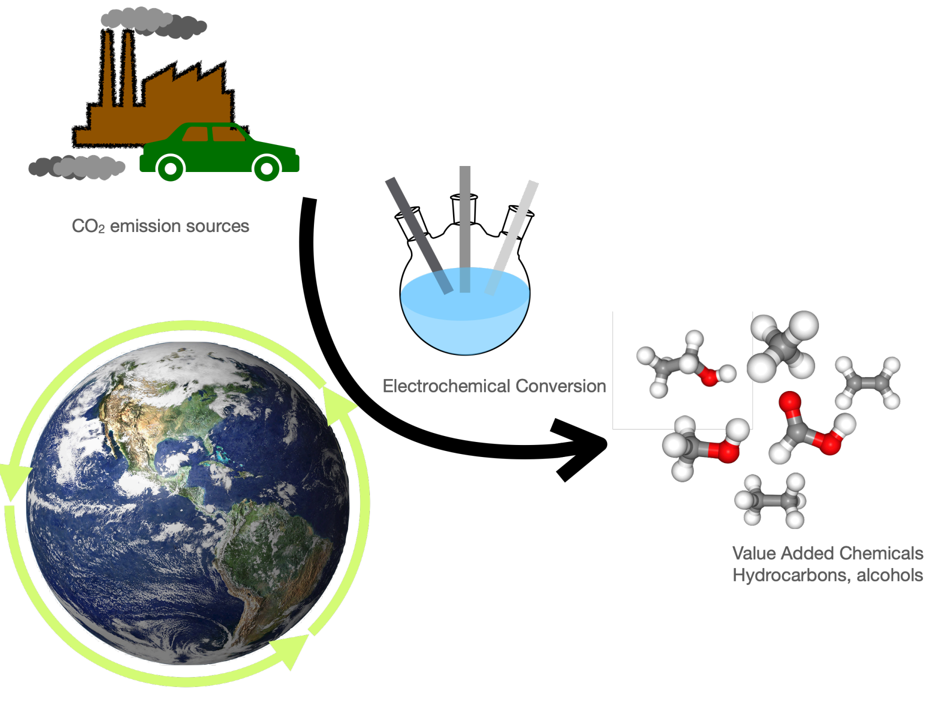

Figure 1.7 A schematic representation of electrochemical conversion of CO_2 into value-added chemicals.[175]

alcohols (CxH2x+1OH) by the metal catalyst or electrochemical reduction on metal electrodes.[59–62] A significant effort has been put into the discovery of an efficient catalyst for the carbon dioxide reduction reaction (CO_2RR) that inhibits the competing hydrogen evolution reaction (HER) and provides high selectivity and faradaic efficiency towards desired products (formate and CO or alcohols and hydrocarbons).[63] Copper based materials has shown high faradic efficiency towards CO_2 electrochemical reduction (CO_2RR) to hydrocarbons (a mixture of C_1, C_2, C_3) with considerable amount but they required high over-potential.[64] The reduction of CO_2 to formate was evident on Pb and Sn catalysts.[65] In-situ infrared spectroscopic studies observed absorbed CO consistently suggesting that adsorbed CO formation is a key intermediate reaction step in CO_2RR. [66–68] Gold[69,70] and silver[71–73] based catalysts reduce CO_2 to CO at high faradaic efficiency and selectivity.

Recently, single-atom metal-centered carbon-based catalysts (M-N-C) has been explored because of atomically dispersed nature of active sites that increases selectivity towards CO formation.[74–86]Further, in the presence of strong interaction between CO and metal, nitrogen coordinated metal centers can reduce CO to hydrocarbons.[75] MNC catalyst has been synthesized using various carbon precursors such as Ketjenblack[87], Ricobendazole, niclosamide[88] , for Oxygen reduction reaction (ORR) as well as polyaniline based MNC for CO_2 reduction reaction.[89] All of these materials show carbon and nitrogen coordinated metal centers on the graphene sheets. Faradaic efficiency of CO formation vs HER is varied from 10 – 90 % depending on different synthesis techniques. But such high selectivity and low range of products makes MNC catalysts an interesting option to optimize further to design integrated catalytic platform.

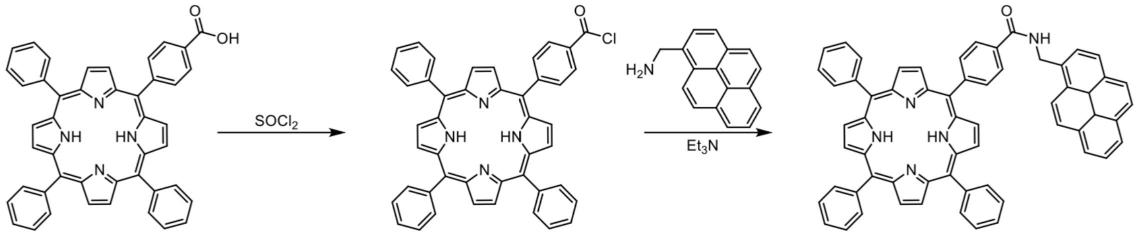

Figure 1.8 Reaction scheme to modify Carboxyphenyl-triphenylporphyrin to form pyrene tether[93]

A molecular catalyst such as iridium and rhodium complex with porphyrin bridges has been explored by S. C. Rasmussen et. al, for electrochemical reduction of CO_2 to hydrocarbons.[90,91] Iridium and Rhodium tetra-phenylporphyrin (Ir-TPP and Rh-TPP) complexes have higher selectivity for hydrogenation of hydrocarbons than the reduction of CO_2.[91] Hence, this homogeneous catalyst can be considered for conversion of ethylene to ethane. Metal-phenylporphyrines complexes can be modified with pyrene tether which then can be anchored to carbon surface.[92] The pyrene tether enables control of the distance between active sites. Therefore, the effect of distance between two active sites on substrate channeling can be studied.

Figure 1.8 shows a reaction scheme to modify carboxyphenyl-triphenylporphyrin to form a single pyrene tether.[93] Carboxyphenyl-triphenylporphyrin will be activated by thionyl chloride and subsequently reacted with aminomethylpyrene to afford the desired pyrene-modified porphyrin. The product can be subsequently reacted with either a rhodium or iridium salt to produce the corresponding immobilizable metal porphyrin. Thus, a strategized synthesis of two active sites, Nitrogen and Carbon coordinated metal center and Iridium and Rhodium triphenylporphyrin complexes, on a graphene sheet shows significant potential to design CO_2RR reaction cascade.

Here we propose, reaction cascade of CO_2 reduction to ethane as follow:

$$2H^+_{(aq.)} + 2e^- \leftrightarrow H_{2_g}\, , E^0 = 0 \tag{13}$$

$$CO_{2_{(g)}} + 2H^+_{(aq.)} + 2e- \leftrightarrow CO_{ads}\ + H_2O_{(l)}, E^0 = -0.104\ V \tag{14}$$

$$2CO_{ads} + 8H^+_{(aq.)} + 8\ \leftrightarrow C_2H_{4_{(g)}} + 2H_2O_{(l)}, E^0\ = -0.34\ V \tag{15}$$

$$C_2H_{4_{(g)}} + 2H^+_{(aq.)} + 2e^-\ \leftrightarrow C_2H_{6_{(g)}}, E^0\ =\ -0.52V \tag{16}$$

Where E^0 is a standard electrode potential vs standard hydrogen electrode (SHE), calculated at 25° C, pH=7 Figure 1.9 describes proposed reaction cascade. From the above three-step reaction cascades, reaction 15 and 16 occurs at two different active sites. CO_2 first adsorbs on the metal center of MNC catalyst and reduce to CO_{ads}. In the presence of strong CO-metal interaction, CO_{ads} can reduce to ethane (C_2H_4). Here, C_2H_4 can be transported from one active site to another through surface diffusion. Once C_2H_4 reaches the iridium or rhodium triphenylporphyrin (TPP) tethered active site, it further reduces to ethane (C_2H_6).

Our collaborators at the University of California at Irvine successfully synthesized a single metal atom catalyst with nitrogen and carbon precursor by using the sacrificial

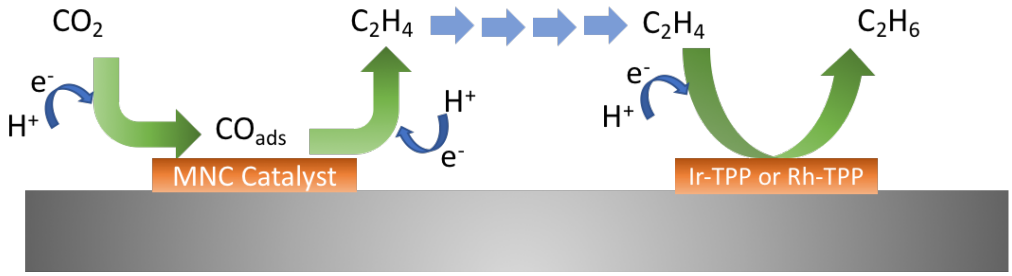

Figure 1.9 Reaction cascade for CO_2 electrochemical reduction to ethane (CO_2RR). TPP=triphenylporphyrin

support method. This novel synthesis yields a highly porous and dispersed catalyst and thus providing access to a single metal active site for CO_2RR.[74] Due to the complex nature of the CO_2 reduction reaction mechanism, mechanistic understanding of a catalytic system has becomes needed to further optimize catalytic performance and design better catalysts.[94] Multi-scale simulation frameworks that capture atomistic insights via DFT study coupled with microkinetic modeling will provide a better understanding of the effect of the reaction kinetics on overall reaction rate.

1.5 Simulation Approaches II

Integrated catalytic designs are heterogeneous systems that involves many events such as diffusion, adsorption/desorption, reaction on the catalytic surface.[95] One of the key assumptions for continuum modeling of a heterogeneous system is such that active sites are equally distributed over a surface. In real life that is not true. At the atomic scale, adsorbates randomly occupy active sites on the surface. Therefore, one needs to model such a system carefully at macroscopic as well as microscopic scale.

1.5.1 Microkinetic Modeling

Due to spectroscopic limitations, quantifying and observing catalytic reactions at atomic level is still impossible. Heterogeneous catalytic reactions are even more complex to study because of the multiphase nature of chemical transformation other than atomic interactions. Therefore, developing simulation methods at different length and time scales to describe microscopic chemical transformation is critical to the design of new catalysts and control of the overall chemical process.[96]

Heterogeneous catalytic chemistry is a multiscale phenomenon in nature. In such systems, a reaction takes place on an active site at the sub-nanometer length scale.

However, the macroscopic results of the chemical transformation are affected by adsorption/desorption of chemical species on the surface, transport of the species from the bulk to the surface that ranges from nanometer- millimeter length scale and picoseconds to milli-seconds timescale. Non-uniform active site distributions and the effect of surface coverage on the kinetic rate are some of the intrinsic heterogeneity of the catalytic systems that also need to be considered while modeling the system. Due to such complexity, coupling two or more modeling techniques is the necessary to capture the overall chemical transformation.

Microkinetic modeling (MKM) techniques use a detailed surface reaction mechanism via a set of elementary reactions to model the kinetic system.[97] The MKM method identifies a dominant reaction pathway and rate determining step (RDS) by simulating elementary reactions. This is a more reliable approach over conventional kinetic modeling approaches such as Langmuir–Hinshelwood–Hougen–Watson (LHHW) models where RDS has to be assumed.[96] Experimental techniques cannot measure kinetics of the elementary reaction by calculating activation energy and entropy changes. This may alternatively be achieved by using first principle-based calculations such as the density functional Theory.

The rate of any n^{th} elementary surface reaction, r_n can be written as the function of fractional surface coverage of species being transformed in n^{th} reaction, θ_n and the rate constant, k_n.

$$r_n = -k_n \theta_n \qquad [17]$$

According to the steady state approximation a set of linear algebraic equations can then be generated using following equation and solved simultaneously.

$$\frac{d\theta_i}{dt} = \sum \sigma_i r_i = 0 \qquad [18]$$

Where σ_i is a stoichiometric coefficient of the species i, θ_i is a fractional surface coverage of species i and r_i is the reaction rate of species i and t is the time.

Activation energy required for each elementary reaction can be calculated from the transition state theory (TST).[98] TST connects Gibb's free energy of the product, reactant and the transition state via the Arrhenius equation as follow:

$$k = \frac{k_B T}{h} \exp\left(\frac{-\Delta \mathrm{G_{TS}}}{k_B T}\right) \qquad [19]$$

$$K = \exp\left(\frac{-\Delta \mathrm{G_{rxn}}}{k_B T}\right) \qquad [20]$$

Where, k is the forward kinetic rate constant and K is the equilibrium rate constant of an elementary reaction. $-\Delta \mathrm{G_{TS}}$ and $-\Delta \mathrm{G_{rxn}}$ are the Gibbs free energy of the transition from reactant to product and Gibbs free energy of the reaction, respectively. A pre-exponential factor for the rate constant is approximated and consist of Boltzman constant, k_B, absolute temperature, T and Planck's constant, h.[94] These Gibbs free energies can be calculated using atomistic solutions.

1.5.2 Density Functional Theory

In a heterogeneous catalytic system, interactions between adsorbate-catalyst and adsorbate-adsorbate determine the potential energy of the surface and thus, the Gibbs free energy barrier for the chemical transformation. During the reaction, reactants are required to overcome the transition state barrier energy to form the product.[99] These atomic scaled energy parameters can be calculated using a quantum mechanical method, such as density functional theory. [96,100,101]

Atomistic simulations deal with quantification of the electronic structure of molecules and atoms. This modeling approach is based on solving the time independent Schrödinger equation by reasonable approximations.[102]

$$\widehat{H}\psi = E\psi \quad [21]$$

Where, $\widehat{H}$ is the Hamiltonian operator, ψ is the state vector of the system, and E is a constant equal to the energy level of the system. The Schrödinger wave function contains all the information about the quantum system and therefore is extremely precise, theory to quantify the electronic parameters. However, it is extremely difficult to solve the Schrödinger equation for systems of more than one electron as computational cost exponentially increases with the number of electrons in the system.

Therefore, many methods have been developed based on different treatments on electron-electron interactions and exchange correlation approximations such as Hartree Fock (HF), Møller–Plesset Perturbation theory (MPn), configuration interactions (CI), coupled clusters (CC), Density functional theory (DFT).[100] DFT is based on the two fundamental theorems.[103] The first theorem by Hohenberg and Kohn states that ground state energy from the Schrödinger equation is a unique function of electron density. In other words, one can map the ground state energy to the ground state electron density. The second theorem defines a property of the functional, that the electron density that minimizes the energy of the overall functional is the true electron density, corresponding to the solution of Schrödinger equation. By combining both above theorems, the energy function can be written as follows[101]:

$$E[\{\psi_i\}] = E_{known}\,[\{\psi_i\}] + E_{xc}[\{\psi_i\}] \quad [22]$$

Where, $E[\{\psi_i\}]$ is the ground state energy, $E_{known}\ [\{\psi_i\}]$ is a "known" energy consisting of the electron kinetic energy, the coulomb interactions between the electrons and nuclei, the coulomb interactions between pairs of electrons and the coulomb interactions between pairs of nuclei, and $E_{xc}[\{\psi_i\}]$ is the exchange-correlation functional which includes all quantum mechanical terms that were not considered in $E_{known}\ [\{\psi_i\}]$ term.

Now, in order to solve the multi-body Schrödinger equation, one needs to solve a set of single-electron wave functions defined by the Kohn–Sham equation as follow:[104]

$$\left[-\frac{\hbar^2}{2m}\nabla^2 + \mathrm{V(r)} + V_H(r) + V_{xc}(r)\right]\psi_i(r) = \varepsilon_i\psi_i(r) \qquad [23]$$

Where, V(r) is the potential defined in 'known' energy term, $V_H(r)$ is the Hartree potential, and $V_{xc}(r)$ is the interaction between and electron and the collection of atom nuclei the functional derivative of the exchange-correlation energy.

The exact functional form of the exchange correlation is unknown. However, two main types of approximations have been developed, namely local density approximation (LDA) and the generalized gradient approximations (GGA).[101] LDA considers an electron in the uniform electron gas, which is a reasonable approximation for fluids. In GGA, an electron density gradient is considered to calculate exchange correlation functionals, which is a more corrective form of LDA. Based on how the electron density gradient is incorporated in GGA functional, there are many distinct GGA functions available in the literature such as PBE, rPBE, PW.[101,105]

Computationally, microkinetic modeling has been used to study reaction mechanisms, and the most favorable pathway for CO_2RR on various catalysts. Liu et. al. developed a microkinetic model and validated the pH effect of CO_2RR on a Cu surface via

Tafel analysis.[106] However, Shinagawa et. al. demonstrated the importance of surface coverage in microkinetic modeling over Tafel analysis.[107] The work of Bart *et. al.* provided potential dependent product distributions on Cu surfaces and found that the formation of COOH* is a critical step for selectivity towards CO or CH_4 formation and CO_2 diffusion limitations at high overpotentials.[108] Singh et. al. provided a multiscale simulation framework consisting of DFT, microkinetic modeling, and continuum modeling that showed good agreement with the experimental data for partial current densities of CO_2RR over Ag surface.[94] In DFT assisted MKM method, free energy prediction is corrected by considering electrolyte polarization to increase the accuracy of model.[109] The effect of the localized electric field generated by the electrolytes on the surface coverage of the CO2RR catalytic system on Ag is studied by Chen et.al. via microkinetic modeling approach.[110] To our knowledge, multi-scale modeling of single-metal atom catalyst has not yet been reported in the literature.

1.6 Overview of work

This work aims to study the effect of kinetics and transport on the channeling efficiency of the multi-step reaction cascades. Confining the intermediate pathway is a one way to assure efficient transport between two active sites. We study confinement at macroscopic and microscopic scales by using continuum modeling and molecular dynamics approach, respectively. We also study the reaction mechanism of the multi-step CO_2 electroreduction reaction on a single metal atom catalyst via a multi-scale modeling approach. This dissertation involves the following projects:

In Chapter 2, the effect of confinement on the channeling efficiency was studied via a continuum modeling approach. The effects of kinetics and transport, as well as geometrical

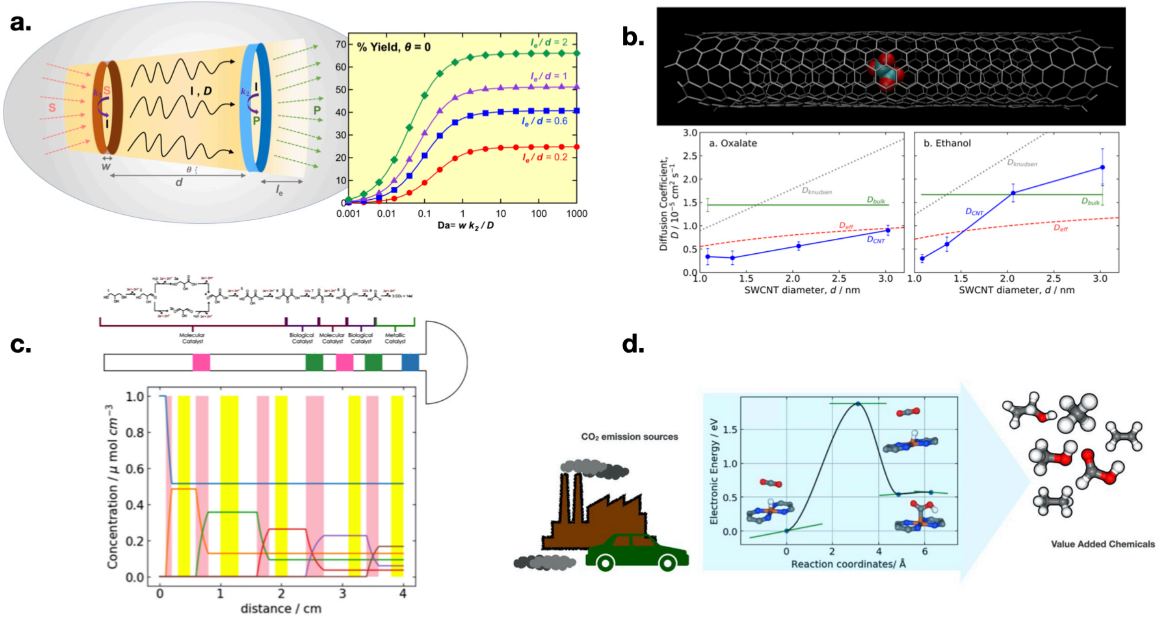

Figure 1.10 Overview of the work. a) Continuum modeling study of nanoscale confinement, b) confinement and diffusion of small molecules in the molecular tunnel, c) continuum modeling of the glycerol oxidation cascade on a paper-based microreactor (adapted from ref 203), d) microkinetic modeling of carbon dioxide reduction reaction cascade.

parameters of confined geometry, were studied through product yield. Larger confined distance between active sites retained intermediate for maximum product yield. (Figure 1.10a)

In Chapter 3, intermediate transport in confined space is described using molecular dynamics. In this work, the diffusivity of two intermediates was studied in a carbon nanotube, used as a model for tunnel structure. The intermediate retention time was also studied by modifying carbon nanotube ends. The maximum intermediate retention was achieved by decreasing effective diffusivity due to Knudsen diffusion and charged termini. (Figure 1.10b)

In Chapter 4, a microkinetic modeling of CO_2 electroreduction reaction is developed to study the reaction mechanism. This work involves DFT based parameter estimation and electrochemical response validation via kinetic modeling. Surface coverages of chemical species varied with potential and played very important role in competitive CO_2RR and HER cascades. (Figure 1.10d)

In Chapter 5, a microkinetic model of glycerol oxidation on a paper-based microreactor was studied via continuum modeling. Convective forces in such a microfluidic reactor are important to prevent back diffusion of chemical species and increase the selectivity of the desired products. (Figure 1.10c)

Chapter 2

Simulation of Intermediate Channeling by Nanoscale Confinement[*]

2.1 Introduction

Molecular tunneling sterically confines an intermediate within a tunnel and prevents access to the bulk. Thus, tunneling has the potential of 100% channeling efficiency in the case of a non-leaky tunnel. The geometry of such tunnels significantly affects channeling efficiency, thus motivating this study.

Molecular tunneling mechanisms have been well studied experimentally. For example, the two-step biosynthesis of l-tryptophan from indole-3-glycerol phosphate (IGP) is catalyzed by tryptophan synthase (TS), a bifunctional enzyme.[10] The α subunit of TS cleaves IGP to form indole and glyceraldehyde 3-phosphate. Allosteric signals control the channeling of indole between α and β subunits via a 25 Å molecular tunnel,[111] and indole is condensed at the β subunit with serine to produce l-tryptophan. Kinetic analysis of this reaction concludes that α-β indole transfers are fast ($\geq 1000\ \mathrm{s}^{-1}$) with comparable conversion rates at the β site.[24,112] The TS complex takes on a non-leaky tunnel conformation when IGP binds at the α subunit and serine binds at β. This state is often described as “closed conformation”. If either or both the substrates are not present at the sites, the TS complex does not form a tunnel. Such conformational changes were studied by Dunn et. al. by open and closed tunneling experiments, which proved that total indole sequestration occurs in a closed conformation.[113]

---

[*] This work is published as Chavan, K. S., Calabrese Barton, S. Simulation of Intermediate Channeling by Nanoscale Confinement. *J. Phys. Chem. C* **2018**, *122* (26), 14474–14480, doi:10.1021/acs.jpcc.8b01922.

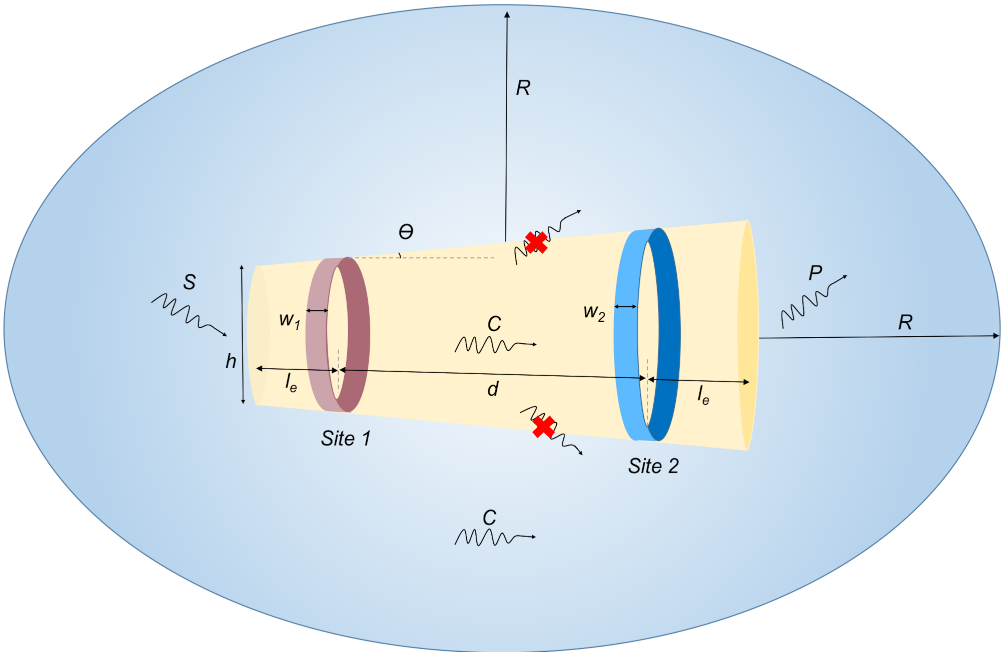

Figure 2.1 Confinement model. Substrate, S, reacts at Site 1 to form intermediate, C, which diffuses to Site 2 and is converted to product, P. Parameters l_e, d, h and w are the end length distance, distance between Site, tunnel diameter and width of Site, respectively.

In this work, the effect of a physical tunnel was studied by confining the intermediate path between two sites. An axisymmetric 2D model is applied to a confined assembly to study the effect of transport as well as kinetics on product yield. We considered competition from bulk diffusion by allowing diffusion to the domain edge. The geometry includes a conical angle in the tunnel that can promote radial diffusion towards a product-forming site. The significance of reaction kinetics as compared to transport is considered via the Damköhler number, Da.

2.2 Methods

To approximate molecular tunneling, a confined geometry is considered as shown in Figure 2.1. In this 2-dimensional axisymmetric geometry, the intermediate, C, produced at Site 1 either diffuse into the confined tunnel and reacts at Site 2 to form the product, or can diffuse out of the tunnel into the bulk through tunnel ends. Unlike the mechanism for Tryptophan synthase, no closed tunnel conformation was considered in this study.[14] To maintain cylindrical symmetry, we assume that the sites are ring-shaped inside the tunnel with a diameter identical to the tunnel wall and uniformly distributed over the surface. The surface area of both sites was fixed for all studies; when conical angle, θ, was varied, the active site widths, w_1 *and* w_2, were adjusted to maintain the fixed area. Further, we assume the system has reached a steady state. Single-step reactions at sites 1 and 2 are considered. Substrate S reacts at Site 1 and produces intermediate, C, which then channels to Site 2 and reacts to produce P:

$$\mathrm{S} \xrightarrow{\text{Site 1}} \mathrm{C} \qquad [1]$$

$$\mathrm{C} \xrightarrow{\text{Site 2}} \mathrm{P} \qquad [2]$$

A zeroth order, the irreversible rate law is assumed for Reaction [1] and first-order, irreversible rate law is assumed for Reaction [2], respectively:

$$J_1 = k_1 \qquad [3]$$

$$J_2 = k_2 C \qquad [4]$$

where C is the intermediate concentration, k_1 is the zeroth-order rate constant for reaction 1, andk_2 is the heterogeneous first-order rate constant for reaction 2. The system can operate in a mass transport limited condition when the consumption rate of intermediate at Site 2 is very high such that intermediate concentration at Site 2 is zero.

In the absence of pressure or potential gradients, and assuming constant diffusivity, a mass balance on the intermediate leads to Laplace's equation as the governing equation for intermediate transport:

$$\nabla^2 C = 0 \qquad [5]$$

Boundary conditions were set to impose the tunneling mechanism. The tunnel walls are impervious to the normal flux of intermediate, except at sites 1 and 2, where the flux is related to the reaction rates given by Eqs. 3 and 4, respectively. To arrive at a steady-state model, and to avoid bulk intermediate contribution to reaction [2], intermediate concentration was set to zero at the domain boundary. By setting such a boundary condition, intermediate is allowed to transport internally through the tunnel as well as externally within the domain. Once an intermediate escape into the domain, it can either escape out of the system at the boundary or be transported to the second site and react to form the product.

The Laplace equation (Eq. 5) subject to the above boundary conditions was solved numerically, in 2D axisymmetric coordinates, using COMSOL finite element modeling software and the Transport of Dilute Species (TDS) application module. An elliptical domain was chosen to achieve uniform separation between the sites and the system

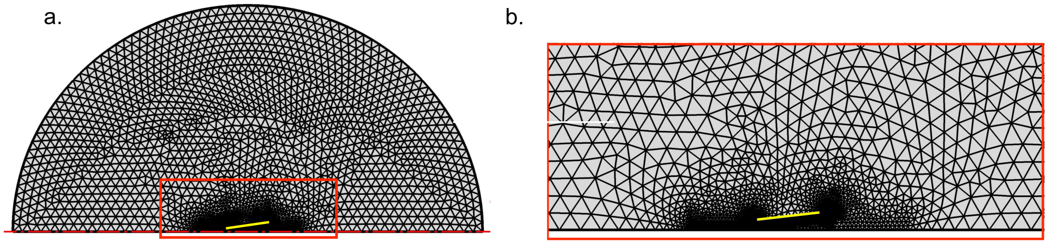

Figure 2.2 Meshing scheme for 2D axisymmetric geometry. a) Overall view. b) enhanced view of mesh in vicinity of the tunnel, shown by rectangle in (a). Yellow line indicates tunnel wall.

boundary. The system was meshed using a physics-controlled triangular mesh with extremely fine element size, and a typical mesh is shown in Figure 2.2.

The minimum element size of the meshing is 0.0089 nm. Baseline model parameters are presented in Table 2.1.

Table 2.1 Baseline Parameters

Parameter	**value**
Zeroth-order rate constant at Site 1, $\boldsymbol{k_1}$ / molecules nm^2 s^{-1}	10^9
First-order rate constant at Site 2, $\boldsymbol{k_2}$ / nm s^{-1}	10^7
End length, $\boldsymbol{l_e}$ / nm	1
Tunnel diameter, $\boldsymbol{h}$ / nm	1
Distance between sites, $\boldsymbol{d}$ / nm	5
Conical angle, $\boldsymbol{\theta}$ / degree	0
Width of Site 1, $\boldsymbol{w_1}$ / nm	1
Width of Site 2, $\boldsymbol{w_2}$ / nm	1
Tunnel wall thickness, $\boldsymbol{t_h}$ / nm	0.1
Distance between tunnel and domain edge, $\boldsymbol{R}$ /nm	50
Diffusion coefficient, $\boldsymbol{D}$/ nm^2 s^{-1}	10^9

2.2.1 Yield

The figure of merit for performance of this system is product yield, which also represents channeling efficiency for the system. Yield can be defined as the rate of consumption of intermediate relative to the rate of its formation, expressed mathematically using surface integrals of the reaction rate at each site:

$$Yield = \frac{\int_{Site\ 2} k_2 C\ dS}{\int_{Site\ 1} k_1 dS} \qquad [6]$$

2.3 Results and Discussion

Initially, Equation 5 is solved numerically assuming infinitely fast kinetics at both sites such that mass transport is rate controlling. We then introduce finite kinetics expressed in terms of Damköhler number, Da, the ratio of a reaction time constant to a diffusion time constant.

$$\mathrm{Da} = \frac{w k_2}{D} \qquad [7]$$

Here, w is the width of both sites at $\theta = 0°$ ($w = w_1 = w_2$).We vary Da from 0.001 to 1000 by varying diffusion coefficient, D from 10^4 to 10^{10} $nm^2\ s^{-1}$. Reaction rates, k_1 and k_2, and geometrical parameters such as end length, l_e, the distance between sites, d, conical angle, θ, and tunnel diameter, h, were also varied to study channeling efficiency.

Mass-transfer limited concentration profiles of non-confined and confined assemblies are shown in Figure 2.3a-b. Significant intermediate concentration is observed throughout the confined region, in contrast to non-confined geometry wherein intermediate concentration approaches zero at the halfway point between sites. This comparison illustrates the intermediate activity retention achieved by the confined geometry.

Within the cylindrical confined geometry (with θ=0°), axial intermediate diffusion dominates over radial diffusion.[114] Directional diffusion from Site 1 to Site 2 is enhanced by a positive conical angle, θ. Figure 2.3c shows the effect of the conical angle on the yield under mass transfer control. The initial increase in the conical angle up to θ =17.4º promotes diffusion toward Site 2 over the diffusional loss at the small end of the cone, leading to a three-fold increase in yield. At large distances between sites, conical geometry provides consistently higher yield compared to cylindrical geometry. Further increase in conical angle increases the diffusional loss from the large end of the cone, decreasing yield (Figure 2.3d).

2.3.1 Effect of kinetics

Effects of mass transport and kinetics are studied and quantified by Damköhler Number, Da. Figure 2-4a shows the effect of Da on the yield for both confined and unconfined systems, with the normalized distance between sites, $\frac{d}{w}$, as a parameter. As Da is increased towards the mass transport limited region, yield increases significantly, and

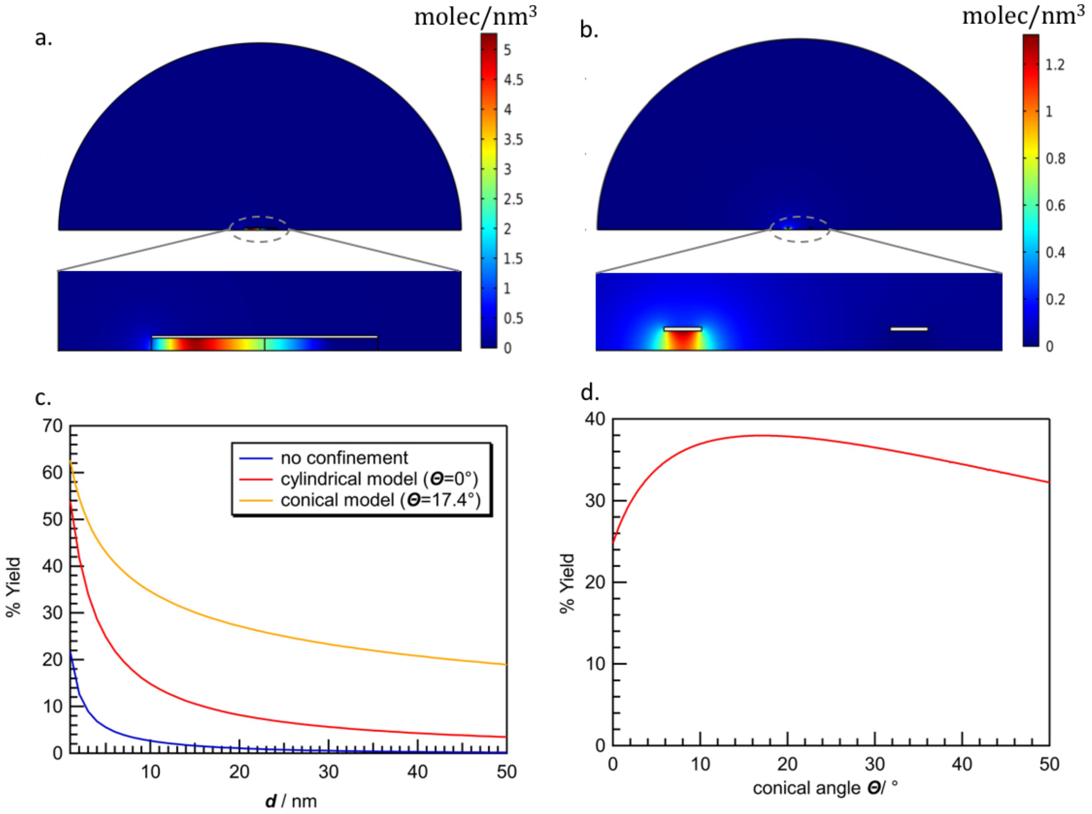

Figure 2.3 Mass transport of intermediate. a) Mass-transfer limited intermediate concentration profile for confined configuration, with θ=0°. b) Mass-transfer limited intermediate concentration profile for non-confined configuration. c) Impact of Site distance on mass-transport limited yield. d) Effect of conical angle, θ, on mass-transport limited yield. Other parameters are given in Table 1.

this transition is observed at Da $\approx$ 1. For the present geometry with $D = 10^9$ nm^2 s^{-1}, Da $=$ 1 corresponds to $k_2 = 10^9$ nm s^{-1}, an exceptionally high value. Assuming realistic kinetic parameters, Da$\ll$ 1 and the system is controlled by reaction kinetics rather than mass transport.[20] Therefore lowering the transition Da by changing geometrical parameters can lead to desirable increases in yield.

The transition value of Da shifts lower as the distance between sites is decreased, due to the short intermediate diffusion length. The effect of site distance, d, is most significant in the mass transport limited region, Da$\gg$ 1 as mass transport depends upon the diffusion length (Figure 2.4b).

2.3.2 Effect of end length

The distance between the sites and the end of the tunnel, l_e, controls axial resistance to diffusion of the intermediate into the bulk. Figure 2-5a shows the effect of normalized end length, $\frac{l_e}{d}$, on yield for varying Da. As an end length, $\frac{l_e}{d}$, increased from 1 to 10, product

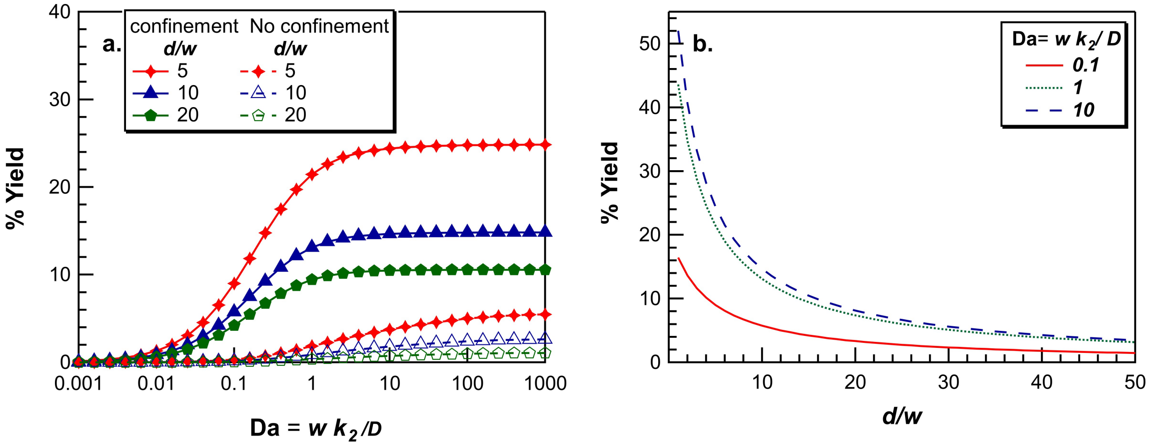

Figure 2.4 Influence of reaction kinetics on confinement efficiency. a) Effect of confinement on the yield for varying distance between Site , d, as a function of Da. b) Effect of distance between Site, d, on the yield for varying Da. Other parameters are given in Table 1.

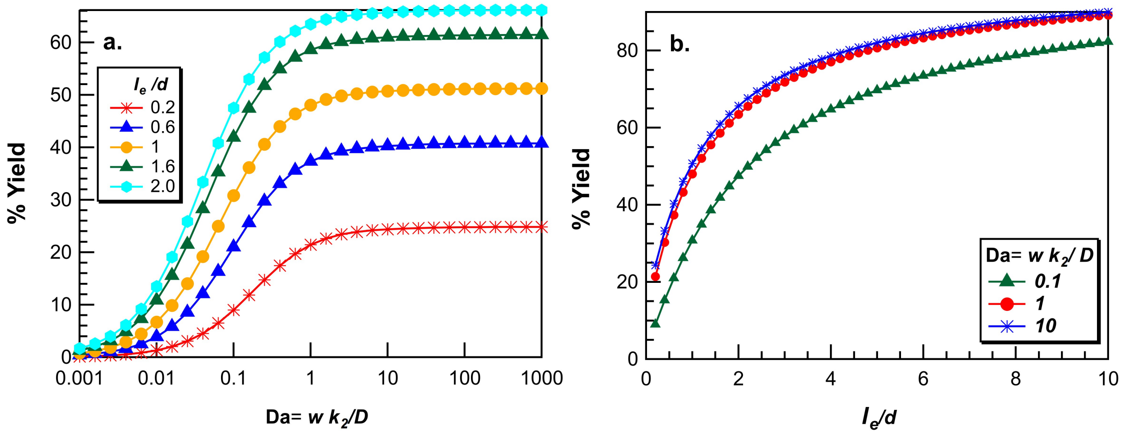

Figure 2.5 Influence of tunnel end length. a) Effect of confinement on the yield for varying end length distance, l_e, as a function of Da. b) Effect of end length distance, l_e, on the yield for varying Da. Other parameters are given in Table 1.

yield increased from 6% to 45% at Da=0.01 from 45% to 90% at Da=100. Such large end length configurations approximate the closed conformation found in tryptophan synthase.[14] Therefore, this configuration may represent the simplest approach to mimicking molecular tunnels found in nature. Along with increased product yield, a significant downward shift in the transition Da value is observed. Transition Da shifts down to 0.1 for $\frac{l_e}{d}$=6. Similarly, Figure 2-5b shows increasing yield for increasing $\frac{l_e}{d}$ over a range of Da.

2.3.3 Effect of tunnel diameter

As tunnel diameter, h, varies, for the fixed surface area of both sites, only transport of the system is affected. Here we introduce a different Damköhler number, $\mathrm{Da}' = \frac{dk_2}{D}$ based on the site-site distance, d. The increasing diameter increases the probability of intermediate loss to the bulk, as observed in Figure 2.6b. As tunnel diameter increases, yield decreases due to an increase in radial diffusion towards the center of the tunnel. This effect is more noticeable at low Da′, e.g. $\mathrm{Da}' \sim 0.5$, where there is a strong inverse proportionality between yield and tunnel diameter. Lower tunnel diameter also reduces the transition Da′ (Figure 2.6a), which is desirable for kinetically limited systems.

2.3.4 Effect of conical angle

Figure 2.7b shows the effect of the conical angle on the yield at various Da′. In the kinetically limited region, Da′ < 1, diffusion leads to increased loss from the large end of the cone, and therefore lower yield, as θ increases. The cylindrical geometry is therefore optimal in the kinetically limited regime. On the other hand, in the mass transport limited region, an increase in the diameter of the second site promotes intermediate to diffuse towards the reaction site and results in higher yield. For the conical geometry, an increase in the end length, l_e, changes the diameter of the end of the tunnel. At large Da′, increased end length does diminish intermediate loss from the smaller end, which increases yield for $\frac{l_e}{d}$ up to 2 (Figure 2.7c, 2.7d). However, an increase in $\frac{l_e}{d}$ also increases the tunnel diameter at the larger end, increasing diffusional flux out of the larger end (Figure 2.8). For moderate Damköhler number (Da′ ≤ 50) this diffusional loss decreases yield slightly for $\frac{l_e}{d}$ >

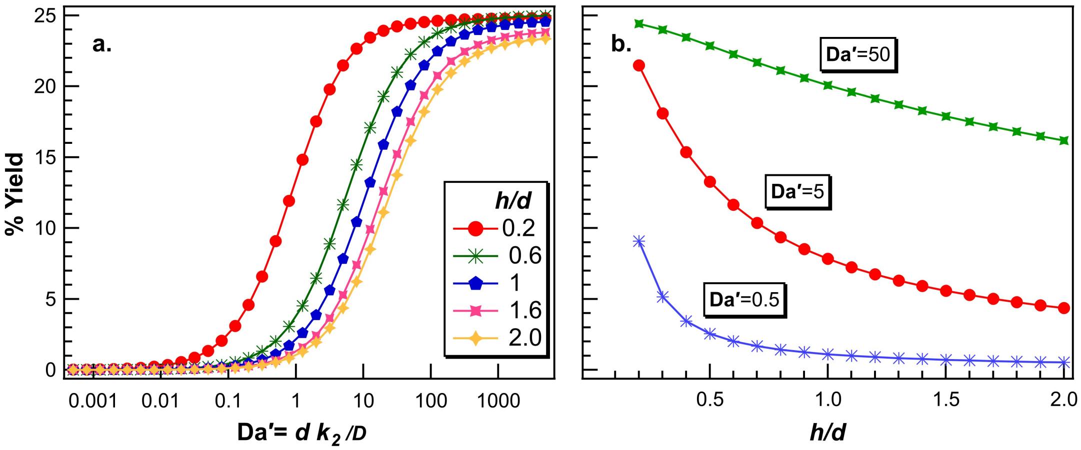

Figure 2.6 Influence of tunnel diameter. a) Effect of confinement on the yield for varying tunnel diameter, h, as a function of Da'. b) Effect of tunnel diameter on the yield for varying Da′. Other parameters are given in Table 2.1

2, but at Da$'$ ~500, the rate at the second site is sufficient to negate this effect. At low Da$'$, end length does not show any effect on the yield, because the reaction is not diffusion controlled. Conical geometry can, therefore, improve yield in the mass transport limited region but is not effective under kinetic control.

2.3.5 Toward experimental validation

Substrate channeling has been studied experimentally by stopped-flow experiments to observe steady-state flux.[115,116] The most common method used to experimentally validate computational studies is to measure lag time, τ.[20,27,50,56] In the presence of substrate channeling, the lag time is expected to reduce compared to free enzymes.[20,27,56,116,117] This reduced lag time can be correlated to the yield as:[20,27]

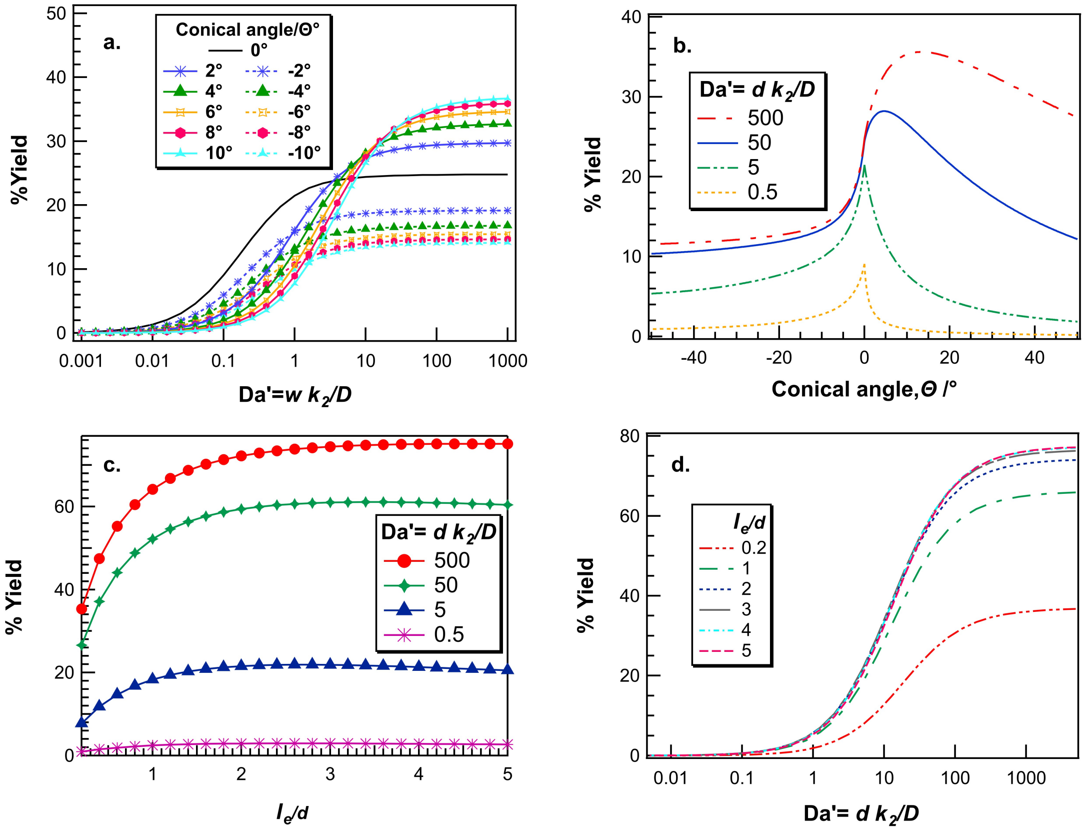

Figure 2.7 Influence of tunnel conical angle. a) Effect of Da' on the yield for varying conical angle. b) Effect of conical angle, θ, on the yield for varying Da'. c) Effect of end length, l_e for θ =10° and varying Da'. d) Effect of Da' for varying end length, l_e.

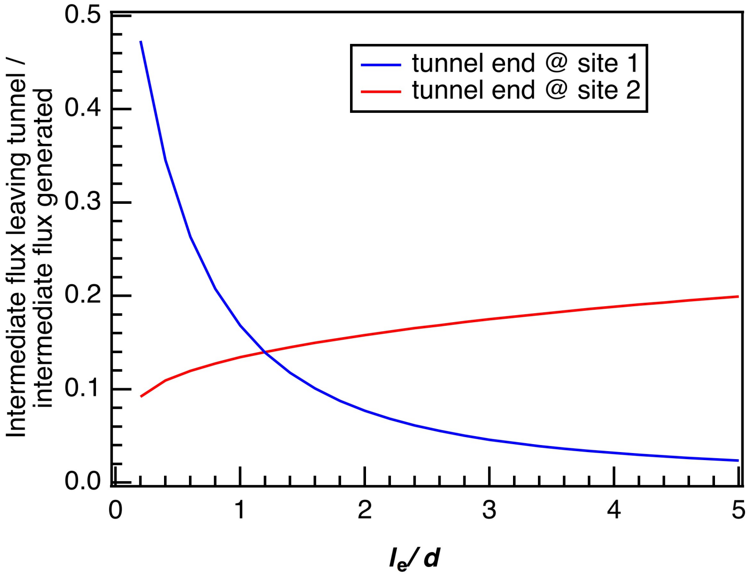

Figure 2.8 Flux at both ends of the tunnel for $\boldsymbol{\theta}$=10° and Da' =500.

$$\frac{\tau}{\tau_o} = 1 - yield \qquad [8]$$

Where, τ_0 is the lag time in the absence of the channeling. Assuming that k_1' and k_2' are homogeneous rate constants for sites 1 and 2, respectively, for $k_2' \gg k_1'$, $\tau_o = {k_2'}^{-1}$ is the lag time in the absence of substrate channeling. Further, the present tunnel structures can be fabricated by functionalizing silica nanotubes[118,119] or TiO_2/Pt conical cylinders[120], and lag time can be studied for an ensemble of tubes, and correlated with computational results. A transient version of the present model would facilitate the calculation of τ for direct comparison with the experiment, which will likely reveal a significant dependence on specific molecular interactions that are not captured in the present model. The effect of these interactions may be further studied using molecular dynamics approaches.[56]

2.4 Conclusions

We studied the effects of kinetics and transport on the tunneling mechanism of substrate channeling. Confinement of sites and the intermediate pathway shows a significant enhancement in the product yield. Lower transition Damköhler number, Da, can be achieved by decreased separation of sites and increased distance to the tunnel end. For large values of Da, such that the reaction is mass-transport limited, a conical tunnel with angle 17.4°shows significantly higher yield than a cylindrical tunnel, but this observation does not extend to kinetically limited reactions.

Continuum modeling of this confined geometry lays a framework to incorporate tunneling mechanisms in integrated catalytic systems. However, since continuum modeling does not consider molecular interaction at the nanoscale, physical properties need to be validated from simulations and experiments using specific molecular systems.

2.5 Supporting files

COMSOL files (*.mph) of all the above calculations are publicly available.

Conical Configurations: git@gitlab.msu.edu:chavanka/cone_model.git

Cylindrical Configurations:git@gitlab.msu.edu:chavanka/2D-nondimentionalise-confinement.git

Chapter 3

Confinement and diffusion of small molecules in a molecular-scale tunnel[†]

3.1 Introduction

An efficiency of multi-step reaction cascades can be increased by controlling the transport of intermediates between active sites. Molecular tunneling, a substrate channeling mechanism provides such a transport control by physically confining the pathway of intermediates.[8]

As a naturally-occurring example of molecular tunneling is the nano-scaled molecular tunnel present in tryptophan synthase (TS), a bifunctional enzyme, transfers an intermediate, indole, between two active sites with a high diffusion rate ($\geq 1000\ s^{-1}$), comparable to the conversion rates.[24,121] This work represents the first steps toward understanding the molecular-scale transport in such a channeling system.

Our previous model (chapter 2) of nano-scaled confinement used a continuum, finite element method, and demonstrated that confinement enhances the yield of a two-step reaction system compared to a non-confined system.[122] This nano-scale model treated reaction and diffusion inside a single-walled carbon nanotube (SWCNT) and considered a range of geometric, transport and kinetic parameters. However, nano-scale molecular interactions were not considered and can significantly affect the transport properties of the system.

[†] This work is published as Chavan, K. S.; Barton, S. C.; Calabrese Barton, S. Confinement and Diffusion of Small Molecules in a Molecular-Scale Tunnel. *J. Electrochem. Soc.* 2020, *167* (2), 023505, doi:10.1149/1945-7111/ab6dd2.

The solvent structure inside a SWCNT plays a critical role in transport through that region. Carbon nanotubes have been studied extensively for water confinement. Both experimental[123,124] as well as simulation[125–130] studies show that, even though CNT surfaces are hydrophobic in nature, water can easily fill the CNT interior through open ends. However, water molecules confined inside SWCNTs with diameter approaching molecular scales exhibit different behavior than in the bulk.[125] For diameters less than 1 nm, water molecules experience the hydrophobicity of the SWCNT wall, resulting in a single-file hydrogen bonding pattern.[131] As the SWCNT diameter increases, a transition from tubular to bulk pattern is observed, accompanied by an increased water density.[131,132]

In this work, transport of the intermediates inside the nanochannel is studied by using molecular dynamics (MD). We represent the molecular tunnel with a single-walled carbon nanotube (SWCNT) and consider negatively charged, oxalate that is found in abundance in biological reaction cascades.[133–135] In contrast, ethanol is considered as an uncharged intermediate species, because its size is comparable with oxalate. We observe

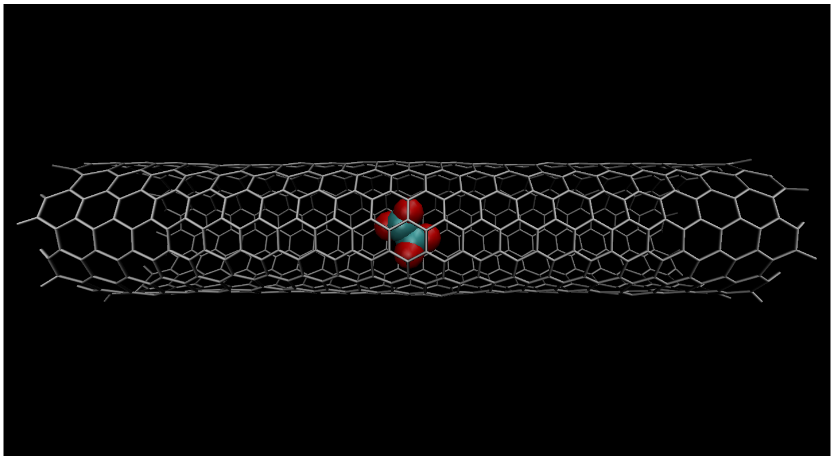

Figure 3.1 Initial configuration of the well equilibrated system. Single-walled carbon nanotube (grey) represents a molecular tunnel and oxalate represents an intermediate molecule. Oxygen and carbon atoms are represented by red and green colors respectively.

the variation in the diffusivity of the intermediate within the nanochannel and study the structure of aqueous solvent surrounding the intermediate in this region. Finally, we modified the nanotube ends using electrostatic charges in order to further retain charged and polar intermediates.

3.2 Methods

A carbon-ended, armchair, single-walled carbon nanotube (SWCNT) was used as a nanoscale confined tunnel (Figure 3.1). Armchair carbon nanotubes have lower local charge magnitudes than zigzag SWCNsT.[125] This provides more control to study intermediate charge effects. Therefore, an armchair SWCNT was used in this study. Transport of a negatively charged small molecule (oxalate, $C_2H_4^-$) and a neutral molecule (ethanol, C_2H_5OH) were studied within this tunnel. Specifically, molecular dynamics (MD) studies were performed to track the motion of intermediate molecule inside the SWCNT for 5-30 ns. We performed these studies for four different SWCNT diameters: 1.08 (8, 8), 1.35 (10, 10), 2.06 (15, 15) and 3.02 nm (22, 22). The effect of the tunnel length to diameter ratio on retention time was studied with SWCNT diameters of 1.35, 2.06 and 3.02 nm by varying this ratio from 1:1 to 10:1.

In our previous work, an FEM continuum model demonstrated higher yield with increased distance between active sites and the tube ends.[122] Therefore, in this work the termini of the SWCNT are modified with negative charges, such that a negatively charged intermediate, oxalate ($C_2H_4^-$) is electrostatically repelled before escaping into the bulk. This effect is quantified by calculating retention time, *i.e.* time span for which intermediate stays inside the SWCNT. To represent negative charges at the termini of the SWCNT, we chose carboxylate (COO^-) moieties, which are small, rigid and can be attached to SWCNT experimentally (Figure 3.2).[136] It was hypothesized that electrostatic repulsion between the SWCNT ends and the negatively-charged carboxylate intermediate would increase the intermediate residence time within the SWCNT.

3.2.1 Simulation approach

GROMACS 2018 was used for MD simulations, applying the Optimized Potential for Liquid Simulations – All Atom (OPLS-AA) force field.[125,137–141] Periodic boundary conditions (PBC) were applied to all MD simulations. The carbon nanotube/intermediate couple was first solvated with extended simple point charge model (SPCE) water molecules in a cubic box. Initial box size was determined by keeping a 1.5 nm minimum distance between the periodic boundary and the SWCNT (initial box volume ~1000 to 3000 nm^3, depending on SWCNT diameter). System energy was minimized before equilibration using the steepest descent method, followed by NVT (0.1 ns) and NPT (1.0 ns) equilibration with position restraints for both the SWCNT and the intermediate. Finally, the MD simulation was performed under NPT ensembles for 5-20 ns (2 fs timestep), repeating 30 times for each system. During the MD simulation, four carbon atoms were position-restrained, two at each end of the SWCNT, in order to fix the SWCNT in place. The system temperature was

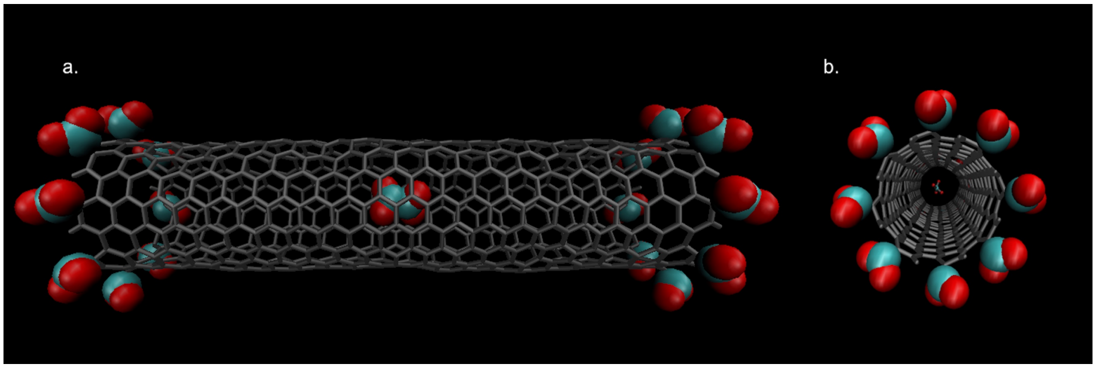

Figure 3.2 Initial configuration of a SWCNT modified with 8 carboxylate groups at the end. Oxalate intermediate at the center of SWCNT. Oxygen and carbon atoms are represented by red and green colors respectively. a) axial view b) radial view.

coupled at 300 K by a velocity rescale thermostat[142] and the pressure was kept constant at 1 bar using the Parrinello-Rahman scheme.[143] A neighbor searching algorithm used a 1 nm cutoff value for both short-range electrostatic and van der Waals interactions. Long-range electrostatic interactions were calculated using the Particle-mesh Ewald method (PME).[144] For non-homogeneous systems, the PME method can generate unwanted artifacts in systems with net charge.[145] Therefore, in order to neutralize negative charges of oxalate or/and carboxylates, fully dissociated Na^+ ions were added outside the SWCNT.[146,147] With this approach, ionic strengths ranging from 10 to 23 mM and Debye lengths from 86 nm to 64 nm were obtained. A Verlet cutoff scheme was used to calculate non-bonded interactions on a GPU accelerator.[52]

3.2.2 Data Analysis

Time-coordinate data from MD trajectories was analyzed using the python packages MDAnalysis[148,149] and GromacsWrapper.[150] This data was used to determine the simulation time at which the intermediate escapes the SWCNT, *i.e.* retention time, and to calculate diffusivity from mean-square displacement.

During MD simulation, the intermediate's initial position was chosen as the geometric center of the SWCNT, allowing the intermediate to diffuse equal lengths in either direction towards the SWCNT terminus. The mean-square displacement (MSD) was calculated as a function of lag time, τ. Three-dimensional displacement (axial and radial) of the intermediate was considered to understand the interaction between the wall and intermediate. For a three-dimensional system, the diffusion coefficient, D, can be calculated using Einstein's equation[151]:

$$D = \lim_{\tau \to \infty} \frac{[r(t+\tau)-r(\tau)]^2}{6\tau} \quad [1]$$

where τ is the lag time over which displacement occurs. Neglecting a brief induction period of ~10 ps simulation time, mean-square displacement (MSD) was calculated over the total simulation time for varying lag times. The MSD varies linearly for $0 < \tau < 100$ ps; at larger lag times, uncertainty grows due to reduced sampling.[152] Therefore, a straight line was fitted to the MSD plot over the 0–100 ps range of lag time, and diffusivity calculated from the slope of this line according to Eq. 1. In this analysis, MD trajectories in which the intermediate exited the nanotube were not considered.

The Knudsen diffusion coefficient, D_{Knudsen}, was calculated for all SWCNT diameters, d, using:[153,154]

$$D_{\mathrm{Knudsen}} = \frac{d}{3}\sqrt{\frac{8RT}{\pi M}} \quad [2]$$

where, d is the SWCNT diameter, M is the molar mass of intermediate, R the gas constant, and T the temperature. Bulk diffusivity, D_{bulk}, is defined as the intermediate diffusivity in bulk solution in the absence of SWCNT. Estimates of D_{bulk} were obtained via MD calculations using identical settings as when the SWCNT was present. Effective diffusivity, D_{eff}, is calculated as the harmonic mean of Knudsen diffusivity, D_{Knudsen}, and bulk diffusivity, D_{bulk}:

$$D_{\mathrm{eff}} = \left[\frac{1}{D_{\mathrm{Knudsen}}} + \frac{1}{D_{\mathrm{bulk}}}\right]^{-1} \quad [3]$$

The radial density function (RDF, $g(r)$) provides information about the probability of finding the molecule at a distance, r, from a reference position.[155] In this work, RDFs were calculated between the center of the SWCNT and the water molecules inside the SWCNT, as well as between the center of the SWCNT and carboxylate groups at the SWCNT termini, and normalized with the maximum density. The RDF is calculated as follows:

$$g(r) = \frac{\rho(r)}{\rho} \qquad [4]$$

where, $\rho(r)$ is the local particle density and ρ the overall particle density.

Carboxylate groups (COO^-) were attached to the SWCNT termini by replacing one or more terminal hydrogen atoms. Carboxylate carries -1 net charge for pH above 3.75. Partial negative charge is present on the oxygen atoms of carboxylate due to high electronegativity, making carboxylate a slightly polar molecule.[156] Dissolved, positively-charged sodium atoms were added outside the SWCNT in equal number to carboxylate and oxalate to maintain overall electroneutrality. This led to increasing ionic strength in the system as the number of carboxylate groups increased. Therefore, the ionic strength of the system ranged from 10.84 mM with no carboxylate end-groups to 23.02 mM with 8 COO^- per terminus.

3.3 Results and Discussion

3.3.1 Diffusivity

Molecular dynamics simulations enable tracking the movement of the intermediate inside the SWCNT. Intermediate mobility is quantified by diffusion coefficient, *D*, of intermediate inside the SWCNT.

For a nano-scale confined system, the mean free path (MFP) of molecules in the liquid phase is comparable to the length scale of the system. In such a system, particles are more likely to be influenced by Knudsen diffusion.[157,158] The diffusion coefficient can therefore quantify the effect of geometry on solute transport.

Figure 3.3 shows the average diffusion coefficient, D_{CNT}, as determined by MD simulations for intermediates (oxalate, Figure 3a and ethanol, Fig 3b) inside SWCNTs of varying diameter, *d*. As SWCNT diameter increases from 1.08 nm to 3.02 nm, the diffusion coefficient generally increases towards the bulk diffusivity. The calculated diffusivity of oxalate compares well with the estimated effective diffusivity, D_{eff}, suggesting that interactions with the nanotube wall influence transport over a broad range of *d*. In comparison, the diffusivity of ethanol shows a stronger dependence on *d*, and achieves bulk values at large nanotube diameters. This trend is further explored in the next section.

3.3.2 Density inside the CNT

MD simulations were analyzed to determine water density and radial distribution inside the SWCNT. Figure 3.5 a-c depicts water molecules inside SWCNT at diameters 1.08 nm, 1.35 nm, and 2.06 nm. This is an axial view of the nanotube, in which carbons in the SWCNT wall are blue, atoms of the oxalate intermediate are colored green, and orange

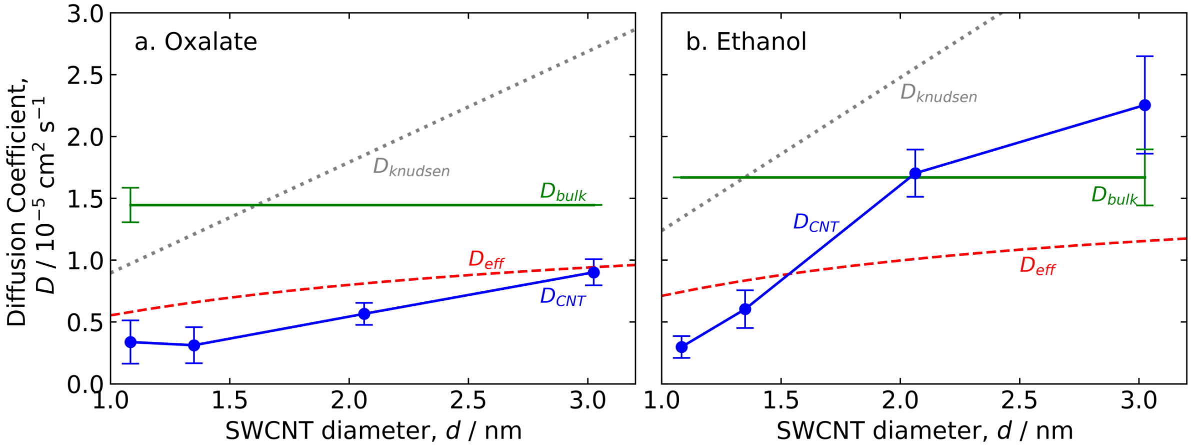

Figure 3.3 Effect of SWCNT diameter on the diffusion coefficient of a) oxalate, and b) ethanol.

indicates atoms of water molecules. Water shows a cylindrical organization structural orientation inside the SWCNT of smallest diameter i.e. 1.084 nm.

As diameter increases further, water orientation transitions to a mixture of organized and unorganized (bulk-like) structure within the 1.35 nm nanotube, and unorganized, bulk-like water structure orientation at 2.06 nm. The minimum distance between interior waters and the CNT surface is fairly constant at ~3.85 Å ± 1.19 Å for all nanotube sizes (Fig 3.4). This value is same as Lennard-Jones parameters defined for water-carbon hydrophobic interactions and reflects the hydrophobicity of the SWCNT surface.[159]

The structural transition of water observed here is describe extensively in the literature. Computational studies have indicated the presence of polygonal (n = 4 to 8) layers inside the SWCNT, referred to as shell-water, for varying Lennard-Jones parameters, temperature and water models.[125,155,160,161] However, experimental NMR and IR studies could only prove the presence of ordered water structure but not the shape.[162–165] In Figure

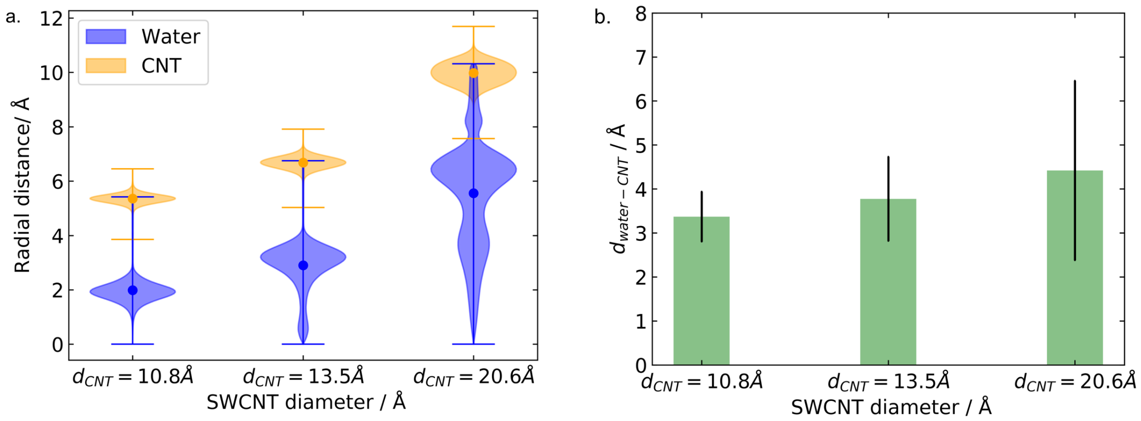

Figure 3.4 a) violin plot of radial distance of SWCNT wall and water inside the SWCNT. Shaded region is a probability density function of the radial distances. b) distance between SWCNT wall and water inside the SWCNT at different carbon nanotube diameters.

4b, shell-water with a water chain at the SWCNT centerline is observed for *d*=1.35 nm. This type of structure can form due to the change in hydrogen bonding of shell water and thus affects the water molecules at the center.[155,165,166]

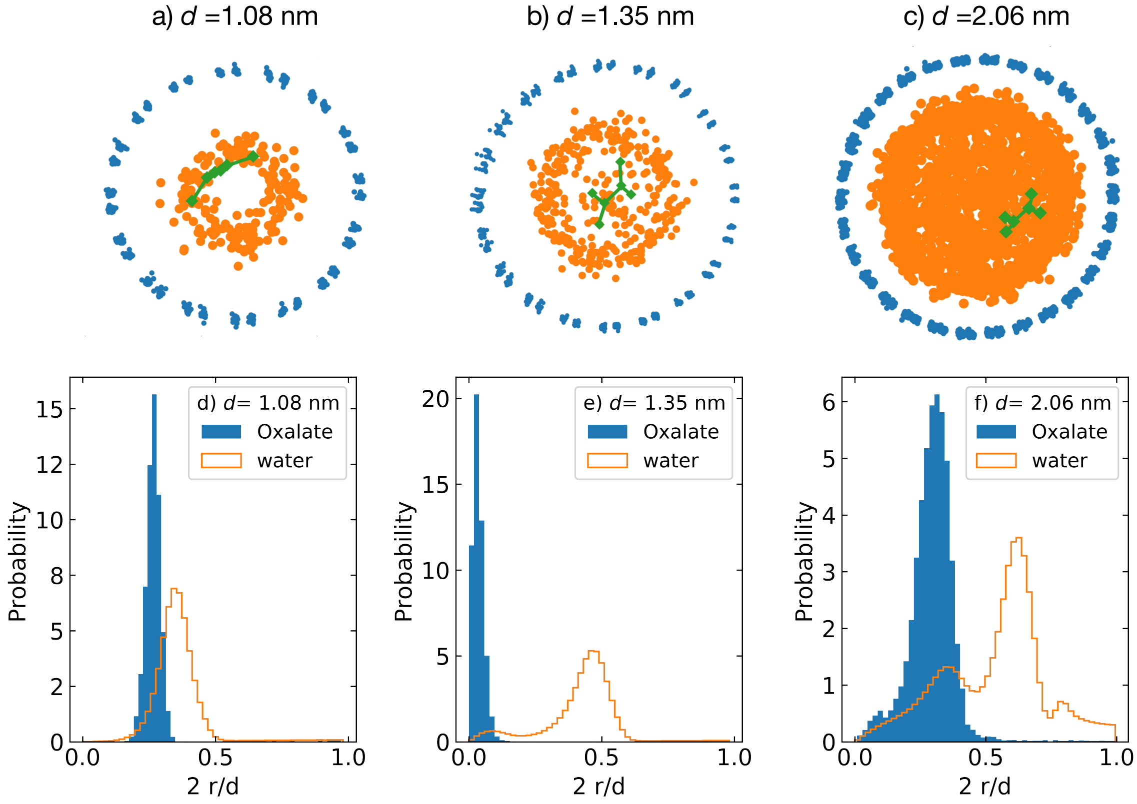

Figure 3.5 (a-c) Radial view of single walled carbon nanotube (SWCNT). Water molecules are represented by orange, SWCNT by blue and oxalate by green color. (d-f) Probability density function of water and oxalate along the radial axis.

Fig 3.5 d-f shows the probability of finding water molecules and oxalate inside the SWCNT along the radius at diameters 1.08 nm, 1.35 nm and 2.06 nm. For all diameters, the probability of finding oxlate at the radial center is higher than close to the SWCNT wall, and shell water predominates at higher radii than oxalate. Since the SWCNT cannot provide hydrogen bonding to the oxalate, oxalate prefers to be at the radial center where hydrogen

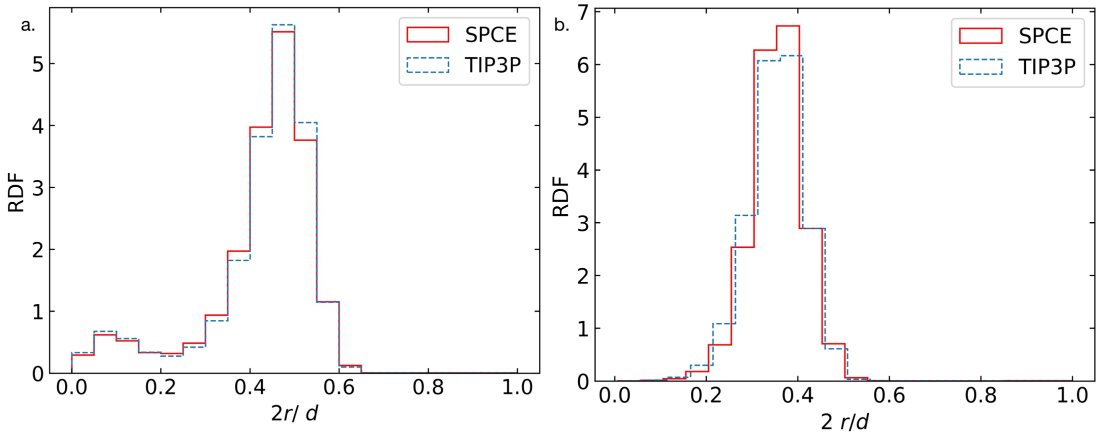

Figure 3.6. Normalized radial distribution function for SPCE and TIP3P models. a) d =1.08 nm b) d= 2.06 nm

bonding can be satisfied by chain water (*i.e.* non-shell water molecules). This indicates that shell-water might act as a solid-wall type of barrier for intermediate diffusion.

Water density inside the SWCNT was analyzed with both rigid (SPCE) and non-rigid (TIP3P) water models to eliminate error due to water models. Due to the varying rigidity of water in each model, it is possible that water inside SWCNT can show different structural configurations. Alexiadis et al. observed different water configurations for SPCE and TIP3P

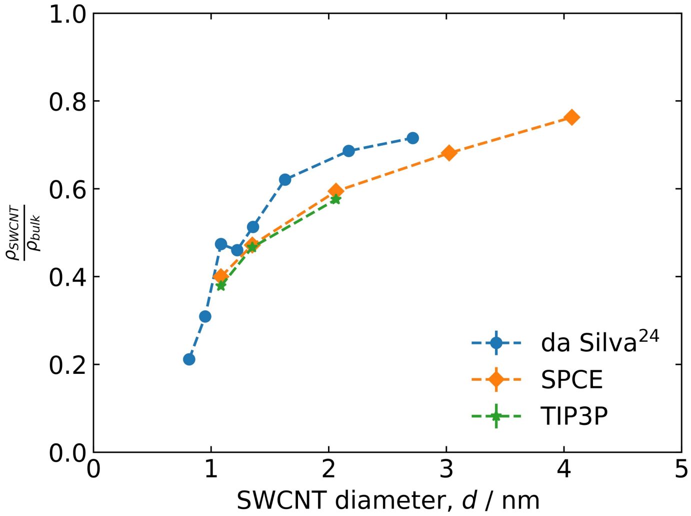

Figure 3.7 Effect of SWCNT diameter on normalized water density.

models for SWCNT of 0.89 nm.[125] In this study, we calculated the normalized radial distribution function between the center of a carbon nanotube and water molecules present inside the SWCNT for both the models. It is found that for SWCNT of diameter 1.084 nm and above, SPCE and TIP3P models showed similar results (Fig 3.6).

The configuration of water within the nanotube suggests that the intermediate does not experience a bulk-like liquid environment for SWCNT diameters below 2.06 nm. Water density inside the SWCNT was calculated from MD simulations and compared with literature results in Figure 3.7, where fair agreement is observed.[131]

3.3.3 Retention time

In order to maximize the probability that a reaction would occur at a catalytic site inside the nanotube, the time over which the intermediate is retained within the nanotube should be maximized. Retention time was studied by varying the diameter of unmodified SWCNT (i.e. no charged at the SWCNT termini) while holding the length:diameter ratio constant at 5 (Figure 3.8 a). It is found that the retention time of both the intermediates,

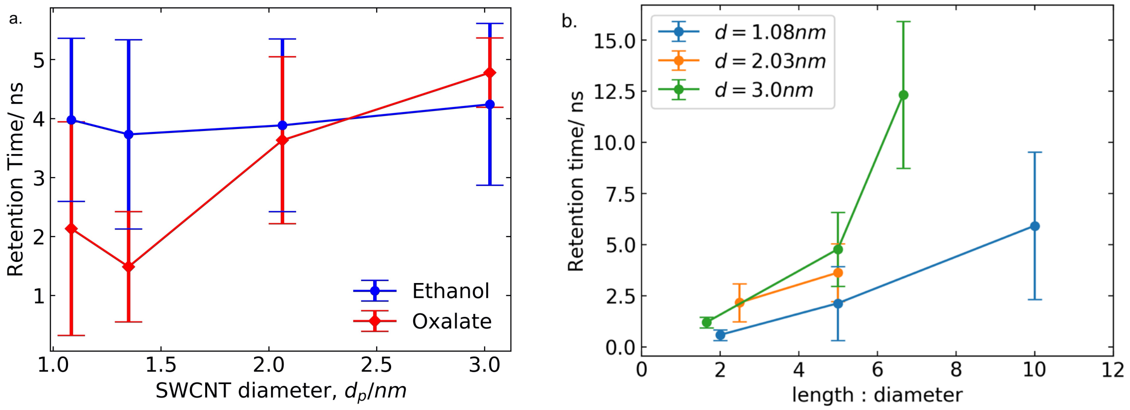

Figure 3.8 a) Retention time of intermediates (oxalate and ethanol) at different SWCNT diameter. b) Retention time of oxalate intermediate at different SWCNT diameter and length:diameter ratio. Error bars represent the standard deviation of 10 trajectories.

oxalate and ethanol, is less than 5 ns and independent of SWCNT diameter for constant length:diameter ratio.

We further studied the effect of length:diameter ratio on retention time for varying SWCNT diameter (Figure 3.8 b). At a constant diameter, retention time increased with increase in length. For the smaller diameters, and for the 3.0 nm tubes below a length:diameter ratio of 5, there is no significant effect of diameter given the range of error observed. For the 3.0 nm diameter at length:diameter ratio above 5, retention time increased significantly with increasing length and diameter. These results are consistent with retention time being proportional to diffusion time $\sim\frac{L^2}{D_{\text{eff}}}$, where L is the diffusion length and D_{eff} is effective diffusivity. The diameter only weakly affects D_{eff} via Knudsen diffusion. Hence, retention time increases primarily due to increase in length. The appearance of more bulk-like solvent in the large 3.0 diameter nanotubes may increase retention due to the enhanced three-dimensional mobility of the intermediate. For the remainder of this study the length:diameter ratio is fixed at 5:1.

One way to ensure longer intermediate retention time is to close off the SWCNT termini, to mimic tryptophan synthase's closed confirmation.[121] As a proxy for this functionality, we introduced a barrier for intermediate diffusion into the bulk by introducing repulsive charges at the SWCNT termini. The termini were modified with varying numbers of negatively charged carboxylate groups. MD simulations of 30 ns with these systems in the presence of a negatively charged oxalate intermediate as well as uncharged ethanol.

Figure 3.9 shows the effect of the presence of charged termini on the retention time of intermediates at constant SWCNT diameter of 1.35 nm. The retention time of oxalate increases from 1 to 5 ns when total terminal charge was changed from 0 to -8. This suggests that whenever oxalate attempts to exit the SWCNT, it is electrostatically repelled by the terminal carboxylates. Unexpectedly, ethanol displays significantly higher retention time in the presence of charged termini (Figure 3.9), particularly for a small amount of terminal charge, above which the retention time stays approximately constant. In the presence of terminal charges, the retention time of ethanol increased from 3.7 ns to 16.7 ns, a significantly higher sensitivity compared to oxalate. The effect of the terminal charge on the retention time was further studied using probability density calculations to observe the predominant axial locations of intermediates within the SWCNT.

The probability density of oxalate along the length of SWCNT (Figure 3.10 a) shows that as terminal charge increases, the probability of finding oxalate at the center is higher than at the termini, presumably due to increasing electrostatic repulsion from the termini.

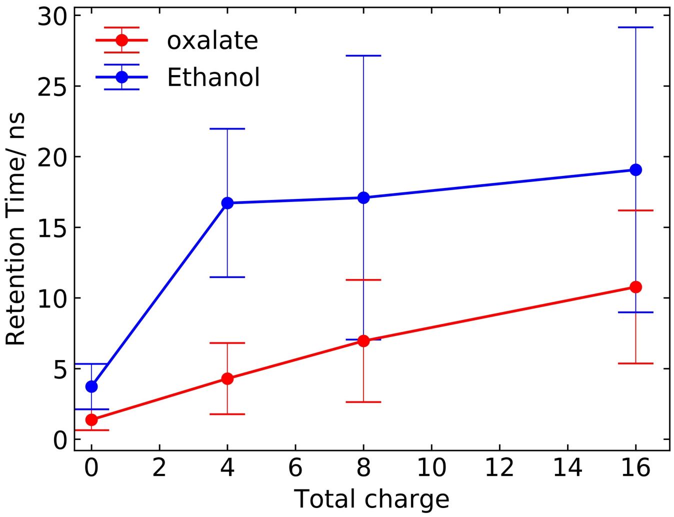

Figure 3.9 Retention time of intermediates (oxalate and ethanol) at different charge density at edges of SWCNT (d=1.35 nm).

Ethanol is a non-charged but polar molecule, and hence can be attracted to the negatively charged terminal groups. The probability of finding ethanol at the tube ends is higher than at the center and increases with increasing terminal charge, providing evidence of such attraction (Figure 3.10 b). For unmodified SWCNT, a different PDF trend was observed due to the difference in hydrogen bonding of ethanol (two hydrogen bonds) and oxalate (eight hydrogen bonds).

Electrostatically modified SWCNTs did show significant improvement in the retention time. However, the terminal carboxylate groups experienced electrostatic repulsion among themselves as the number of carboxylates increased. This resulted in a change of orientation of carboxylate such that negatively charged oxygen atom is pointed outside the SWCNT (Figure 3.2). Thus, dilution of negative charge reduced the magnitude of electrostatic forces at the tube ends. It is also important to consider the increase in ionic strength with increasing terminal charge, which affects the strength of potential fields. One possible way to address this reduction of charge density is to modify the SWCNT termini with more rigid negative charges, for example by esterifying the carbon-nanotube ends.[167]

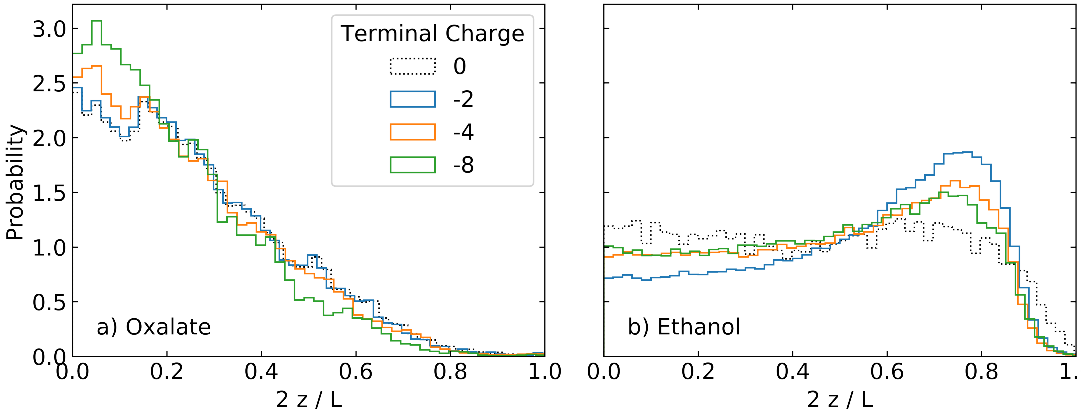

Figure 3.10 Normalized probability density function for a) oxalate and b) ethanol along the length of modified single walled carbon nanotube (d = 1.35 nm)

Consideration of reaction processes is a natural next step based on the present results. First, the effect of incorporated catalyst inside the SWCNT would necessarily affect the transport results obtained here, as would the introduction of defects in the nanotube. Both of these modifications could be modeled using classical MD approaches to account for specific molecular interactions. On the other hand, the time scale of reaction processes, typically greater than 1 ms, makes it difficult to study the kinetics of the present system using molecular dynamics. Kinetic Monte Carlo (KMC) simulation, on the other hand, can be parameterized using MD and used to study kinetics.[21,168] This approach can fill the gap between atomistic simulation and continuum modeling by considering the state to state transition of a molecule rather than following a trajectory of the molecule.[169] The results presented here can facilitate a KMC simulation in which a catalytic site is introduced within the SWCNT. Diffusion coefficients obtained via MD simulation, for example, can be applied in such a KMC model to study the time evolution of reaction and intermediate transport.

3.4 Conclusions

Intermediate transport inside a water-filled nanochannel was studied using single-walled carbon nanotube as a model structure. MD simulations reveal that intermediate inside the nanochannel follows a diffusion mode that combines molecular and Knudsen diffusion. A length:diameter ratio higher than 5 can also retain the molecule significantly. The unusual structure of water molecules inside the SWCNT plays a critical role in intermediate transport at smaller SWCNT diameters, where water showed ice-like ordered structure that restricts intermediate transport to the nanotube center. However, retention time can be increased by functionalizing the SWNT termini with an electrostatic charge, even if the intermediate is uncharged.

Chapter 4

A multi-scale modeling study of CO_2 electroreduction on a single metal atom catalyst[‡]

4.1 Introduction

With the alarming speed of climate change, a solution to global warming has become an urgent need.[57] Atmospheric CO_2 has been proven to be the single most climate-relevant greenhouse gas that plays a major role in temperature rise.[170] As of 2020, the concentration of CO_2 has increased from 280 ppm in preindustrial times to 413 ppm and will continue to increase due to increasing human activities.[171] The open-loop industrial processes in industry are one of the major CO_2 emitting sources. Controlling CO_2 gas emissions at the source by converting it into value-added chemicals such as alcohols and hydrocarbons could be one solution to solve the global warming problem. CO_2 capture and conversion (CCC) into hydrocarbons not only closes the open loop processes but also provides an alternative to fossil fuels. Hence, it is important to find a sustainable and cleaner way of reducing CO_2 into chemicals. Existing carbon-neutral energy sources such as renewables and nuclear provide energy as electricity. This enables electrochemistry, as a potentially viable option to reduce CO_2 to chemicals.

CO_2 can be reduced to a variety of chemicals such as alcohols and hydrocarbons (Figure 4.1). A significant effort has been put into the discovery of efficient metal catalysts for carbon dioxide reduction reactions (CO_2RR) that inhibit the competing hydrogen evolution reaction (HER) and provide high selectivity and faradaic efficiency towards

---

[‡] Some excerpts of this chapter are published as Asset, T.; Garcia, S. T.; Herrera, S.; Andersen, N.; Chen, Y.; Peterson, E. J.; Matanovic, I.; Artyushkova, K.; Lee, J.; Minteer, S. D.; et al. Investigating the Nature of the Active Sites for the CO2 Reduction Reaction on Carbon-Based Electrocatalysts. *ACS Catal.* **2019**, *9* (9), 7668–7678, doi:10.1021/acscatal.9b01513.

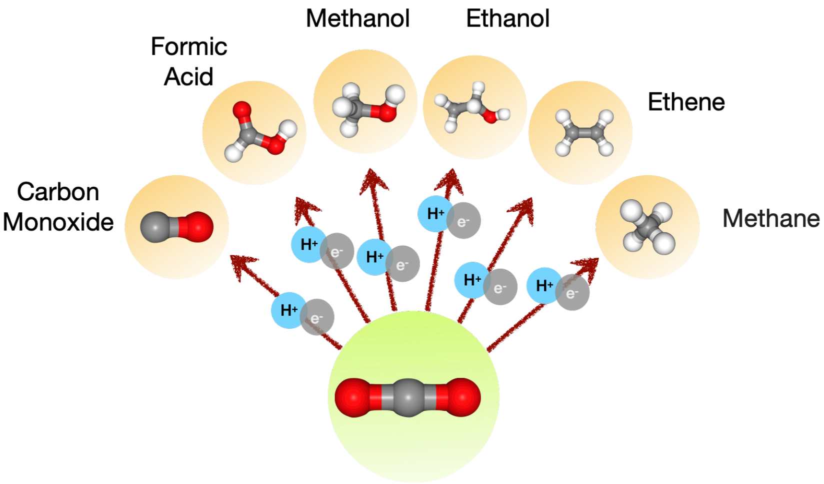

Figure 4.1 A schematic of a conversion of CO_2 into value-added chemicals.[175]

desired products (formate and CO or alcohols and hydrocarbons).[63] Gold[70,172] and silver[71–73] based catalysts reduce CO_2 to CO at high faradaic efficiency and selectivity. CO can be reduced further to hydrocarbons such as methane and ethane on a Cu based catalyst by inhibiting HER.[173–179] The reduction of CO_2 to formate was evident on Pb and Sn catalysts.[65]

Recently, single-atom metal-centered carbon-based catalysts (M-N-C) have been explored because of the atomically dispersed nature of active sites that increases selectivity towards CO formation.[74–80,84–86,180,181] Faradaic efficiency of CO formation vs. HER is varied from 10 – 90 % depending on different synthesis techniques. But high selectivity and a low range of products make M-N-C catalyst an attractive option to optimize further, for example to produce syngas (CO/H_2) in industry.

Recently, our collaborators at the University of Irvine, California, synthesized a library of atomically dispersed metal centered catalysts by the sacrificial support method (SSM).[182–184] In SSM, usually silica is used as a template to deposit precursors via pyrolysis. This synthesis introduces distant single-atom active sites and reduces the probability of C-C bond formation which requires high proximity of active sites. Also, M-N-C has shown promising results of inhibiting HER due to the absence of hollow binding sites for proton adsorption increasing the selectivity towards CO_2RRs.[181]

Due to the complex nature of the CO_2 reduction reaction mechanism, a mechanistic understanding of a catalytic system has become a requirement to further optimize catalytic performance and design better catalysts.[94] A Multi-scale simulation framework that captures atomistic insights via DFT studies, coupled with microkinetic modeling will provide a clear understanding of CO_2RR and the heterogeneous reaction that includes the surface processes such as reaction and adsorption.

Computationally, microkinetic modeling has been used to study reaction mechanisms and the most favorable pathway for CO_2RR on various catalysts. Liu et. al. developed a microkinetic model to validate the pH effect on CO_2RR on Cu surfaces via Tafel analysis.[106] However, Shinagawa et. al. demonstrated the importance of surface coverage in microkinetic modeling over the Tafel analysis.[107] Work of Bart et. al. provided potential dependent product distribution on Cu surfaces and reported that the formation of COOH* is a critical step for selectivity towards CO and CH_4 formation.[108] Singh et. al. provided a multiscale simulation framework consists of MD+DFT, microkinetic modeling, and continuum modeling to validate partial current densities of CO_2RR with experimental data over Ag surface.[94] A microkinetic model was used to study the formation of the C_2 hydrocarbon pathway by considering the effect of the electrolyte polarization to correct the free energies obtained from DFT simulations for accurate kinetics prediction.[185] The effect of an electric field generated in the electrolyte on the surface coverage of the CO_2RR catalytic system on Ag was studied by Chen et.al.[110] As per our knowledge, multi-scale modeling of MNC catalyst has not been reported in the literature yet.

In this work, we explore experimental results presented by Asset et. al., using microkinetic modeling for a better understanding of the CO_2 reaction mechanism on the M-N-C catalyst.[74] We aim to develop a model to predict partial current densities of CO and H_2 formation. We have chosen Fe-N-C catalysts to model from the library of Cr, Ni, Co, Mo, Cu, and Zn centered catalyst synthesized as it has shown the highest faradaic efficiency at low overpotentials (50 % at -0.435 V vs RHE).[74] (Figure 4.2) We proposed the most favorable path for the CO_2 reduction reaction based on the product formed (CO and H_2) in the experiment. Free energy of the reaction and the transition state is then calculated via DFT to estimate the rate of each elementary reaction. The electrode potential dependent activation energy barrier was calculated by applying the CHE model via Butler-Volmer formalism.[186,187] These estimated potential dependent rate constants were then used as an

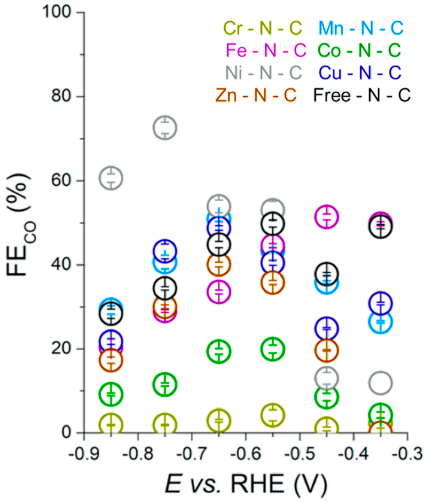

Figure 4.2 Faradaic efficiency of M-N-C catalysts (M = Cr, Mn, FE, Co, Ni, Zn, Cu, Free).[74]

input to a microkinetic model and a linear sweep voltammetry curve (LSV) was simulated to validate the experimental data.

Finally, in complex catalytic systems, identifying the rate determining step (RDS) helps to improve the rate of the reaction by modifying the catalyst, changing the electrolyte or molecular structures. However, in the absence of a single RDS, sensitivity analysis of the model helps to determine which transition state energies and intermediates are controlling the rate of the reaction. In the present model, such a sensitivity analysis was performed by calculating the degree of rate control (DRC).

4.2 Methods

4.2.1 Experimental Methods

4.2.1.1 Material synthesis

A library of MNC catalyst with different metal centers, M = Cr, Mn, Fe, Co, Ni, Cu, Zn was synthesized by our collaborator at UC, Irvine.[74] A schematic of the synthesis process is shown in Figure 4.3.

4.2.1.2 Material Characterization

The specific surface area of each sample was calculated using the Brunauer–Emmett–Teller (BET) isotherm.[188] Nitrogen gas adsorption and desorption were measured by a Micromeritics ASAP 2020. A sample was degassed for 6 h before the measurements. To measure smaller pore sizes, we used a 0.17846 mol/g dosing amount of N_2. Physisorption isotherms were analyzed for pore size distribution using the Barrett, Joyner, and Halenda (BJH) theory as well as DFT. For DFT, the microscale geometry of the pore network was considered to be undefined, consisting of both spherical and cylindrical pores. To estimate pore size distribution, the pore network model of Ustinov et al.[189] was then

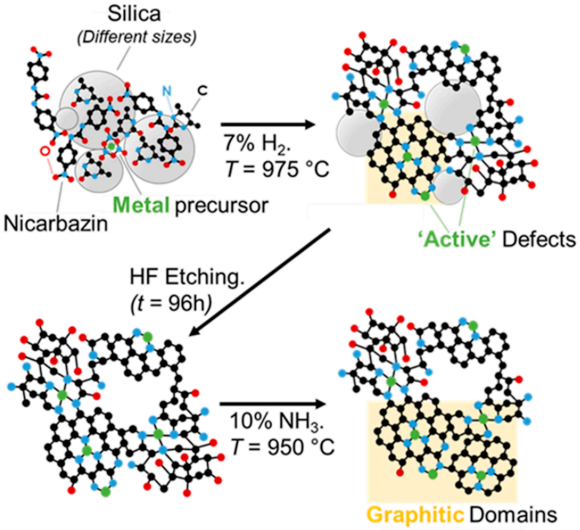

Figure 4.3 A schematic of MNC catalyst synthesis using sacrificial support method.[74]

considered. It uses a slit geometry but also includes surface adsorption parameters of a non-graphitic carbon.

4.2.2 Reaction Mechanism

Atomically dispersed metal centers in carbon-based catalysts have shown higher selectivity towards the $CO_2 \rightarrow CO$ conversion .[74,190] Hence, we limited our reaction mechanism to the formation of CO. Surface adsorption and desorption of the products was neglected to reduce the number of equations. However, adsorption/desorption of the products will change the reaction driving force and hence will be considered in the next phase of the model. We considered the following two-step reaction mechanism for CO_2RR:

$$\ast + CO_2 + H^+ + e^- \underset{k_{-1}}{\overset{k_1}{\rightleftarrows}} COOH\ast \quad [1]$$

$$COOH\ast + H^+ + e^- \overset{k_2}{\rightarrow} CO + H_2O \quad [2]$$

For HER, Volmer-Heyrovsky, a single site reaction mechanism was considered as follow[94]:

Volmer $$ ❋+H^++e^- \underset{k_{-3}}{\overset{k_3}{\rightleftarrows}} H❋ \quad [3] $$

Heyrovsky $$ H❋ + H^+ + e^- \overset{k_4}{\rightarrow} H_2 \quad [4] $$

4.2.3 Computational method

We followed the DFT calculation method described by Asset et.al. for optimizing the geometries of reactants, products, and intermediates (COOH❋, H❋, and M-N-C surfaces).[74,79] All DFT calculations were performed using GPAW and ASE python packages.[191–193] Generalized gradient approximation (GGA) with RPBE functional and projector augmented- wave pseudopotentials were implemented to calculate electronic structures of the chemical species. A γ-centered 8 × 8 × 1 k-mesh and Fermi-smearing with σ set to 0.03 were used to calculate electronic energies. In all cases, plane-wave basis cutoff was set to 800 eV. Transition state energy was calculated using the climbing image nudged elastic band theory (Cl-NEB).[194] Cl-NEB finds the minimum energy pathway (MEP) between reactants and products. A structure with maximum energy along the MEP pathway is then assumed to be a transition state. Gibbs free energy of all the species were calculated by adding electronic energy (E_{DFT}), zero point energies (ZPE), heat capacities (Cp) and entropies(-TS) calculated by using Harmonic oscillator approximation as follow.[195]

$$ G = E_{DFT} + ZPE + \int Cp\, dT - TS \quad [7] $$

Gibbs free energy of activation and reaction for each elementary step is then further used to calculate the forward rate constant (k) and equilibrium rate constant (K), respectively.

4.2.3.1 Potential dependent rate constant calculation

Gibb's free energy of an electrochemical reaction is calculated using the computational hydrogen electrode (CHE) model.[186] For a potential-dependent chemical reaction:

$$\mathrm{A}\ast + \mathrm{H}^+ + \mathrm{e}^- \rightarrow \mathrm{AH}\ast \qquad [8]$$

where, * denotes surface adsorbed species. Gibb's free energy of the reaction was calculated using following an equivalent non-electrochemical reaction.[186]

$$\mathrm{A}\ast + \mathrm{H}\ast \rightarrow A\mathrm{H}\ast \qquad [9]$$

By using the CHE model, the electrode potential dependent Gibb's free energy of the reaction was calculated by setting a reference electrode relative to the reversible hydrogen electrode (RHE). In this approach, the chemical potential of hydrogen and the electron (H^+ + e^-) is set to be equal to the chemical potential of a hydrogen molecule (H_2) at 0 V and all pH values. Change in electrode potential (V) can be translated to the free energy by applying a linear shift in potential by -eV, where e is an elementary charge and V is an electrode potential. Therefore, Gibb's free energy of reaction 7 can be written as follow:

$$\Delta G_r(V) = G_{A\mathrm{H}\ast} - G_{\mathrm{A}\ast} - \tfrac{1}{2} G_{H_2} + eV \qquad [10]$$

At the equilibrium potential, U, the chemical potential of adsorbed species, AH$\ast$, is equal to the chemical potential of proton adsorption, H$\ast$. We calculated the equilibrium potential, U, by setting the Gibbs free energy of reaction 7 to zero in equation 9.

$$\mathrm{U} = \frac{-[\, G_{A\mathrm{H}\ast} - G_{\mathrm{A}\ast} - \frac{1}{2} G_{H_2}]}{e} \qquad [11]$$

By presuming that electron transfer occurs when nuclei reach the transition state, we can assume the transition state energy of reaction 8 is the same as reaction 7.[187] The transition state energy, $\Delta G_{TS}(V)$, of reaction 8 can be obtained using standard DFT approaches such as NEB calculations and referred back to the reaction 7.

Now, $\Delta G_{TS}(V)$ at any electrode potential, V, is calculated by Butler-Volmer formalism[186] as follow:

$$\Delta G_{TS}(V) = \Delta G_{TS}(U) + \beta \mathrm{F}(\mathrm{V} - \mathrm{U}) \qquad [12]$$

Where, β is a reaction symmetry factor (assumed 0.5 here), U is an equilibrium potential of reaction 1 and F is the Faraday's constant. By using transition state theory, the forward rate constant, k_i, and equilibrium rate constant, K_i, of an elementary reaction, i, can be written in the form of Arrhenius equation respectively as follow:

$$k_i = A_i \, e^{(-\frac{\Delta G_{TS}(V)}{k_B T})} \qquad [13]$$

$$K_i = \, e^{(-\frac{\Delta G_T(V)}{k_B T})} \qquad [14]$$

Where, A_i is a preexponential factor, k_B is the Boltzmann's constant and T is the absolute temperature of a reaction. The pre exponential factor, A_i, is calculated using the following equation:[196]

$$A_i = \frac{k_B T}{h} \qquad [15]$$

Where h is the Planck's constant.[196]

4.2.3.2 Microkinetic model

In this model, we develop a set of differential equation/ rate laws that can be solved simultaneously using numerical methods. The rate expressions of the elementary reactions from 1 to 4 are as follow:

$$r_1 = k_1(\theta C_{CO_2} C_{H^+} - \frac{1}{K_1}\theta_{COOH*}) \qquad [16]$$

$$r_2 = k_2 \theta_{COOH*} C_{H^+} \qquad [17]$$

$$r_3 = k_3\ (\theta C_{H^+} - \frac{1}{K_3}\theta_{H*}) \qquad [18]$$

$$r_4 = k_4 \theta_{H*} C_{H^+} \qquad [19]$$

Under a CO_2 saturated condition and at the experimental condition (1 bar and room temperature) the concentration of CO_2 in water was assumed to be 0.033 M.[197] At a pH = 7.5, the concentration of H^+ ions was 3.16 x 10^{-8} M (10^{-pH}). In a dilute aqueous electrolyte concentration of water was assumed to be 55.5 M. As a first assumption we considered all surface reactions to have reached to quasi-steady state when the potential is varied. This assumption makes the time derivative of the adsorbed species almost zero at a given potential.

Mass balance for adsorbed protons, H❋ is given by

$$-r_3 - r_4 = 0 \qquad [20]$$

$$\theta_{H*} = \frac{k_3\ \theta C_{H^+}}{\frac{k_3}{K_3} + k_4 C_{H^+}} \qquad [21]$$

Similarly, mass balance on COOH❋ yields,

$$\theta_{COOH*} = \frac{k_1\,\theta C_{CO_2}\,C_{H^+}}{\frac{k_1}{K_1}+k_2\,C_{H^+}} \qquad [22]$$

and fractional coverage of vacant sites (❋) is given by site balance as follow:

$$\theta_{COOH*} + \theta_{H*} + \theta = 1 \qquad [23]$$

The set of equations 20,21 and 22 was then solved simultaneously to find the fractional coverage of vacant sites, COOH❋, and H❋. These obtained values of θ_{COOH*}, θ_{H*} and θ were then substituted back in equations 15 and 17 to calculate the rate of CO and H_2 production respectively.

$$r_{CO} = r_2 \qquad [24]$$

And

$$r_{H_2} = r_4 \qquad [25]$$

Partial current densities of CO and H_2 were calculated further by using the following equations:

$$i_{Co} = -2\,F\,r_{CO} \qquad [26]$$

And

$$i_{H_2} = -2\,F\,r_{H_2} \qquad [27]$$

4.2.4 Sensitivity Analysis

The sensitivity analysis of the model was performed by measuring the degree of rate control (DRC) that quantifies the relative change in the rate of reaction, i by a differential change in the rate constants of reaction, j (where, $i \neq j$) as follows:[108,198]

$$DRC_i = \left(\frac{\delta\,(\ln r_i)}{\delta(\ln k_j)}\right)_{i\neq j,K_i} \qquad [28]$$

where, r_i is the rate of i^{th} elementary reaction, k_j is the forward rate constant of j^{th} reaction. K_i is the equilibrium constant of i^{th} reaction which was held constant while determining DRC_i. It must be noted that the rate constants were defined as a function of Gibbs free energy as depicted in equation 13. Thus, DRC can also be defined in terms of differential change in the transition state energy as shown below:

$$DRC_i = \left(\frac{\delta\,(\ln r_i)}{\delta\left(\frac{\mathrm{G_j^{TS}}}{RT}\right)}\right)_{i\neq j,K_i} \qquad [29]$$

where, G_j^{TS} is the transition state energy of the j^{th} reaction.

4.3 Results and Discussion

4.3.1 Morphology of M-N-C catalysts

The catalyst material was analyzed by scanning electron microscopy (SEM), physisorption isotherms (BET), abberation-corrected scanning transmission electron microscopy (AC-STEM), x-ray photoelectron spectroscopy (XPS), Raman analysis, and x-ray powder diffraction (XRD) revealing information about the surface morphology, the crystalline size, and dispersed metallic atoms. All the characterizations were performed by UC, Irvine except BET analysis. More details about the SEM, AC-STEM, XPS, XRD, and Raman spectroscopy are mentioned in ref. 18.

Here, we present results obtained from the surface analysis of the catalysts using N_2 physisorption at Michigan State University. The morphology of the M−N−C electrocatalysts

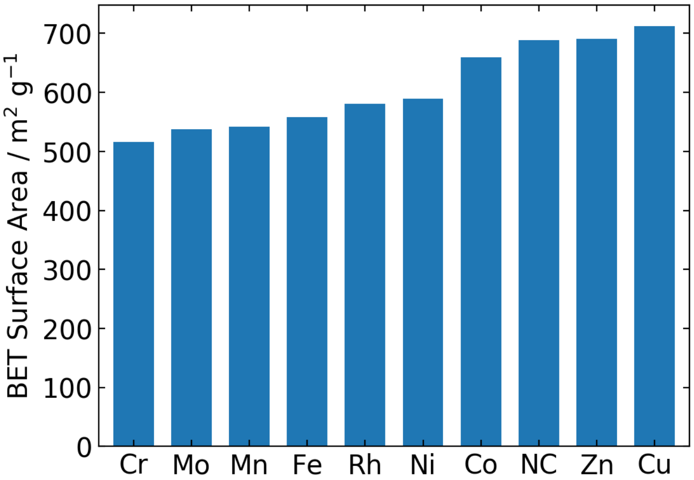

Figure 4.4 BET surface area of M-N-C catalysts (M =Cr, Mo, Mn, Fe, Rh, Ni, Co, Zn, Cu, Free)

is described in Figures 4.4 and 4.5. All materials exhibit a porous structure with a wide range of porosities (Figure 4.5 a-b) and a specific surface (calculated by N2 adsorption, using DFT and the slit- pores model, Figure 4.4) ranging from 516 m^2 g^{-1} (Cr−N−C) to 712 m^2 g^{-1} (Ni−N−C). Bet surface analysis indicates type I, N_2 adsorption isotherms which are primarily a result of the microporous nature. We also observed hysteresis which indicates the presence of mesopores. (Fig 4.6)

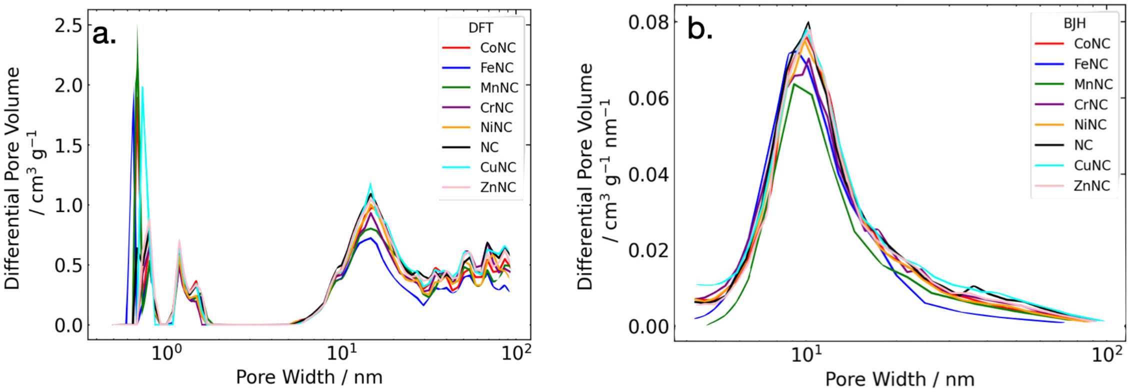

Figure 4.5 Pore size distribution of single metal atom catalysts via a) Density Functional Theory (DFT) and b) the Barrett, Joyner, and Helenda (BJH) theory

4.3.2 Estimation of Gibb's free energy and transition state energy of the reaction:

In Figure 4.7, the relative free energy of each species of proposed CO_2RR and HER is plotted with respect to (CO_2 +❋) and free surface, respectively. The binding energy of CO_2 with a metal center of an Fe-N-C catalyst is 0.40 eV which corresponds to weak CO_2 adsorption. The XPS spectra of atmospheric CO_2 on Fe-N-C catalyst also suggests that CO_2

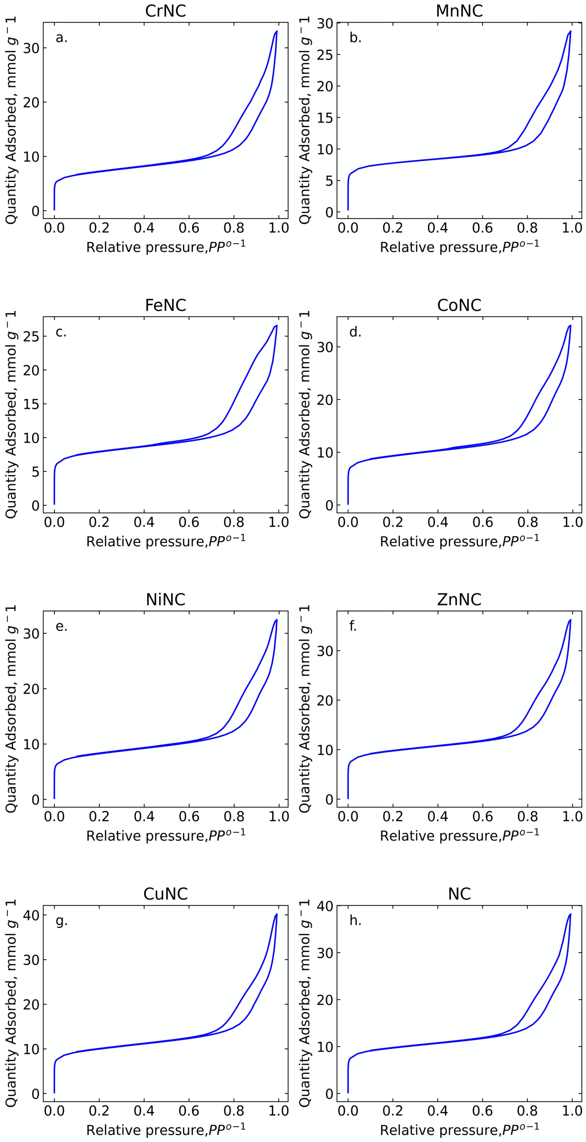

Figure 4.6 N_2 adsorption isotherms for the single metal atom catalysts. a) Cr-N-C, b) Mn-N-C, c) Fe-N-C, d) Co-N-C, e) Ni-N-C, f) Zn-N-C, g) Cu-N-C and h) Free-N-C

strongly adsorbs on the pyridinic N instead of the Fe atom.[74] Therefore, we propose that proton and electron transfer and CO_2 adsorption occurs simultaneously to form COOH❋ at the Fe atoms. Such a proton coupled electron transfer (PCET) requires high energy and slows the reaction (ΔG_r =0.605 eV). [180] Subsequent proton and electron transfer to form CO❋ is a downhill reaction with ΔG_r =-1.119 eV. (Figure 4.7a)

The free energy diagram of the hydrogen evolution reaction shows ΔG_r of 0.25eV for each proton addition (Figure 4.7b). Such a low energy barrier suggests that Fe-N-C strongly catalyzes HER. Relative free energy values for CO_2RR and HER are in good agreement with Menisa L. T. et al.[199]

Figure 4.8a shows the optimized structures of the reference state (CO_2 + H❋), transition state, and product (COOH❋) used to calculate the activation energy of COOH* formation. The activation energy of $CO_2 \rightarrow$ COOH❋ is 1.89 eV at U = 0.61 V vs RHE. Such a high transition energy to transfer H from the surface could be because of the absence of water molecules in the simulation. For Cu catalyst, water-assisted proton transfer has

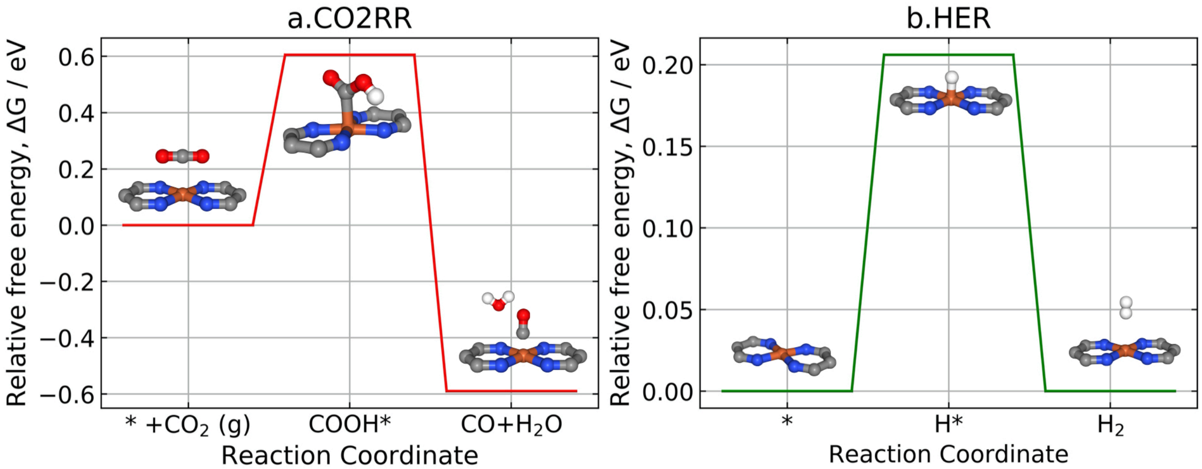

Figure 4.7 DFT calculated free energy diagram for a) the carbon dioxide Reduction to CO and b) and hydrogen evolution reaction.

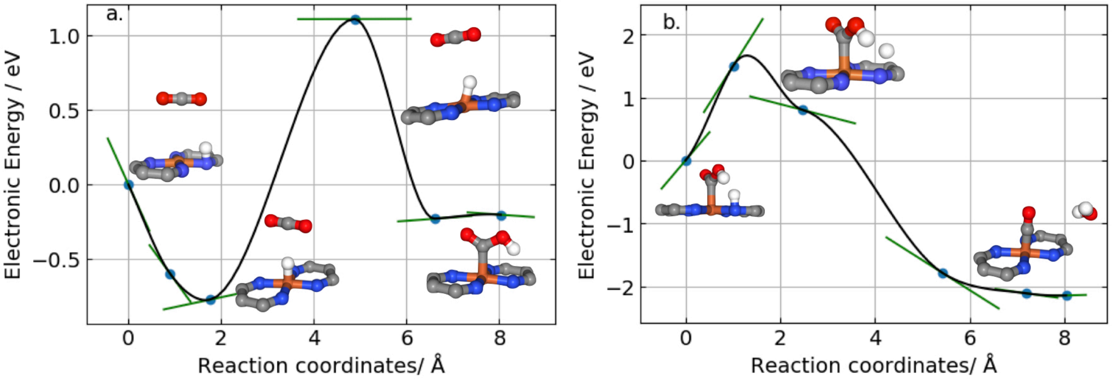

Figure 4.8 NEB profiles of for elementary reactions of carbon dioxide reduction reactions on Fe-N-C catalyst a) ❋+CO_2+H^++ e^- ⇌ COOH❋ and b) COOH❋ + H^+ + e^- → CO + H_2O.

resulted in lowering the transition state energy because of the stabilized charge separation.[186] To understand the effect of the water molecule in proton transfer, further study is required with explicit water molecules.

A transition state search for the COOH❋→ CO is shown in Figure 4.8b. CO❋ is a stable configuration (binding energy = -1.93 eV) and therefore for the transition state energy calculation we used CO❋ as a product. However, to reduce the complexity of the microkinetic model, we have assumed that CO desorbs as soon as it forms. After the

Table 4.1 Parameters to estimate potential dependent reaction energies, ΔG_{TS}, and activation energies, ΔG_r

Elementary Reaction	**ΔG_r (eV)**	**U (V vs RHE)**	**ΔG_{TS} (eV)**
$* \ +CO_2 + H^+ + e^- \ \leftrightarrow COOH^*$	-0.605	0.61 V	1.108
$COOH^* + H^+ + e^- \ \longrightarrow CO * \ +H_2O$	-1.119	1.12 V	1.667
$* +H^+ + e^- \ \leftrightarrow H^*$	-0.252	0.25 V	1.72*
$H^* + H^+ + e^- \ \longrightarrow H_2$	0.252	-0.25 V	1.56[206]

* Value is expected from the NEB calculations and will be reported as soon as the simulations are available.

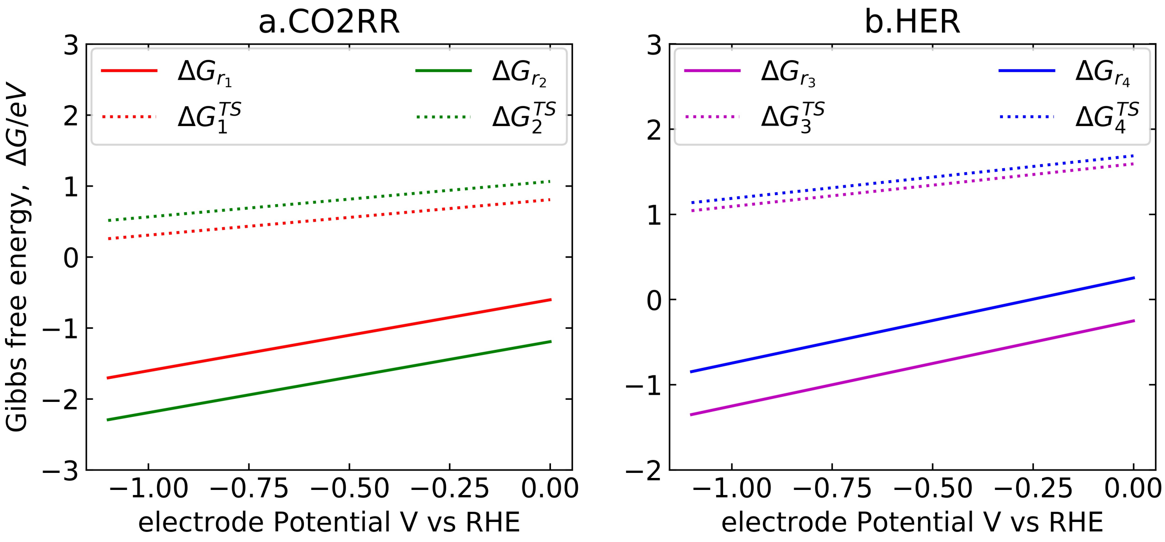

Figure 4.9 Potential dependent activation free energies (ΔG^{TS}) with α=0.5 and reaction energies (ΔG_r) for a) CO2RR (subscript 1 and 2) b) HER (subscript 3 and 4)

formation of COOH, the second step of CO_2RR occurs in the PCET manner and the transition state energy of COOH✻→ CO✻ is 1.66 eV at U = 1.105 V vs. RHE.

Further, the potential dependent linear shift in Gibbs free energies of the reaction and activation at a constant charge transfer coefficient, $\beta = 0.5$ were calculated using Eq. 9, 10, and 11 for CO_2RR (Figure 4.9a) and HER (Figure 4.9b). Parameters used to construct Figure 4.9 are given in table 4.1. The current value of the transition state energy (ΔG_{TS})of the formation of H*, in the Volmer step was estimated value and acting as a placeholder for the model. This value will be replaced by a DFT calculated value, once the ongoing NEB simulations converges. In the next section, we report results of a microkinetic model based on this estimated value to provide preliminary results.

4.3.3 Potential-dependent Fractional surface coverage of surface species

The potential dependency of surface coverage and current density is illustrated in Figure 4.10. These calculations neglect mass transport of the species and surface desorption of the products. We also assumed that CO_2 concentration near the electrode surface is in equilibrium with 1 atm gaseous CO_2 and remains constant due to a constant CO_2 gas supply. Figure 4.10a shows the current densities of combined CO_2RR and HER as a function of applied potential. Simulated current density is 4 orders of magnitude lower than the experimentally observed current density.

Figure 4.10b shows the potential-dependent fractional surface coverage for the surface species. At lower potential, COOH❋ formation is the dominant species over H❋. As potential increases, H❋ dominates the surface coverage (starting at -0.3 V vs RHE) because of the downhill reaction energies due to lower free energy (ΔG_r= 0.25eV).[180]

The discrepancy in the experimental and current modeled results could arise due to many reasons. Effect of explicit water on the transition state energy were not considered in our current calculation. Zijlstra et.al. observed a change in the transition state energy due to hydrogen bonding interactions.[108] Water molecules help to stabilize the electron cloud and lowers the transition state energy. More accurate results can be achieved by

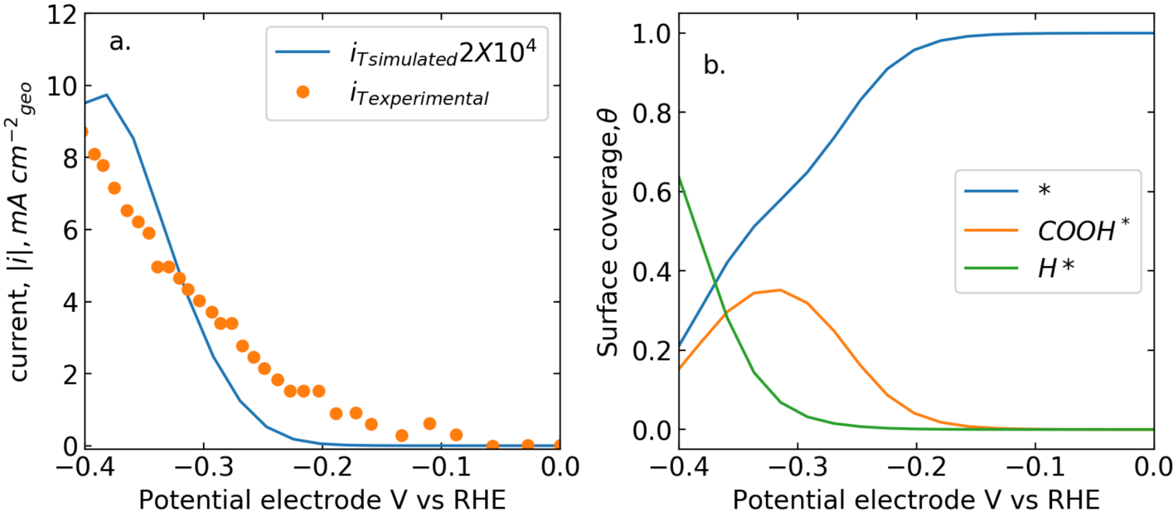

Figure 4.10 a) Comparison of simulated and experimentally measured total current densities ($\alpha = 0.5$). Simulated current is multiplied by the factor of 2 x10^4 b) Potential dependent fractional surface coverages of vacant ($*$) and adsorbed intermediate species (COOH^*, H^*) .

considering explicit water molecules and buffer molecules to reflect experimental electrolyte environment near surface.[94]

In absence of mass transport of the chemical species in the model might have overestimated the surface concentration of protons, reactants and products. It has been found that diffusion limitations alter the reaction rate and product distribution.[94] The full reaction dynamics can be studied by coupling microkinetic model with the continuum transport model. Mass transport limitations can be removed in the experiments by using rotating disc electrodes.[108]Lastly, CO❋ plays a very important role to form CH_4. Neglecting CO❋ might result in a higher probability of vacant sites to compete with HER. One can

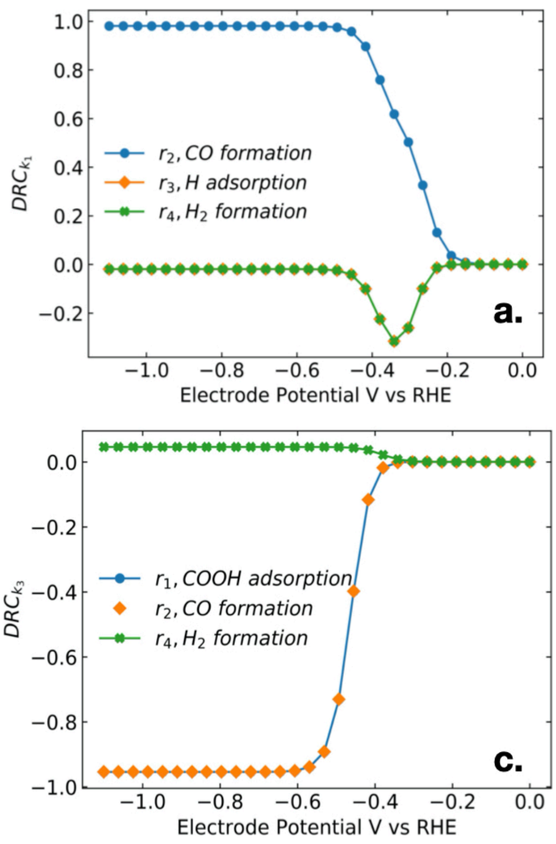

Figure 4.11 Degree of rate control with respect to a) rate constant for COOH adsorption (k_1), b) rate constant for CO formation (k_2), c) rate constant for H adsorption (k_3), and d) rate constant for H_2 formation (k_4)

assume a pseudo-equilibrium state of surface adsorption and desorption to account for the effect of CO❋.

The sensitivity analysis of the model using DRC is depicted in Figure 4.11 (a-d). In each of the subplots, the effect of a differential change in the rate constant of each reaction (k_j) on the reaction rates r_i (where $i \neq j$), has been shown by plotting DRC_i with respect to k_j as a function of electrode potential. The absolute numeric value of DRC is a measure of how sensitive the elementary reaction is to a specific rate constant. A positive or negative sign indicates whether the rate of elementary reaction positively increases or reduces with the increase in a rate constant. The potential range was varied from 0 to -1 V vs RHE. The results were analyzed at three potential subranges: a) low (0 V to -0.2 V vs RHE), b) medium (-0.2 V to -0.6 V vs RHE) and c) high (-0.6 V to -1.1 V vs RHE).

At low potentials, the forward rate constant of CO formation, k_2, controls the COOH* adsorption, r_1 (Figure 4.11b). Similarly, H adsorption is controlled by the rate constant, k_4, of subsequent H_2 formation reaction. (Figure 4.11d) The rate constants for COOH❋ adsorption, k_1, and H❋ adsorption, k_3, do not exert control on any of the reaction rates in this potential range, as shown by the zero DRC value. (Figure 4.11 a and c). The control of k_2 and k_4 on the two-adsorption reaction can be explained by the high concentration of vacant sites and minimum surface coverages of H and COOH.

At high potentials, the rate of CO formation, r_2 is controlled by k_1 and k_3. (Fig 4.10a-c). k_3 also controls the rate of the COOH* adsorption, r_1 .(Figure 4.11c) Also Figure 4.10d shows that r_3 is controlled by k_4 in this potential range. Again, k_2 has no control on any of the reaction rates. (Figure 4.11b). Overall extent of control of k_1, k_3 and k_4 on CO_2RR and HER is attributed to the minimal COOH coverage, negligible vacant sites and Maximum H coverage. (Figure 4.10b and Figure 4.11 a, c and d). Distinction must however be established between the positive control of k_1 and k_4, and negative control of k_3. (Figure 4.11 a and c)

At medium potential ranges, the transient nature of DRC was observed. As potential increases, the extent of control of k_1 on r_2 increased while its control on r_3 and r_4 passed through a minima at ~ -0.35 V vs RHE. A reverse trend was seen for the extent of control of $k_2$where increase in the potential reduced its control on r_1. Again, its control on r_3 and r_4 passed through a maxima at ~ -0.35 V vs RHE. Fig 4.11 C shows that the degree of control of k_3 on r_1 and r_2, steeply decreases with increase in the potential. In comparison its control on r_4 is negligible as shown by the very slight increase in DRC with an increase in potential. An exact opposite trend was observed in regard to the control of k_4. As potential increased the extent of control of k_4 on r_2 and r_3 increased greatly. The sudden variations observed in the DRC's compliments the transient nature of surface coverages observed in Fig4.10b. As the surface coverage of COOH passes through a maximum and hydrogen coverage starts increasing rapidly, there is a greater interaction between all rate constants. This behavior also indicates the competitive nature of CO_2RR and HER.

Similarly, H adsorption is controlled by the rate constant of subsequent H_2 formation reaction, k_2. (Fig 4.11d) The rate constant for COOH❋ adsorption, k_1, and H❋ adsorption, k_3, do not exert control on any of the reaction rates in this potential range, as shown by the zero DRC value. (Fig 4.11 a and c). As a whole this sensitivity analysis shows that the overall reaction rate cannot be attributed to a single elementary step as the rate controlling parameter varies with the electrode potentials.

4.3.4 Tafel Analysis

Tafel analysis was performed in a small overpotential range, -0 V to -0.4 V, to measure overall charge transfer coefficient. (Figure 4.11b) The Tafel equation for reduction current density can be written as follow:[107]

$$i = i_0 \exp\left(-\frac{\alpha n F \eta}{RT}\right) \qquad [30]$$

where, α is the charge transfer coefficient, n is the number of electrons involved in the reaction, η is the overpotential, i is the current density and i_0 is the exchange current density. Non-linear regression (goodness of fit, R^2=0.988) between current density (i) and electrode potential (V), reveals the charge transfer coefficient, $\alpha, = 0.24$, Tafel slope $=$ 248.9 $\pm$ 7.29 mV/dec and the exchange current density (i_0) = 0.226 ± 0.0214 mA/cm^2. (Figure 4.12) High Tafel slope can be explained by sluggish proton coupled electron transfer mechanism of COOH❋ and H❋ formation.

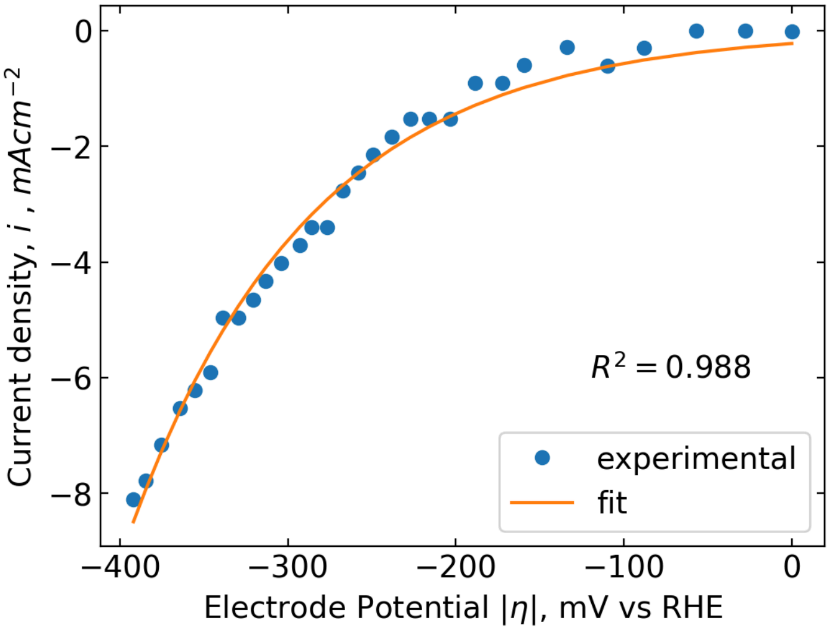

Figure 4.12 Tafel analysis. Plot of Current density as a function of overpotential in the Tafel region (0V to -0.4V)

We used the experimentally observed α value in our microkinetic model and calculated the current density. Figure 4.13a shows the experimental and simulated current densities at varying potential in the Tafel region. The shape of the simulated current density curve matches with the experimental curve which suggests that the effect of charge transfer coefficient is correctly incorporated in our model. Corresponding fractional coverages of the surface species at the varying potential is shown in Figure 4.13b. At all the electrode potentials, the surface coverage of COOH❋ is higher than the H❋ and dominates the surface coverage at the higher potential. Overall low surface coverage of the H❋ results into the lower current density of the hydrogen evolution reaction. The surface coverage distribution suggests the overall HER inhibition in the Tafel region.

We observed overall current is ~6 orders of magnitude lower than the experimentally observed current. This discrepancy in the magnitude of current density can be explained by the various reason. we considered only single type of active sites, M-N_4, for

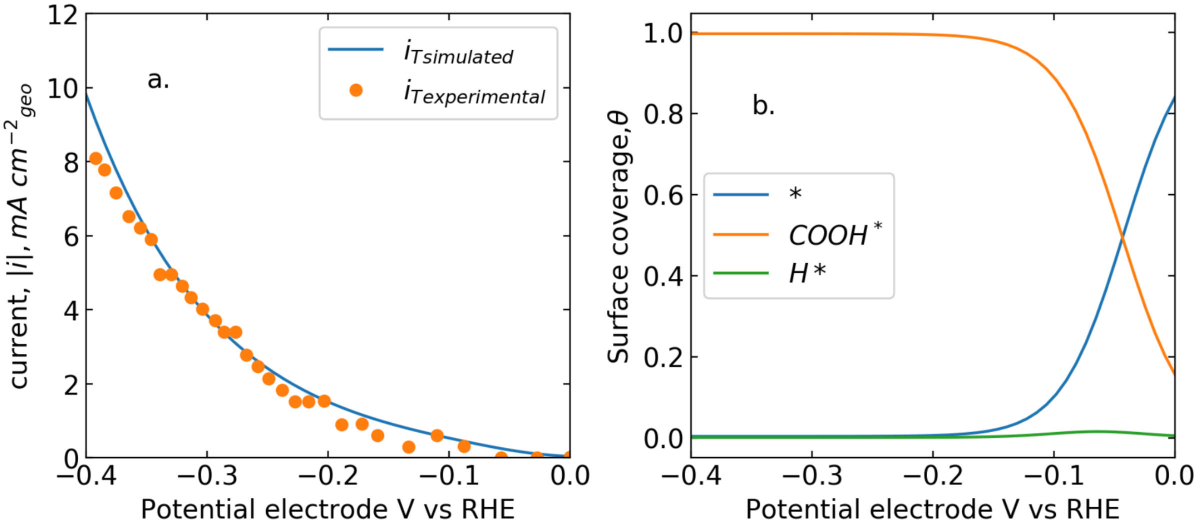

Figure 4.13 a) Comparison of simulated and experimentally measured total current densities ($\alpha = 0.24$).Simulated current is multiplied by the factor of 3 x10^6 b) Potential dependent fractional surface coverages of vacant ($*$) and adsorbed intermediate species ($COOH^*, H^*$).

CO_2RR and HER. MNC catalysts possess non-metal active sites such as Nx-Cy which might have different catalytic activities for the reaction cascades. In contrast, the experimentally observed overall charge transfer coefficient is the overall activity of active sites of all types present in the catalyst.

Lastly, the magnitude of pre-exponential factor (Eq. 15), is approximated to 10^{13} s^{-1} for all the elementary reaction in our model. The typical value of the pre-exponential factor for Eley-Rideal reactions is 10^3-10^1 Pa s^{-1}.[200] One way to estimate more precise value of the pre-exponential factor using transition state theory is to include the partition functions for surface mobility, vibrational, rotational and translational frequencies, surface entropies etc.[200] Alternatively, advanced molecular dynamics simulations with reactive forcefield (ReacFF) can also be used to simulate the reaction at different temperatures and then calculate the slope of ln(k) vs temperature (T) plot to estimate the pre-exponential factor.

4.4 Conclusions

We developed a microkinetic model for CO_2 reduction reaction on a single-atom metal-centered carbon-based catalyst. The influence of potential on the reaction rates and surface coverages has been explored in the study. We observed that at lower potential COOH adsorption dominates the catalytic surface and proton adsorption dominates at higher potential. The sensitivity analysis of the reaction mechanism provided insights about the rate controlling parameters in the system and helped reinforced the surface coverage distribution obtained from the simulation. Mass transport limitations of CO_2 and protons will affect the simulated results, and were not accounted for in our simulation. Metal-free ‘N’ atoms are possible active sites for CO_2RR and HER, and could be explored further to investigate the activity of non-metal center. This microkinetic model will provide direct mechanistic insights of the CO_2RR on M-N-C catalyst which can be used further to increase the faradaic efficiency by improving the catalytic surface and/or reaction conditions.

Chapter 5

Continuum Modeling study of a paper-based microreactor for a multi-step reaction cascade.

5.1 Introduction

For an efficient multi-step reaction cascade, architecture of an integrated catalytic platform is an important feature besides controlling intermediate transport and kinetics of the reaction cascade. Synthetic biology, molecular chemistry and advanced synthesis of combined organic and inorganic materials have investigated biological (enzymes), molecular (organocatalysts) and metallic catalysts, respectively. Each of these catalysts has enormous potential to improve the kinetics of the reaction. However, all of these different types of catalysts need different favorable reaction conditions. Thus, integration of the best catalysts for individual reaction steps, on one platform is very challenging.

A microfluidic channel provides a precise control over the fluid flow.[201,202] Materials like glass, silicon, PDMS and paper has been used to create microfluidic channels in microfluidic reactors.[203] Paper being cheap, flexible, biodegradable and easy to modify has been utilized widely to design a microfluidic device as a sensor. Thus, paper makes a very attractive option to design an integrated catalytic platform.

Our collaborators at University of New Mexico designed a paper-based integrated catalytic platform by immobilizing biological, molecular and metallic catalysts. Nalin et.al. carried out multistep oxidation of glycerol to carbon dioxide (CO_2) using a fan shaped micro-reactor, originally designed by Mendez et.al. [133,204,205] Figure 5.1 shows a schematic of a five-step reaction cascade consist of a molecular catalyst (4-amino-TEMPO), Biological catalyst (Oxalate Decarboxylase) and metallic catalyst (Pd/3D-GNS). Synthesis and characterization of the device is described in ref.[204]. A micro-reactor consists of the catalytic (reactive zone) and detection zone (non-reactive) to analyze the intermediate formation via Surface-enhanced Raman scattering (SERS) technique.

In this work, we studied kinetics and transport of the intermediates in the micro-reactor using a continuum modeling approach and quantify the intermediate formation. A one-dimensional geometry with reactive and non-reactive zones is simulated at different convective velocities to study the effect of transport in the microreactor. The concentration profile of each chemical species along the length of the microreactor is reported here.

5.2 Methods

A fan-shaped one-dimensional model consists of the main four zones, 1) a liquid inlet for introducing a substrate (glycerol), 2) catalytic reaction zones, 3) intermediate detection zones, and 4) a fan outlet. Velocity in such a fan-shaped paper is described by Mendez et. al.[205] and depends upon the fan shape. For the circular shaped fan, the velocity ranged between 0.015 cm/s -0.035 cm/s.[205] Reynold's number (Re) and Peclet number (Pe) of the system were calculated as :

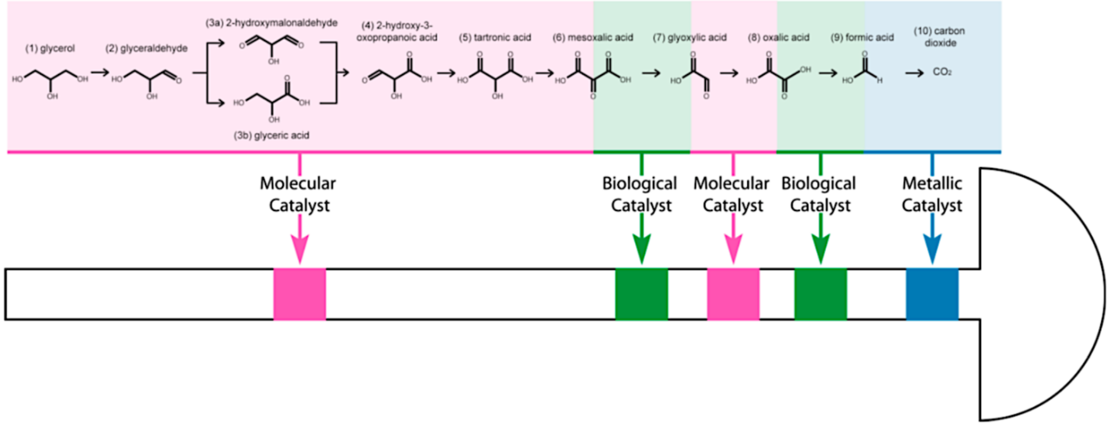

Figure 5.1 Glycerol oxidation reaction cascade on the fan-shaped micro-reactor. Pink, Green and Blue strips are catalyst layer respectively. (Device assembled by University of Irvin, California)[204]

Table 5.1: Simulation parameters

Parameters	**value**
Diffusion coefficient, $\boldsymbol{D}$/ cm2s -1	10-5
Velocity, $\boldsymbol{v}$ / cm s-1	0.01 -0.03
Initial Concentration, $\boldsymbol{C_i}$ / µM	1
Rate constant, $\boldsymbol{k_i}$ / s-1	0.1
Filter paper diameter, $\boldsymbol{d_p}$/ μm	2.5

$$Re = v \frac{d_p}{\nu} \quad [1]$$

$$Pe = Re\ Sc = Re\left(\frac{\nu}{D}\right) \quad [2]$$

where, $d_p$is a pore diameter of filter paper, v is velocity, ν is a dynamic viscosity of fluid and D is diffusivity of the system. There are all neutral species present in the reactor, therefore we considered diffusion and convection as the mode of transport. At steady state, assuming constant diffusivity and velocity, a mass balance equation on the intermediate is governed by the following equation:

$$-D_i \frac{d^2 C_i}{dx^2} - v \frac{dC_i}{dx} + R = 0 \quad [3]$$

where, D_i is the diffusivity, C_i is the concentration, R_i is the generation/consumption rate of intermediate species i and x is the position along the length of the reactor. The microreactor is fed with constant fuel having constant concentration at the inlet and the flux at the end of the device is assumed to be zero. We assumed a first order rate of reaction with constant rate constant at each catalytic layer. Simulation parameters are presented in Table 5.1.

5.3 Results and Discussion

We studied the effect of velocity on concentration profile of 6 chemical species and 5 catalytic reactions. Assuming average velocity of 0.02 cm/s and pore diameter of filter paper as 2.5 μm, the corresponding Reynolds number, Re, of the system was calculated to be 5x10^{-4} which is very low and termed as Stoke's flow. The corresponding Peclet number, Pe, is 0.5, confirming that diffusion cannot be neglected in the system and back-diffusion is a possibility. For an average velocity, concentration of each species in a non -reactive region is constant, confirming the absence of back-diffusion. However, in the absence of convection in the system, concentration gradient in both directions drives species to diffuse back as well as to the next catalytic layer. (Figure5.2-b)

Our model considered ideal mass transport and kinetic conditions which may not match with the true operating condition. Change in the atmospheric humidity will affect the

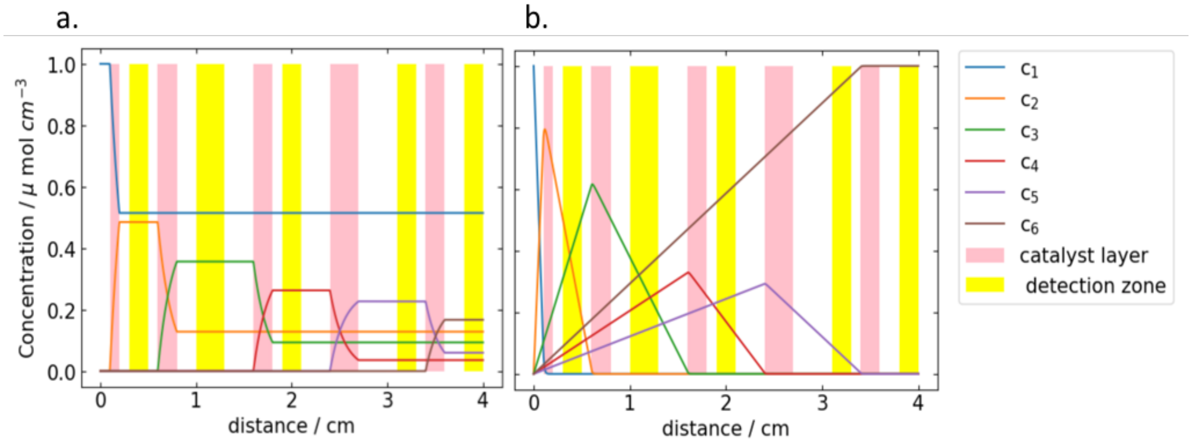

Figure 5.2 Concentration profile of all species in micro-reactor at a) Pe=0.5 b) Pe=0. Pink and yellow strips represent catalytic zone and detection zone respectively. Other parameters are in Table 5.1

evaporation rate that drives the convective transport in the microreactor, is not accounted for. Change in the catalytic activity due to immobilization of catalysts will affect the rate of the reaction in the system. deeper understanding of the reaction mechanism is necessary, when different types of the catalysts were paired on the single platform. Advanced modeling kinetic modeling techniques such as density functional theory, molecular dynamics with reactive force field (ReacFF) and kinetic Monte Carlo could be helpful to predict the reaction mechanism as well as reaction energies that will ultimately predict the catalytic activity of these platforms. An activity database of the different types of immobilized catalysts can be used to predict newer catalysts by using advanced data analysis such as machine learning. These kinetic parameters then can be used as an input for our model. Addition of the remaining spatial dimensions to the model will improve the accuracy of the model.

5.4 Conclusion

We studied the intermediate transport in the paper-based microreactor. Convective transport plays a very important role in the micro-reactor to prevent back-diffusion of the chemical species. For the reaction conditions, the location of the detection zone does not affect the quantitative assessment of product. This model provides a starting point to predict the quantification of intermediates. Experimental quantification of the intermediates at each detection zone of the micro-reactor is required to further validate the model.

Chapter 6

Summary and Future Work

Work presented in this thesis is solely motivated by the need for efficient multi-step reaction cascades to increase the selectivity and yield of the desired product by reducing capital and process costs of the product manufacturing. In order to design such an efficient system, we studied integrated catalytic platforms that can control kinetics and transport in the system and reduce the chemical losses. The substrate channeling mechanism of the multi-step reaction cascades in a biological system successfully controls the transport and kinetics in the system. Hence, we adopted features of these mechanisms in the study.

Chapter 2 focuses on the effect of confining the pathway of intermediates on the channeling efficiency. A geometry with two ring-shaped catalytic active sites within the open-ended cylindrical tunnel was simulated via a continuum modeling approach. In the confined system, a 2.5-fold increase in the product yield was observed over the non-confined system and proved the potential of efficient channeling via the confinement mechanism. We studied the effect of kinetics, transport, and geometrical parameters on the product yield and recommend a set of rules to design optimum geometry. In the kinetically limited region, maximum product yield can be achieved by the cylindrical geometry with 1) smaller tunnel diameter, 2) smaller distance between active sites, and 3) larger confined distance between the active site and the bulk. A conical configuration with a conical angle $\theta = 17.4^o$ is the optimum geometry for the mass transport limited region.

In Chapter 3, we studied the intermediate transport inside the tunnel at the molecular scale. The movement of intermediates, oxalate – negatively charged and non-polar, and ethanol- uncharged and polar, were studied inside the single-walled carbon nanotube via molecular dynamics. Molecular interaction between the tunnel wall and intermediate effectively decreased the diffusivity of the intermediate in the tunnel. The solvent orientation inside the tunnel also affects the intermediate transport. Maximum retention of the intermediate is the key to efficient channeling. Hence, we modified SWCNT termini with -1 charged carboxylate groups to retain intermediate inside the tunnel. The retention time of the intermediate increased with an increase in the terminal charge density and is very sensitive towards polarity instead of the change of the intermediate.

Overall, chapter 2 and 3 provides a comprehensive study of the effect of confinement of intermediate's pathway on the channeling efficiency. The nano-scaled tunnel has shown the potential of ~70% product yield and is a very attractive option to increase the selectivity of the product. In order to further pursue this strategy, experimental validation is required. With advanced nanoscale fabrication techniques, it may be possible to synthesize a tunnel with the catalytic rings within and validate our model.[120] A heterogeneous catalytic surface does not have a uniform active site density. Hence, a kinetic Monte Carlo (kMC)study of this system by considering a non-uniform surface will provide a better understanding of kinetics and transport together and bridge the gap between the continuum and the molecular model.

In chapter 4, we developed a microkinetic model for the mechanistic study of multi-step CO_2RR. In this work, kinetic parameters were estimated using density functional theory and the transition state was defined using nudged elastic band theory. In the absence of transport of chemical species, carboxylate, COOH*, dominates the surface coverage at low potential. However, HER dominates at the higher potential as activation energy barrier reduces exponentially. Distant metal active sites induce single site mechanism for CO_2RR and HER that includes proton coupled electron transfer. Due to such a complex electron transfer mechanism, we believe that charge transfer coefficient, surface concentration of chemical species, and interfacial water molecules will play very important role in the chemical transformation. And therefore, further ongoing investigation of these aspect is necessary to enhance the reaction mechanism understanding.

The addition of second active site with metal the metal active site of M-N-C will develop the CO_2RR cascade further to produce ethane. Successful synthesis of such a catalyst with two different types of active sites will be a major successful step towards the creation of integrated catalytic system for successful multi-step reaction cascades. This integrated catalytic platform will possess a surface diffusion mechanism for the successful transport of the intermediates between the active sites. The effect of additional surface phenomena on the overall reaction can be studied further with the advanced simulation techniques such as kinetic Monte Carlo (kMC) and reactive molecular dynamics.

Lastly, in Chapter 5, we modeled a paper-based microreactor designed for glycerol oxidation reaction cascade. Convective forces in such microreactor play an important role to transport chemical species in the forward direction, from one catalytic zone to another. Absence of convection in the system led to back-diffusion which reduces the product yield and selectivity. For the future work experimental quantification of the microreactor is utmost important to validate the model and understand the effect of transport and kinetics. Quantification of catalytic activity of each catalyst and the diffusivity of each species inside the filter paper will also increase the prediction accuracy of our model.

In this work, we studied intermediate transport mechanisms and reaction cascades to learn effective role of kinetics and transport on the overall multi-step reaction cascades.

This work is a ‘tip of the iceberg’ towards the understanding of efficient multi-step reaction cascades and acts as a primary guide to improve integrated catalytic platform designs.

BIBLIOGRAPHY

BIBILOGRAPHY

(1) Denard, C. A.; Hartwig, J. F.; Zhao, H. Multistep One-Pot Reactions Combining Biocatalysts and Chemical Catalysts for Asymmetric Synthesis. *ACS Catal.* **2013**, *3* (12), 2856–2864, doi:10.1021/cs400633a.

(2) Climent, M. J.; Corma, A.; Iborra, S.; Sabater, M. J. Heterogeneous Catalysis for Tandem Reactions. *ACS Catal.* **2014**, *4* (3), 870–891, doi:10.1021/cs401052k.

(3) Ambrosini, L. M.; Lambert, T. H. Multicatalysis: Advancing Synthetic Efficiency and Inspiring Discovery. *ChemCatChem* **2010**, *2* (11), 1373–1380, doi:10.1002/cctc.200900323.

(4) Zhang, L.; Sonaglia, L.; Stacey, J.; Lautens, M. Multicomponent Multicatalyst Reactions (MC)2R: One-Pot Synthesis of 3,4-Dihydroquinolinones. *Org. Lett.* **2013**, *15* (9), 2128–2131, doi:10.1021/ol4006008.

(5) Liebminger, S.; Siebenhofer, M.; Guebitz, G. Oxidation of Glycerol by 2,2,6,6-Tetramethylpiperidine-N-Oxyl (TEMPO) in the Presence of Laccase. *Bioresour. Technol.* **2009**, *100* (20), 4541–4545, doi:10.1016/j.biortech.2009.04.051.

(6) Falase, A.; Garcia, K.; Lau, C.; Atanassov, P. Electrochemical and in Situ IR Characterization of PtRu Catalysts for Complete Oxidation of Ethylene Glycol and Glycerol. *Electrochem. commun.* **2011**, *13* (12), 1488–1491, doi:10.1016/j.elecom.2011.10.001.

(7) Srere, P. a. Complexes Of Sequential Metabolic Enzymes. *Annu. Rev. Biochem.* **1987**, *56* (1), 89–124, doi:10.1146/annurev.biochem.56.1.89.

(8) Wheeldon, I.; Minteer, S. D.; Banta, S.; Barton, S. C.; Atanassov, P.; Sigman, M. Substrate Channelling as an Approach to Cascade Reactions. *Nat. Chem.* **2016**, *8* (4), 299–309, doi:10.1038/nchem.2459.

(9) Rickey Welch, G.; Easterby, J. S. Metabolic Channeling versus Free Diffusion: Transition-Time Analysis. *Trends Biochem. Sci.* **1994**, *19* (5), 193–197, doi:10.1016/0968-0004(94)90019-1.

(10) Cheng, Y.; Chang, C.-E. a; Yu, Z.; Zhang, Y.; Sun, M.; Leyh, T. S.; Holst, M. J.; McCammon, J. A. Diffusional Channeling in the Sulfate-Activating Complex: Combined Continuum Modeling and Coarse-Grained Brownian Dynamics Studies. *Biophys. J.* **2008**, *95* (10), 4659–4667, doi:10.1529/biophysj.108.140038.

(11) Huang, X.; Holden, H. M.; Raushel, F. M. Channeling of Substrates and Intermediates in Enzyme-Catalyzed Reactions. *Annu. Rev. Biochem.* **2001**, *70* (1), 149–180,

doi:10.1146/annurev.biochem.70.1.149.

(12) Miles, E. W.; Rhee, S.; Davies, D. R. The Molecular Basis of Substrate Channeling. *Journal of Biological Chemistry*. 1999, pp 12193–12196, doi:10.1074/jbc.274.18.12193.

(13) Loutchko, D.; Gonze, D.; Mikhailov, A. S. Single-Molecule Stochastic Analysis of Channeling Enzyme Tryptophan Synthase. *J. Phys. Chem. B* **2016**, *120* (9), 2179–2186, doi:10.1021/acs.jpcb.5b12229.

(14) Dunn, M. F.; Niks, D.; Ngo, H.; Barends, T. R. M.; Schlichting, I. Tryptophan Synthase: The Workings of a Channeling Nanomachine. *Trends Biochem. Sci.* **2008**, *33* (6), 254–264, doi:10.1016/j.tibs.2008.04.008.

(15) Thoden, J. B.; Holden, H. M.; Wesenberg, G.; Raushel, F. M.; Rayment, I. Structure of Carbamoyl Phosphate Synthetase: A Journey of 96 ?? From Substrate to Product. *Biochemistry* **1997**, *36* (97), 6305–6316, doi:10.1021/bi970503q.

(16) Smolle, M.; Prior, A. E.; Brown, A. E.; Cooper, A.; Byron, O.; Lindsay, J. G. A New Level of Architectural Complexity in the Human Pyruvate Dehydrogenase Complex. *J. Biol. Chem.* **2006**, *281* (28), 19772–19780, doi:10.1074/jbc.M601140200.

(17) Castellana, M.; Wilson, M. Z.; Xu, Y.; Joshi, P.; Cristea, I. M.; Rabinowitz, J. D.; Gitai, Z.; Wingreen, N. S. Enzyme Clustering Accelerates Processing of Intermediates through Metabolic Channeling. *Nat. Biotechnol.* **2014**, *32* (10), 1011–1018, doi:10.1038/nbt.3018.

(18) Ishikawa, M.; Tsuchiya, D.; Oyama, T.; Tsunaka, Y.; Morikawa, K. Structural Basis for Channelling Mechanism of a Fatty Acid β-Oxidation Multienzyme Complex. *EMBO J.* **2004**, *23* (14), 2745–2754, doi:10.1038/sj.emboj.7600298.

(19) Knighton, D. R.; Kan, C. C.; Howland, E.; Janson, C. A.; Hostomska, Z.; Welsh, K. M.; Matthews, D. A. Structure of and Kinetic Channelling in Bifunctional Dihydrofolate Reductase-Thymidylate Synthase. *Nat. Struct. Biol.* **1994**, *1*, 186–194, doi:10.1038/nsb0394-186.

(20) Earl, E.; Calabrese Barton, S. Simulation of Intermediate Transport in Nanoscale Scaffolds for Multistep Catalytic Reactions. *Phys. Chem. Chem. Phys.* **2017**, *19* (23), 1–8, doi:10.1039/C7CP00239D.

(21) Liu, Y.; Matanovic, I.; Hickey, D. P.; Minteer, S. D.; Atanassov, P.; Barton, S. C. Cascade Kinetics of an Artificial Metabolon by Molecular Dynamics and Kinetic Monte Carlo. *ACS Catal.* **2018**, *8* (8), 7719–7726, doi:10.1021/acscatal.8b01041.

(22) Eun, C.; Kekenes-Huskey, P. M.; McCammon, J. A. Influence of Neighboring Reactive Particles on Diffusion-Limited Reactions. *J. Chem. Phys.* **2013**, *139* (4), 044117, doi:10.1063/1.4816522.

(23) Hyde, C. C.; Ahmed, S. a; Padlan, E. a; Miles, E. W.; Davies, D. R. Three-Dimensional Structure of the Tryptophan Synthase Alpha 2 Beta 2 Multienzyme Complex from Salmonella Typhimurium. *J. Biol. Chem.* **1988**, *263* (33), 17857–17871.

(24) Huang, X.; Holden, H. M.; Raushel, F. M. Channeling of Substrates and Intermediates in Enzyme-Catalyzed Reactions. *Annu. Rev. Biochem.* **2001**, *70*, 149–180, doi:10.1146/annurev.biochem.70.1.149.

(25) Carere, J.; McKenna, S. E.; Kimber, M. S.; Seah, S. Y. K. Characterization of an Aldolase-Dehydrogenase Complex from the Cholesterol Degradation Pathway of Mycobacterium Tuberculosis. *Biochemistry* **2013**, *52* (20), 3502–3511, doi:10.1021/bi400351h.

(26) Carere, J.; Baker, P.; Seah, S. Y. K. Investigating the Molecular Determinants for Substrate Channeling in BphI-BphJ, an Aldolase-Dehydrogenase Complex from the Polychlorinated Biphenyls Degradation Pathway. *Biochemistry* **2011**, *50* (39), 8407–8416, doi:10.1021/bi200960j.

(27) Elcock, A. H.; Huber, G. A.; Andrew McCammon, J. Electrostatic Channeling of Substrates between Enzyme Active Sites: Comparison of Simulation and Experiment. *Biochemistry* **1997**, *36* (97), 16049–16058, doi:10.1021/bi971709u.

(28) Elcock, a H.; Potter, M. J.; Matthews, D. a; Knighton, D. R.; McCammon, J. a. Electrostatic Channeling in the Bifunctional Enzyme Dihydrofolate Reductase-Thymidylate Synthase. *J. Mol. Biol.* **1996**, *262* (3), 370–374, doi:10.1006/jmbi.1996.0520.

(29) Elcock, A. H.; Andrew McCammon, J. Evidence for Electrostatic Channeling in a Fusion Protein of Malate Dehydrogenase and Citrate Synthase. *Biochemistry* **1996**, *35* (96), 12652–12658, doi:10.1021/bi9614747.

(30) Jørgensen, K.; Rasmussen, A. V.; Morant, M.; Nielsen, A. H.; Bjarnholt, N.; Zagrobelny, M.; Bak, S.; Møller, B. L. Metabolon Formation and Metabolic Channeling in the Biosynthesis of Plant Natural Products. *Curr. Opin. Plant Biol.* **2005**, *8* (3 SPEC. ISS.), 280–291, doi:10.1016/j.pbi.2005.03.014.

(31) Smolle, M.; Lindsay, J. G. Molecular Architecture of the Pyruvate Dehydrogenase Complex: Bridging the Gap. *Biochem. Soc. Trans.* **2006**, *34* (5), 815–818, doi:10.1042/BST0340815.

(32) An, S.; Kumar, R.; Sheets, E. D.; Benkovic, S. J. Reversible Compartmentalization of de Novo Purine Biosynthetic Complexes in Living Cells. *Science* **2008**, *320* (5872), 103–

106, doi:10.1126/science.1152241.

(33) Yamada, Y.; Tsung, C.-K.; Huang, W.; Huo, Z.; Habas, S. E.; Soejima, T.; Aliaga, C. E.; Somorjai, G. a; Yang, P. Nanocrystal Bilayer for Tandem Catalysis. *Nat. Chem.* **2011**, *3* (April), 372–376, doi:10.1038/nchem.1018.

(34) Lee, H.; DeLoache, W. C.; Dueber, J. E. Spatial Organization of Enzymes for Metabolic Engineering. *Metab. Eng.* **2012**, *14* (3), 242–251, doi:10.1016/j.ymben.2011.09.003.

(35) Vriezema, D. M.; Garcia, P. M. L.; Sancho Oltra, N.; Hatzakis, N. S.; Kuiper, S. M.; Nolte, R. J. M.; Rowan, A. E.; Van Hest, J. C. M. Positional Assembly of Enzymes in Polymersome Nanoreactors for Cascade Reactions. *Angew. Chemie - Int. Ed.* **2007**, *46* (39), 7378–7382, doi:10.1002/anie.200701125.

(36) Fu, J.; Liu, M.; Liu, Y.; Woodbury, N. W.; Yan, H. Interenzyme Substrate Diffusion for an Enzyme Cascade Organized on Spatially Addressable DNA Nanostructures. *J. Am. Chem. Soc.* **2012**, *134* (12), 5516–5519, doi:10.1021/ja300897h.

(37) Fu, Y.; Zeng, D.; Chao, J.; Jin, Y.; Zhang, Z.; Liu, H.; Li, D.; Ma, H.; Huang, Q.; Gothelf, K. V.; et al. Single-Step Rapid Assembly of DNA Origami Nanostructures for Addressable Nanoscale Bioreactors. *J. Am. Chem. Soc.* **2013**, *135* (2), 696–702, doi:10.1021/ja3076692.

(38) Fu, J.; Yang, Y. R.; Johnson-Buck, A.; Liu, M.; Liu, Y.; Walter, N. G.; Woodbury, N. W.; Yan, H. Multi-Enzyme Complexes on DNA Scaffolds Capable of Substrate Channelling with an Artificial Swinging Arm. *Nat. Nanotechnol.* **2014**, *9* (May), 1–6, doi:10.1038/nnano.2014.100.

(39) Lindbladh, C.; Rault, M.; Hagglund, C.; Small, W. C.; Mosbach, K.; Bülow, L.; Evans, C.; Srere, P. A. Preparation and Kinetic Characterization of a Fusion Protein of Yeast Mitochondrial Citrate Synthase and Malate Dehydrogenase. *Biochemistry* **1994**, *33*, 11692–11698, doi:10.1021/bi00205a004.

(40) Zhang, Y.; Tsitkov, S.; Hess, H. Proximity Does Not Contribute to Activity Enhancement in the Glucose Oxidase-Horseradish Peroxidase Cascade. *Nat. Commun.* **2016**, *7*, 13982, doi:10.1038/ncomms13982.

(41) You, C.; Myung, S.; Zhang, Y. H. P. Facilitated Substrate Channeling in a Self-Assembled Trifunctional Enzyme Complex. *Angew. Chemie - Int. Ed.* **2012**, *51* (35), 8787–8790, doi:10.1002/anie.201202441.

(42) Van Dongen, S. F. M.; Nallani, M.; Cornelissen, J. J. L. M.; Nolte, R. J. M.; Van Hest, J. C. M. A Three-Enzyme Cascade Reaction through Positional Assembly of Enzymes in a Polymersome Nanoreactor. *Chem. - A Eur. J.* **2009**, *15*, 1107–1114, doi:10.1002/chem.200802114.

(43) Vriezema, D. M.; Comellas Aragonès, M.; Elemans, J. A. A. W.; Cornelissen, J. J. L. M.; Rowan, A. E.; Nolte, R. J. M. Self-Assembled Nanoreactors. *Chem. Rev.* **2005**, *105* (4), 1445–1490, doi:10.1021/cr0300688.

(44) Zhao, M.; Deng, K.; He, L.; Liu, Y.; Li, G.; Zhao, H.; Tang, Z. Core–Shell Palladium Nanoparticle@Metal–Organic Frameworks as Multifunctional Catalysts for Cascade Reactions. *J. Am. Chem. Soc.* **2014**, *136* (5), 1738–1741, doi:10.1021/ja411468e.

(45) Li, P.; Cao, C.-Y.; Chen, Z.; Liu, H.; Yu, Y.; Song, W.-G. Core–Shell Structured Mesoporous Silica as Acid–Base Bifunctional Catalyst with Designated Diffusion Path for Cascade Reaction Sequences. *Chem. Commun.* **2012**, *48*, 10541, doi:10.1039/c2cc35718f.

(46) Yan, J.; Rao, G. V. R.; Barela, M.; Brevnov, D. A.; Jiang, Y.; Xu, H.; López, G. P.; Atanassov, P. B. Growth of Patterned Nanopore Arrays of Anodic Aluminum Oxide. *Adv. Mater.* **2003**, *15* (23), 2015–2018, doi:10.1002/adma.200305360.

(47) Stan, M.; Ramirez, J. C.; Cristea, P.; Hu, S. Y.; Deo, C.; Uberuaga, B. P.; Srivilliputhur, S.; Rudin, S. P.; Wills, J. M. Models and Simulations of Nuclear Fuel Materials Properties. *J. Alloys Compd.* **2007**, *444–445* (SPEC. ISS.), 415–423, doi:10.1016/j.jallcom.2007.01.102.

(48) Plawsky, J. L. *Transport Phenomena Fundamentals*, Third.; 2013.

(49) Raimondeau, S.; Vlachos, D. G. Recent Developments on Multiscale, Hierarchical Modeling of Chemical Reactors. *Chem. Eng. J.* **2002**, *90* (1–2), 3–23, doi:10.1016/S1385-8947(02)00065-7.

(50) Li, G.; Zhang, C.; Xing, X.-H. H. A Kinetic Model for Analysis of Physical Tunnels in Sequentially Acting Enzymes with Direct Proximity Channeling. *Biochem. Eng. J.* **2016**, *105*, 242–248, doi:10.1016/j.bej.2015.09.020.

(51) Okabe, Y. On the Theory of Brownian Motion with the Alder-Wainwright Effect. *J. Stat. Phys.* **1986**, *45* (5–6), 953–981, doi:10.1007/BF01020584.

(52) Chen, J. C.; Kim, A. S. Brownian Dynamics , Molecular Dynamics , and Monte Carlo Modeling of Colloidal Systems. **2004**, *112*, 159–173, doi:10.1016/j.cis.2004.10.001.

(53) Bauler, P.; Huber, G.; Leyh, T.; McCammon, J. A. Channeling by Proximity: The Catalytic Advantages of Active Site Colocalization Using Brownian Dynamics. *J. Phys. Chem. Lett.* **2010**, *1* (9), 1332–1335, doi:10.1021/jz1002007.

(54) Kuzmak, A.; Carmali, S.; von Lieres, E.; Russell, A. J.; Kondrat, S. Can Enzyme Proximity Accelerate Cascade Reactions? *Sci. Rep.* **2019**, *9* (1), 1–8, doi:10.1038/s41598-018-37034-3.

(55) Lin, J. L.; Wheeldon, I. Kinetic Enhancements in DNA-Enzyme Nanostructures Mimic the Sabatier Principle. *ACS Catal.* **2013**, *3* (4), 560–564, doi:10.1021/cs300766d.

(56) Liu, Y.; Hickey, D. P.; Guo, J.-Y.; Earl, E.; Abdellaoui, S.; Milton, R. D.; Sigman, M. S.; Minteer, S. D.; Calabrese Barton, S. Substrate Channeling in an Artificial Metabolon: A Molecular Dynamics Blueprint for an Experimental Peptide Bridge. *ACS Catal.* **2017**, *7* (4), 2486–2493, doi:10.1021/acscatal.6b03440.

(57) Letcher, T. M. *Why Do We Have Global Warming?*; Elsevier Inc., 2019, doi:10.1016/b978-0-12-814104-5.00001-6.

(58) Vinet, L.; Zhedanov, A. A “Missing” Family of Classical Orthogonal Polynomials. *J. Neurosci. Methods* **2010**, *176* (2), 57–62, doi:10.1088/1751-8113/44/8/085201.

(59) Azuma, M.; Watanabe, M. Electrodes in Low-Temperature Aqueous KHC03 Media. *J. Electrochem. Soc.* **1990**, *137* (6), 1772–1778.

(60) Benson, E. E.; Kubiak, C. P.; Sathrum, A. J.; Smieja, J. M. Electrocatalytic and Homogeneous Approaches to Conversion of CO 2 to Liquid Fuels. *Chem. Soc. Rev.* **2009**, *38* (1), 89–99, doi:10.1039/B804323J.

(61) DeWulf, D. W.; Jin, T.; Bard, A. J. Electrochemical and Surface Studies of Carbon Dioxide Reduction to Methane and Ethylene at Copper Electrodes in Aqueous Solutions. *J. Electrochem. Soc.* **1989**, *136* (6), 1686, doi:10.1149/1.2096993.

(62) Qiao, J.; Liu, Y.; Hong, F.; Zhang, J. A Review of Catalysts for the Electroreduction of Carbon Dioxide to Produce Low-Carbon Fuels. *Chemical Society Reviews*. Royal Society of Chemistry December 16, 2014, pp 631–675, doi:10.1039/c3cs60323g.

(63) Hori, Y. Enhanced Evolution of CO and Supressed Formation of HCs in ERC at Cu Electrode Modified with Cd.Pdf. 1990.

(64) Padilla, M.; Baturina, O.; Gordon, J. P.; Artyushkova, K.; Atanassov, P.; Serov, A. Selective CO2 Electroreduction to C2H4 on Porous Cu Films Synthesized by Sacrificial Support Method. *J. CO2 Util.* **2017**, *19*, 137–145, doi:10.1016/j.jcou.2017.03.006.

(65) Cui, C.; Wang, H.; Zhu, X.; Han, J.; Ge, Q. A DFT Study of CO2 Electrochemical Reduction on Pb(211) and Sn(112). *Sci. China Chem.* **2015**, *58* (4), 607–613, doi:10.1007/s11426-015-5323-z.

(66) Baruch, M. F.; Pander, J. E.; White, J. L.; Bocarsly, A. B. Mechanistic Insights into the Reduction of CO2 on Tin Electrodes Using in Situ ATR-IR Spectroscopy. *ACS Catal.* **2015**, *5* (5), 3148–3156, doi:10.1021/acscatal.5b00402.

(67) Gunathunge, C. M.; Li, X.; Li, J.; Hicks, R. P.; Ovalle, V. J.; Waegele, M. M. Spectroscopic Observation of Reversible Surface Reconstruction of Copper Electrodes under CO2

Reduction. *J. Phys. Chem. C* **2017**, *121* (22), 12337–12344, doi:10.1021/acs.jpcc.7b03910.

(68) Wuttig, A.; Liu, C.; Peng, Q.; Yaguchi, M.; Hendon, C. H.; Motobayashi, K.; Ye, S.; Osawa, M.; Surendranath, Y. Tracking a Common Surface-Bound Intermediate during CO2-to- Fuels Catalysis. *ACS Cent. Sci.* **2016**, *2* (8), 522–528, doi:10.1021/acscentsci.6b00155.

(69) Chen, Y.; Kanan, M. W. Tin Oxide Dependence of the CO 2 Reduction Efficiency on Tin Electrodes and Enhanced Activity for Tin/Tin Oxide Thin-Film Catalysts. *J. Am. Chem. Soc.* **2012**, *134* (4), 1986–1989, doi:10.1021/ja2108799.

(70) Mistry, H.; Reske, R.; Zeng, Z.; Zhao, Z. J.; Greeley, J.; Strasser, P.; Cuenya, B. R. Exceptional Size-Dependent Activity Enhancement in the Electroreduction of CO2 over Au Nanoparticles. *J. Am. Chem. Soc.* **2014**, *136* (47), 16473–16476, doi:10.1021/ja508879j.

(71) Ma, M.; Trześniewski, B. J.; Xie, J.; Smith, W. A. Selective and Efficient Reduction of Carbon Dioxide to Carbon Monoxide on Oxide-Derived Nanostructured Silver Electrocatalysts. *Angew. Chemie* **2016**, *128* (33), 9900–9904, doi:10.1002/ange.201604654.

(72) Mistry, H.; Choi, Y. W.; Bagger, A.; Scholten, F.; Bonifacio, C. S.; Sinev, I.; Divins, N. J.; Zegkinoglou, I.; Jeon, H. S.; Kisslinger, K.; et al. Enhanced Carbon Dioxide Electroreduction to Carbon Monoxide over Defect-Rich Plasma-Activated Silver Catalysts. *Angew. Chemie - Int. Ed.* **2017**, *56* (38), 11394–11398, doi:10.1002/anie.201704613.

(73) Lu, Q.; Rosen, J.; Jiao, F. Nanostructured Metallic Electrocatalysts for Carbon Dioxide Reduction. *ChemCatChem* **2015**, *7* (1), 38–47, doi:10.1002/cctc.201402669.

(74) Asset, T.; Garcia, S. T.; Herrera, S.; Andersen, N.; Chen, Y.; Peterson, E. J.; Matanovic, I.; Artyushkova, K.; Lee, J.; Minteer, S. D.; et al. Investigating the Nature of the Active Sites for the CO 2 Reduction Reaction on Carbon-Based Electrocatalysts. *ACS Catal.* **2019**, *9* (9), 7668–7678, doi:10.1021/acscatal.9b01513.

(75) Varela, A. S.; Ranjbar Sahraie, N.; Steinberg, J.; Ju, W.; Oh, H. S.; Strasser, P. Metal-Doped Nitrogenated Carbon as an Efficient Catalyst for Direct CO<inf>2</Inf> Electroreduction to CO and Hydrocarbons. *Angew. Chemie - Int. Ed.* **2015**, *54* (37), 10758–10762, doi:10.1002/anie.201502099.

(76) Jiang, K.; Siahrostami, S.; Zheng, T.; Hu, Y.; Hwang, S.; Stavitski, E.; Peng, Y.; Dynes, J.; Gangisetty, M.; Su, D.; et al. Isolated Ni Single Atoms in Graphene Nanosheets for High-Performance CO2 Reduction. *Energy Environ. Sci.* **2018**, *11* (4), 893–903, doi:10.1039/c7ee03245e.

(77) Huan, T. N.; Ranjbar, N.; Rousse, G.; Sougrati, M.; Zitolo, A.; Mougel, V.; Jaouen, F.; Fontecave, M. Electrochemical Reduction of CO 2 Catalyzed by Fe-N-C Materials: A Structure–Selectivity Study. *ACS Catal.* **2017**, *7* (3), 1520–1525, doi:10.1021/acscatal.6b03353.

(78) Möller, T.; Ju, W.; Bagger, A.; Wang, X.; Luo, F.; Ngo Thanh, T.; Varela, A. S.; Rossmeisl, J.; Strasser, P. Efficient CO 2 to CO Electrolysis on Solid Ni–N–C Catalysts at Industrial Current Densities. *Energy Environ. Sci.* **2019**, *12* (2), 640–647, doi:10.1039/C8EE02662A.

(79) Delafontaine, L.; Asset, T.; Atanassov, P. Metal-Nitrogen-Carbon Electrocatalysts for CO2 Reduction Towards Syngas Generation. *ChemSusChem* **2020**, cssc.201903281, doi:10.1002/cssc.201903281.

(80) Varela, A. S.; Ju, W.; Bagger, A.; Franco, P.; Rossmeisl, J.; Strasser, P. Electrochemical Reduction of CO 2 on Metal-Nitrogen-Doped Carbon Catalysts. *ACS Catal.* **2019**, *9* (8), 7270–7284, doi:10.1021/acscatal.9b01405.

(81) Ma, M.; Grey, F.; Shen, L.; Urbakh, M.; Wu, S.; Liu, J. Z.; Liu, Y.; Zheng, Q. Water Transport inside Carbon Nanotubes Mediated by Phonon-Induced Oscillating Friction. *Nat. Nanotechnol.* **2015**, *10* (July), 1–5, doi:10.1038/nnano.2015.134.

(82) Ju, W.; Bagger, A.; Hao, G. P.; Varela, A. S.; Sinev, I.; Bon, V.; Roldan Cuenya, B.; Kaskel, S.; Rossmeisl, J.; Strasser, P. Understanding Activity and Selectivity of Metal-Nitrogen-Doped Carbon Catalysts for Electrochemical Reduction of CO2. *Nat. Commun.* **2017**, *8* (1), 944, doi:10.1038/s41467-017-01035-z.

(83) Bagger, A.; Ju, W.; Varela, A. S.; Strasser, P.; Rossmeisl, J. Electrochemical CO2 Reduction: A Classification Problem. *ChemPhysChem* **2017**, *18* (22), 3266–3273, doi:10.1002/cphc.201700736.

(84) Wang, T.; Zhao, Q.; Fu, Y.; Lei, C.; Yang, B.; Li, Z.; Lei, L.; Wu, G.; Hou, Y. Carbon-Rich Nonprecious Metal Single Atom Electrocatalysts for CO2 Reduction and Hydrogen Evolution. *Small Methods* **2019**, *3* (10), 1–17, doi:10.1002/smtd.201900210.

(85) Cui, H.; Guo, Y.; Guo, L.; Wang, L.; Zhou, Z.; Peng, Z. Heteroatom-Doped Carbon Materials and Their Composites as Electrocatalysts for CO2 Reduction. *J. Mater. Chem. A* **2018**, *6* (39), 18782–18793, doi:10.1039/c8ta07430e.

(86) Pan, F.; Deng, W.; Justiniano, C.; Li, Y. Identification of Champion Transition Metals Centers in Metal and Nitrogen-Codoped Carbon Catalysts for CO2 Reduction. *Appl. Catal. B Environ.* **2018**, *226* (November 2017), 463–472, doi:10.1016/j.apcatb.2018.01.001.

(87) Kothandaraman, R.; Nallathambi, V.; Artyushkova, K.; Calabrese Barton, S. Non-Precious Oxygen Reduction Catalysts Prepared by High-Pressure Pyrolysis for Low-

Temperature Fuel Cells. *Appl. Catal. B Environ.* **2009**, *92* (2), 209–216, doi:10.1016/j.apcatb.2009.07.005.

(88) Santoro, C.; Serov, A.; Stariha, L.; Kodali, M.; Gordon, J.; Babanova, S.; Bretschger, O.; Artyushkova, K.; Atanassov, P. Iron Based Catalysts from Novel Low-Cost Organic Precursors for Enhanced Oxygen Reduction Reaction in Neutral Media Microbial Fuel Cells. *Energy Environ. Sci. Energy Environ. Sci* **2346**, *9* (9), 2346–2353, doi:10.1039/c6ee01145d.

(89) Chen, R.; Yan, J.; Liu, Y.; Li, J. Three-Dimensional Nitrogen-Doped Graphene/MnO Nanoparticle Hybrids as a High-Performance Catalyst for Oxygen Reduction Reaction. *J. Phys. Chem. C* **2015**, *119* (15), 8032–8037, doi:10.1021/acs.jpcc.5b00306.

(90) Rasmussen, S. C.; Richter, M. M.; Yi, E.; Place, H.; Brewer, K. J. Synthesis and Characterization of a Series of Novel Rhodium and Iridium Complexes Containing Polypyridyl Bridging Ligands: Potential Uses in the Development of Multimetal Catalysts for Carbon Dioxide Reduction. *Inorg. Chem.* **1990**, *29* (20), 3926–3932, doi:10.1021/ic00345a005.

(91) Thompson, S. J.; Brennan, M. R.; Lee, S. Y.; Dong, G. Synthesis and Applications of Rhodium Porphyrin Complexes. *Chem. Soc. Rev.* **2018**, *47* (3), 929–981, doi:10.1039/c7cs00582b.

(92) Zheng, L.; Ye, D.; Xiong, L.; Xu, J.; Tao, K.; Zou, Z.; Huang, D.; Kang, X.; Yang, S.; Xia, J. Preparation of Cobalt-Tetraphenylporphyrin/Reduced Graphene Oxide Nanocomposite and Its Application on Hydrogen Peroxide Biosensor. *Anal. Chim. Acta* **2013**, *768* (1), 69–75, doi:10.1016/j.aca.2013.01.019.

(93) Lennox, J. C.; Murray, R. W. Chemically Modified Electrodes Vi. Binding and Reversible Electrochemistry of Tetra- (Aminophenyl)Porphyrin on Glassy Carbon. *J. Electroanal. Chem.* **1977**, *78*, 395–401.

(94) Singh, M. R.; Goodpaster, J. D.; Weber, A. Z.; Head-Gordon, M.; Bell, A. T. Mechanistic Insights into Electrochemical Reduction of CO2 over Ag Using Density Functional Theory and Transport Models. *Proc. Natl. Acad. Sci. U. S. A.* **2017**, *114* (42), E8812–E8821, doi:10.1073/pnas.1713164114.

(95) Nørskov, J. K.; Studt, F.; Abild-Pedersen, F.; Bligaard, T. *Fundamental Concepts in Heterogeneous Catalysis*; wiley, 2014; Vol. 9781118888, doi:10.1002/9781118892114.

(96) Salciccioli, M.; Stamatakis, M.; Caratzoulas, S.; Vlachos, D. G. A Review of Multiscale Modeling of Metal-Catalyzed Reactions: Mechanism Development for Complexity and Emergent Behavior. *Chem. Eng. Sci.* **2011**, *66* (19), 4319–4355, doi:10.1016/j.ces.2011.05.050.

(97) Dumesic, J. A.; Milligan, B. A.; Greppi, L. A.; Balse, V. R.; Sarnowski, K. T.; Beall, C. E.; Kataoka, T.; Rudd, D. F.; Trevino, A. A. A Kinetic Modeling Approach to the Design of Catalysts: Formulation of a Catalyst Design Advisory Program. *Ind. Eng. Chem. Res.* **1987**, *26* (7), 1399–1407, doi:10.1021/ie00067a022.
(98) Laidler ', K. J.; Klng, M. C. The Development of Transition-State Theory. *J. Phys. Chem* **1983**, *87*, 2657–2664.

(99) Agmon, N.; Levine, R. D. Structural Considerations in Chemical Kinetics: Gas Phase H-Atom Transfer Reaction Series. *Isr. J. Chem.* **1980**, *19* (1–4), 330–336, doi:10.1002/ijch.198000041.

(100) Cramer, christopher J. *Essentials of Computational Chemistry, Theories and Models*, 2nd ed.; wiley, 2002.

(101) Scholl, David S., Steckel, J. A. *Theory Density Functional Theory - A Practical Introduction*; 2009, doi:10.1007/978-3-642-20180-6_7.

(102) Schrödinger, E. An Undulatory Theory of the Mechanics of Atoms and Molecules. *Phys. Rev.* **1926**, *28* (6), 1049–1070, doi:10.1103/PhysRev.28.1049.
(103) Hohenberg, P.; Kohn, W. Inhomogeneous Electron Gas. *Phys. Rev.* **1964**, *136* (3B), B864–B871, doi:10.1103/PhysRev.136.B864.

(104) Kohn, W.; Sham, L. J. Self-Consistent Equations Including Exchange and Correlation Effects. *Phys. Rev.* **1965**, *140* (4A), A1133–A1138, doi:10.1103/PhysRev.140.A1133.

(105) Schagger, H.; Cramer, W. A.; Vonjagow, G. Expression of Terminal Oxidases under Nutrient-Starved Conditions in *Shewanella Oneidensis*: Detection of the A-Type Cytochrome c Oxidase. *Anal. Biochem.* **1994**, *217* (2), 220–230, doi:10.1038/srep19726.

(106) Liu, X.; Schlexer, P.; Xiao, J.; Ji, Y.; Wang, L.; Sandberg, R. B.; Tang, M.; Brown, K. S.; Peng, H.; Ringe, S.; et al. PH Effects on the Electrochemical Reduction of CO (2) towards C 2 Products on Stepped Copper. *Nat. Commun.* **2019**, *10* (1), 32, doi:10.1038/s41467-018-07970-9.

(107) Shinagawa, T.; Garcia-Esparza, A. T.; Takanabe, K. Insight on Tafel Slopes from a Microkinetic Analysis of Aqueous Electrocatalysis for Energy Conversion. *Sci. Rep.* **2015**, *5* (May), 1–21, doi:10.1038/srep13801.

(108) Zijlstra, B.; Zhang, X.; Liu, J.-X.; Filot, I. A. W.; Zhou, Z.; Sun, S.; Hensen, E. J. M. First-Principles Microkinetics Simulations of Electrochemical Reduction of CO2 over Cu Catalysts. *Electrochim. Acta* **2020**, *335*, 135665, doi:10.1016/j.electacta.2020.135665.

(109) Goodpaster, J. D.; Bell, A. T.; Head-Gordon, M. Identification of Possible Pathways for C-C Bond Formation during Electrochemical Reduction of CO2: New Theoretical

Insights from an Improved Electrochemical Model. *J. Phys. Chem. Lett.* **2016**, *7* (8), 1471–1477, doi:10.1021/acs.jpclett.6b00358.

(110) Chen, L. D.; Urushihara, M.; Chan, K.; Nørskov, J. K. Electric Field Effects in Electrochemical CO2 Reduction. *ACS Catal.* **2016**, *6* (10), 7133–7139, doi:10.1021/acscatal.6b02299.

(111) Ngo, H.; Harris, R.; Kimmich, N.; Casino, P.; Niks, D.; Blumenstein, L.; Barends, T. R.; Kulik, V.; Weyand, M.; Schlichting, I.; et al. Synthesis and Characterization of Allosteric Probes of Substrate Channeling in the Tryptophan Synthase Bienzyme Complex. *Biochemistry* **2007**, *46* (26), 7713–7727, doi:10.1021/bi700385f.

(112) Anderson, K. S.; Miles, E. W.; Johnson, K. A. Serine Modulates Substrate Channeling in Tryptophan Synthase: A Novel Intersubunit Triggering Mechanism. *J. Biol. Chem.* **1991**, *266* (13), 8020–8033.

(113) Dunn, M. F.; Aguilar, V.; Brzović, P.; Drewe, W. F.; Houben, K. F.; Leja, C. a; Roy, M. The Tryptophan Synthase Bienzyme Complex Transfers Indole between the Alpha- and Beta-Sites via a 25-30 A Long Tunnel. *Biochemistry* **1990**, *29* (2), 8598–8607, doi:10.1021/bi00489a015.

(114) Ventura, E. M. R. M. R.; Williams, M. M. R. M. R.; Wood, J. Solutions of the Diffusion Equation in Cones and Wedges. *Ann. Nucl. Energy* **1988**, *15* (4), 191–199, doi:10.1016/0306-4549(88)90012-6.

(115) LANE, A. N.; KIRSCHNER, K. The Catalytic Mechanism of Tryptophan Synthase from Escherichia Coli Kinetics of the Reaction of Indole with the Enzyme—L-Serine Complexes. *Eur. J. Biochem.* **1983**, *129* (3), 571–582, doi:10.1111/j.1432-1033.1983.tb07087.x.

(116) Storer, B. A. C.; Cornish-bowden, A.; Box, P. O.; Birmingham, B. The Kinetics of Coupled Enzyme Reactions. *Biochem J* **1974**, *141*, 205–209.

(117) Trujillo, M.; Donald, R. G. K.; Roos, D. S.; Greene, P. J.; Santi, D. V. Heterologous Expression and Characterization of the Bifunctional Dihydrofolate Reductase-Thymidylate Synthase Enzyme of Toxoplasma Gondii. *Biochemistry* **1996**, *35* (95), 6366–6374, doi:10.1021/bi952923q.

(118) Biradar, A. V; Patil, V. S.; Chandra, P.; Doke, D. S.; Asefa, T. A Trifunctional Mesoporous Silica-Based, Highly Active Catalyst for One-Pot, Three-Step Cascade Reactions. *Chem. Commun.* **2015**, *51* (40), 8496–8499, doi:10.1039/C5CC01694K.

(119) Yang, X.; Tang, H.; Cao, K.; Song, H.; Sheng, W.; Wu, Q. Templated-Assisted One-Dimensional Silica Nanotubes: Synthesis and Applications. *J. Mater. Chem.* **2011**, *21* (17), 6122, doi:10.1039/c0jm04516k.

(120) Li, J.; Liu, W.; Wang, J.; Rozen, I.; He, S.; Chen, C.; Kim, H. G.; Lee, H. J.; Lee, H. B. R.;

Kwon, S. H.; et al. Nanoconfined Atomic Layer Deposition of TiO2/Pt Nanotubes: Toward Ultrasmall Highly Efficient Catalytic Nanorockets. *Adv. Funct. Mater.* **2017**, *27* (24), 1–8, doi:10.1002/adfm.201700598.

(121) Anderson, K. S.; Miles, E. W.; Johnson, K. A. Serine Modulates Substrate Channeling in Tryptophan Synthase: A Novel Intersubunit Triggering Mechanism. *J. Biol. Chem.* **1991**, *266* (13), 8020–8033, doi:266(13):8020-33.

(122) Chavan, K. S.; Calabrese Barton, S. Simulation of Intermediate Channeling by Nanoscale Confinement. *J. Phys. Chem. C* **2018**, *122* (26), 14474–14480, doi:10.1021/acs.jpcc.8b01922.

(123) Yarin, A. L.; Yazicioglu, A. G.; Megaridis, C. M. Thermal Stimulation of Aqueous Volumes Contained in Carbon Nanotubes: Experiment and Modeling. *Appl. Phys. Lett.* **2005**, *86* (1), 013109, doi:10.1063/1.1844602.

(124) Tao, Y.; Muramatsu, H.; Endo, M.; Kaneko, K. Evidence of Water Adsorption in Hydrophobic Nanospaces of Highly Pure Double-Walled Carbon Nanotubes. *J. Am. Chem. Soc.* **2010**, *132* (4), 1214–1215, doi:10.1021/ja9091215.

(125) Alexiadis, A.; Kassinos, S. Molecular Simulation of Water in Carbon Nanotubes. *Chem. Rev.* **2008**, *30* (12), 5014–5034, doi:10.1021/cr078140f.

(126) Clark Ii, J. K.; Habenicht, B. F.; Paddison, S. J. Ab Initio Molecular Dynamics Simulations of Aqueous Triflic Acid Confined in Carbon Nanotubes. *Phys. Chem. Chem. Phys. Phys. Chem. Chem. Phys* **2014**, *16* (16), 16465–16479, doi:10.1039/c4cp01066c.

(127) Sansom, M. S. P.; Biggin, P. C. Biophysics: Water at the Nanoscale. *Nature*. Nature Publishing Group November 8, 2001, pp 156-157+159, doi:10.1038/35102651.

(128) Pascal, T. A.; Goddard, W. A.; Jung, Y. Entropy and the Driving Force for the Filling of Carbon Nanotubes with Water. *Proc. Natl. Acad. Sci. U. S. A.* **2011**, *108* (29), 11794–11798, doi:10.1073/pnas.1108073108.

(129) Hummer, G.; Rasaiah, J. C.; Noworyta, J. P. Water Conduction through the Hydrophobic Channel of a Carbon Nanotube. *Nature* **2001**, *414* (6860), 188–190, doi:10.1038/35102535.

(130) Rasaiah, J. C.; Garde, S.; Hummer, G. Water in Nonpolar Confinement: From Nanotubes to Proteins and Beyond. *Annu. Rev. Phys. Chem.* **2008**, *59* (1), 713–740, doi:10.1146/annurev.physchem.59.032607.093815.

(131) da Silva, L. B. Structural and Dynamical Properties of Water Confined in Carbon Nanotubes. *J. Nanostructure Chem.* **2014**, *4* (2), 104, doi:10.1007/s40097-014-0104-3.

(132) Striolo, A. The Mechanism of Water Diffusion in Narrow Carbon Nanotubes. *Nano Lett.* **2006**, *6* (4), 633–639, doi:10.1021/nl052254u.

(133) Arechederra, R. L.; Minteer, S. D. Complete Oxidation of Glycerol in an Enzymatic Biofuel Cell. *Fuel Cells* **2009**, *9* (1), 63–69, doi:10.1002/fuce.200800029.

(134) Yang, J. C.; Loewus, F. A. Metabolic Conversion of L-Ascorbic Acid to Oxalic Acid in Oxalate-Accumulating Plants. *Plant Physiol.* **1975**, *56* (2), 283–285, doi:10.1104/pp.56.2.283.

(135) Konings, W. N.; Lolkema, J. S.; Poolman, B. The Generation of Metabolic Energy by Solute Transport. *Arch. Microbiol.* **1995**, *164* (4), 235–242, doi:10.1007/BF02529957.

(136) Karousis, N.; Tagmatarchis, N.; Tasis, D. Current Progress on the Chemical Modification of Carbon Nanotubes. *Chem. Rev.* **2010**, *110* (9), 5366–5397, doi:10.1021/cr100018g.

(137) Berendsen, H. J. C.; van der Spoel, D.; van Drunen, R. GROMACS: A Message-Passing Parallel Molecular Dynamics Implementation. *Comput. Phys. Commun.* **1995**, *91* (1–3), 43–56, doi:10.1016/0010-4655(95)00042-E.

(138) Van Der Spoel, D.; Lindahl, E.; Hess, B.; Groenhof, G.; Mark, A. E.; Berendsen, H. J. C. GROMACS: Fast, Flexible, and Free. *J. Comput. Chem.* **2005**, *26* (16), 1701–1718, doi:10.1002/jcc.20291.

(139) Abraham, M. J.; Murtola, T.; Schulz, R.; Páll, S.; Smith, J. C.; Hess, B.; Lindahl, E. GROMACS: High Performance Molecular Simulations through Multi-Level Parallelism from Laptops to Supercomputers. *SoftwareX* **2015**, *1–2*, 19–25, doi:10.1016/J.SOFTX.2015.06.001.

(140) Pronk, S.; Páll, S.; Schulz, R.; Larsson, P.; Bjelkmar, P.; Apostolov, R.; Shirts, M. R.; Smith, J. C.; Kasson, P. M.; van der Spoel, D.; et al. GROMACS 4.5: A High-Throughput and Highly Parallel Open Source Molecular Simulation Toolkit. *Bioinformatics* **2013**, *29* (7), 845–854, doi:10.1093/bioinformatics/btt055.

(141) Hess, B.; Kutzner, C.; Van Der Spoel, D.; Lindahl, E. GRGMACS 4: Algorithms for Highly Efficient, Load-Balanced, and Scalable Molecular Simulation. *J. Chem. Theory Comput.* **2008**, *4* (3), 435–447, doi:10.1021/ct700301q.

(142) Bussi, G.; Donadio, D.; Parrinello, M. Canonical Sampling through Velocity Rescaling. *J. Chem. Phys.* **2007**, *126* (1), 014101, doi:10.1063/1.2408420.

(143) Parrinello, M.; Rahman, A. Polymorphic Transitions in Single Crystals: A New Molecular Dynamics Method. *J. Appl. Phys.* **1981**, *52* (12), 7182–7190, doi:10.1063/1.328693.

(144) Darden, T.; York, D.; Pedersen, L. Particle Mesh Ewald: An N·log(N) Method for Ewald Sums in Large Systems. *J. Chem. Phys.* **1993**, *98* (12), 10089–10092, doi:10.1063/1.464397.

(145) Hub, J. S.; De Groot, B. L.; Grubmüller, H.; Groenhof, G. Quantifying Artifacts in Ewald Simulations of Inhomogeneous Systems with a Net Charge. *J. Chem. Theory Comput.* **2014**, *10* (1), 381–390, doi:10.1021/ct400626b.

(146) Vega, C.; Abascal, J. L. F. Simulating Water with Rigid Non-Polarizable Models: A General Perspective. *Phys. Chem. Chem. Phys.* **2011**, *13* (44), 19663–19688, doi:10.1039/c1cp22168j.

(147) Berendsen, H. J. C.; Grigera, J. R.; Straatsma, T. P. The Missing Term in Effective Pair Potentials. *J. Phys. Chem.* **1987**, *91* (24), 6269–6271, doi:10.1021/j100308a038.

(148) Gowers, R.; Linke, M.; Barnoud, J.; Reddy, T.; Melo, M.; Seyler, S.; Domański, J.; Dotson, D.; Buchoux, S.; Kenney, I.; et al. MDAnalysis: A Python Package for the Rapid Analysis of Molecular Dynamics Simulations. *Proc. 15th Python Sci. Conf.* **2016**, No. Scipy, 98–105, doi:10.25080/majora-629e541a-00e.

(149) Michaud-agrawal, N.; Denning, E. J.; Woolf, T. B.; Beckstein, O. Software News and Updates MDAnalysis : A Toolkit for the Analysis of Molecular Dynamics Simulations. *J Comput Chem 32* **2011**, *32*, 2319–2327, doi:10.1002/jcc.

(150) Beckstein, O. GromacsWrapper., doi:10.5281/zenodo.17901.

(151) Einstein, A. Eine Neue Bestimmung Der Moleküldimensionen. *Ann. Phys.* **1906**, *324* (2), 289–306, doi:10.1002/andp.19063240204.

(152) Yeh, I. C.; Hummer, G. System-Size Dependence of Diffusion Coefficients and Viscosities from Molecular Dynamics Simulations with Periodic Boundary Conditions. *J. Phys. Chem. B* **2004**, *108* (40), 15873–15879, doi:10.1021/jp0477147.

(153) Kast, W.; Hohenthanner, C.-R. Mass Transfer within the Gas-Phase of Porous Media. *Int. J. Heat Mass Transf.* **2000**, *43* (5), 807–823, doi:10.1016/S0017-9310(99)00158-1.

(154) Mu, D.; Liu, Z. S.; Huang, C.; Djilali, N. Determination of the Effective Diffusion Coefficient in Porous Media Including Knudsen Effects. *Microfluid. Nanofluidics* **2008**, *4* (3), 257–260, doi:10.1007/s10404-007-0182-3.

(155) Kolesnikov, A. I.; Loong, C. K.; de Souza, N. R.; Burnham, C. J.; Moravsky, A. P. Anomalously Soft Dynamics of Water in Carbon Nanotubes. *Phys. B Condens. Matter* **2006**, *385-386 I*, 272–274, doi:10.1016/j.physb.2006.05.065.

(156) Noskov, S. Y.; Lamoureux, G.; Roux, B. Molecular Dynamics Study of Hydration in

Ethanol-Water Mixtures Using a Polarizable Force Field. *J. Phys. Chem. B* **2005**, *109* (14), 6705–6713, doi:10.1021/jp045438q.

(157) Malek, K.; Coppens, M. O. Knudsen Self- and Fickian Diffusion in Rough Nanoporous Media. *J. Chem. Phys.* **2003**, *119* (5), 2801–2811, doi:10.1063/1.1584652.

(158) Roy, S.; Raju, R.; Chuang, H. F.; Cruden, B. A.; Meyyappan, M. Modeling Gas Flow through Microchannels and Nanopores. *J. Appl. Phys.* **2003**, *93* (8), 4870–4879, doi:10.1063/1.1559936.

(159) Pérez-Hernández, G.; Schmidt, B. Anisotropy of the Water-Carbon Interaction: Molecular Simulations of Water in Low-Diameter Carbon Nanotubes. *Phys. Chem. Chem. Phys.* **2013**, *15* (14), 4995–5006, doi:10.1039/c3cp44278k.

(160) Koga, K.; Gao, G. T.; Tanaka, H.; Zeng, X. C. Formation of Ordered Ice Nanotubes inside Carbon Nanotubes. *Nature* **2001**, *412* (6849), 802–805, doi:10.1038/35090532.

(161) Mashl, R. J.; Joseph, S.; Aluru, N. R.; Jakobsson, E. Anomalously Immobilized Water: A New Water Phase Induced by Confinement in Nanotubes. *Nano Lett.* **2003**, *3* (5), 589–592, doi:10.1021/nl0340226.

(162) Maniwa, Y.; Kataura, H.; Abe, M.; Suzuki, S.; Achiba, Y.; Kira, H.; Matsuda, K. Phase Transition in Confined Water Inside Carbon Nanotubes. *J. Phys. Soc. Japan* **2002**, *71* (12), 2863–2866, doi:10.1143/JPSJ.71.2863.

(163) Finkelstein, Y.; Moreh, R.; Shang, S. L.; Wang, Y.; Liu, Z. K. Quantum Behavior of Water Nano-Confined in Beryl. *J. Chem. Phys.* **2017**, *146* (12), doi:10.1063/1.4978397.

(164) Matsuda, K.; Hibi, T.; Kadowaki, H.; Kataura, H.; Maniwa, Y. Water Dynamics inside Single-Wall Carbon Nanotubes: NMR Observations. *Phys. Rev. B* **2006**, *74* (7), 073415, doi:10.1103/PhysRevB.74.073415.

(165) Dalla Bernardina, S.; Paineau, E.; Brubach, J. B.; Judeinstein, P.; Rouzière, S.; Launois, P.; Roy, P. Water in Carbon Nanotubes: The Peculiar Hydrogen Bond Network Revealed by Infrared Spectroscopy. *J. Am. Chem. Soc.* **2016**, *138* (33), 10437–10443, doi:10.1021/jacs.6b02635.

(166) Köhler, M. H.; Bordin, J. R.; da Silva, L. B.; Barbosa, M. C. Structure and Dynamics of Water inside Hydrophobic and Hydrophilic Nanotubes. *Phys. A Stat. Mech. its Appl.* **2018**, *490*, 331–337, doi:10.1016/j.physa.2017.08.030.

(167) Hamon, M. A.; Hui, H.; Bhowmik, P.; Itkis, H. M. E. Ester-Functionalized Soluble Single-Walled Carbon Nanotubes. *Appl. Phys. A …* **2002**, *74*, 333–338.

(168) Liu, Y.; Hickey, D. P.; Minteer, S. D.; Dickson, A.; Calabrese Barton, S. Markov-State Transition Path Analysis of Electrostatic Channeling. *J. Phys. Chem. C* **2019**, *123* (24), 15284–15292, doi:10.1021/acs.jpcc.9b02844.

(169) Voter, A. F. INTRODUCTION TO THE KINETIC MONTE CARLO METHOD. In *Radiation Effects in Solids*; Springer Netherlands: Dordrecht, 2007; Vol. 235, pp 1–23, doi:10.1007/978-1-4020-5295-8_1.

(170) Lacis, A. A.; Schmidt, G. A.; Rind, D.; Ruedy, R. A. Atmospheric CO2: Principal Control Knob Governing Earth's Temperature. *Science (80-.).* **2010**, *330* (6002), 356–359, doi:10.1126/science.1190653.

(171) *NOAA*; Washington, DC, 2018.

(172) Chen, Y.; Li, C. W.; Kanan, M. W. Aqueous CO2 Reduction at Very Low Overpotential on Oxide-Derived Au Nanoparticles. *J. Am. Chem. Soc.* **2012**, *134* (49), 19969–19972, doi:10.1021/ja309317u.

(173) Hori, Y.; Wakebe, H.; Tsukamoto, T.; Koga, O. Electrocatalytic Process of CO Selectivity in Electrochemical Reduction of CO2 at Metal Electrodes in Aqueous Media. *Electrochim. Acta* **1994**, *39* (11–12), 1833–1839, doi:10.1016/0013-4686(94)85172-7.

(174) Hori, Y. Electrochemical CO_2 Reduction on Metal Electrodes. *Mod. Asp. Electrochem.* **2008**, *42* (42), 89–189.

(175) Gattrell, M.; Gupta, N.; Co, A. A Review of the Aqueous Electrochemical Reduction of CO2 to Hydrocarbons at Copper. *J. Electroanal. Chem.* **2006**, *594* (1), 1–19, doi:10.1016/j.jelechem.2006.05.013.

(176) Sen, S.; Liu, D.; Palmore, G. T. R. Electrochemical Reduction of CO2 at Copper Nanofoams. *ACS Catal.* **2014**, *4* (9), 3091–3095, doi:10.1021/cs500522g.

(177) Song, Y.; Peng, R.; Hensley, D. K.; Bonnesen, P. V.; Liang, L.; Wu, Z.; Meyer, H. M.; Chi, M.; Ma, C.; Sumpter, B. G.; et al. High-Selectivity Electrochemical Conversion of CO2 to Ethanol Using a Copper Nanoparticle/N-Doped Graphene Electrode. *ChemistrySelect* **2016**, *1* (19), 6055–6061, doi:10.1002/slct.201601169.

(178) Le, M.; Ren, M.; Zhang, Z.; Sprunger, P. T.; Kurtz, R. L.; Flake, J. C. Electrochemical Reduction of CO2 to CH3OH at Copper Oxide Surfaces. *J. Electrochem. Soc.* **2011**, *158* (5), E45, doi:10.1149/1.3561636.

(179) Loiudice, A.; Lobaccaro, P.; Kamali, E. A.; Thao, T.; Huang, B. H.; Ager, J. W.; Buonsanti, R. Tailoring Copper Nanocrystals towards C2 Products in Electrochemical CO2 Reduction. *Angew. Chemie - Int. Ed.* **2016**, *55* (19), 5789–5792, doi:10.1002/anie.201601582.

(180) Ju, W.; Bagger, A.; Wang, X.; Tsai, Y.; Luo, F.; Möller, T.; Wang, H.; Rossmeisl, J.; Varela, A. S.; Strasser, P. Unraveling Mechanistic Reaction Pathways of the Electrochemical CO 2 Reduction on Fe–N–C Single-Site Catalysts. *ACS Energy Lett.* **2019**, *4* (7), 1663–

1671, doi:10.1021/acsenergylett.9b01049.

(181) Bagger, A.; Ju, W.; Varela, A. S.; Strasser, P.; Rossmeisl, J. Single Site Porphyrine-like Structures Advantages over Metals for Selective Electrochemical CO2 Reduction. *Catal. Today* **2017**, *288*, 74–78, doi:10.1016/j.cattod.2017.02.028.

(182) Serov, A.; Robson, M. H.; Halevi, B.; Artyushkova, K.; Atanassov, P. Highly Active and Durable Templated Non-PGM Cathode Catalysts Derived from Iron and Aminoantipyrine. *Electrochem. commun.* **2012**, *22* (1), 53–56, doi:10.1016/j.elecom.2012.04.029.

(183) Serov, A.; Artyushkova, K.; Andersen, N. I.; Stariha, S.; Atanassov, P. Original Mechanochemical Synthesis of Non-Platinum Group Metals Oxygen Reduction Reaction Catalysts Assisted by Sacrificial Support Method. *Electrochim. Acta* **2015**, *179*, 154–160, doi:10.1016/j.electacta.2015.02.108.

(184) Pylypenko, S.; Mukherjee, S.; Olson, T. S.; Atanassov, P. Non-Platinum Oxygen Reduction Electrocatalysts Based on Pyrolyzed Transition Metal Macrocycles. *Electrochim. Acta* **2008**, *53* (27), 7875–7883, doi:10.1016/j.electacta.2008.05.047.

(185) Goodpaster, J. D.; Bell, A. T.; Head-Gordon, M. Identification of Possible Pathways for C-C Bond Formation during Electrochemical Reduction of CO2: New Theoretical Insights from an Improved Electrochemical Model. *J. Phys. Chem. Lett.* **2016**, *7* (8), 1471–1477, doi:10.1021/acs.jpclett.6b00358.

(186) Akhade, S. A.; Bernstein, N. J.; Esopi, M. R.; Regula, M. J.; Janik, M. J. A Simple Method to Approximate Electrode Potential-Dependent Activation Energies Using Density Functional Theory. *Catal. Today* **2017**, *288*, 63–73, doi:10.1016/j.cattod.2017.01.050.

(187) Liu, Y.; Fire, A. Z.; Boyd, S.; Olshen, R. A. Estimating Clonality. *J. Catal.* **2014**, *312*, 108–122, doi:10.1016/j.jcat.2014.01.013.

(188) Thommes, M.; Kaneko, K.; Neimark, A. V.; Olivier, J. P.; Rodriguez-Reinoso, F.; Rouquerol, J.; Sing, K. S. W. Physisorption of Gases, with Special Reference to the Evaluation of Surface Area and Pore Size Distribution (IUPAC Technical Report). *Pure Appl. Chem.* **2015**, *87* (9–10), 1051–1069, doi:10.1515/pac-2014-1117.

(189) Ustinov, E. A.; Do, D. D.; Fenelonov, V. B. Pore Size Distribution Analysis of Activated Carbons: Application of Density Functional Theory Using Nongraphitized Carbon Black as a Reference System. *Carbon N. Y.* **2006**, *44* (4), 653–663, doi:10.1016/j.carbon.2005.09.023.

(190) Hu, X. M.; Hval, H. H.; Bjerglund, E. T.; Dalgaard, K. J.; Madsen, M. R.; Pohl, M. M.; Welter, E.; Lamagni, P.; Buhl, K. B.; Bremholm, M.; et al. Selective CO2 Reduction to CO in Water Using Earth-Abundant Metal and Nitrogen-Doped Carbon Electrocatalysts. *ACS Catal.* **2018**, *8* (7), 6255–6264, doi:10.1021/acscatal.8b01022.

(191) Hjorth Larsen, A.; JØrgen Mortensen, J.; Blomqvist, J.; Castelli, I. E.; Christensen, R.; Dułak, M.; Friis, J.; Groves, M. N.; Hammer, B.; Hargus, C.; et al. The Atomic Simulation Environment - A Python Library for Working with Atoms. *J. Phys. Condens. Matter* **2017**, *29* (27), doi:10.1088/1361-648X/aa680e.

(192) Mortensen, J. J.; Hansen, L. B.; Jacobsen, K. W. Real-Space Grid Implementation of the Projector Augmented Wave Method. *Phys. Rev. B - Condens. Matter Mater. Phys.* **2005**, *71* (3), 1–11, doi:10.1103/PhysRevB.71.035109.

(193) Enkovaara, J.; Rostgaard, C.; Mortensen, J. J.; Chen, J.; Dułak, M.; Ferrighi, L.; Gavnholt, J.; Glinsvad, C.; Haikola, V.; Hansen, H. A.; et al. Electronic Structure Calculations with GPAW: A Real-Space Implementation of the Projector Augmented-Wave Method. *J. Phys. Condens. Matter* **2010**, *22* (25), doi:10.1088/0953-8984/22/25/253202.

(194) Henkelman, G.; Uberuaga, B. P.; Jónsson, H. Climbing Image Nudged Elastic Band Method for Finding Saddle Points and Minimum Energy Paths. *J. Chem. Phys.* **2000**, *113* (22), 9901–9904, doi:10.1063/1.1329672.

(195) Chan, K.; Tsai, C.; Hansen, H. A.; Nørskov, J. K. Molybdenum Sulfides and Selenides as Possible Electrocatalysts for CO 2 Reduction. *ChemCatChem* **2014**, *6* (7), 1899–1905, doi:10.1002/cctc.201402128.

(196) Rostamikia, G.; Mendoza, A. J.; Hickner, M. A.; Janik, M. J. First-Principles Based Microkinetic Modeling of Borohydride Oxidation on a Au(1 1 1) Electrode. *J. Power Sources* **2011**, *196* (22), 9228–9237, doi:10.1016/j.jpowsour.2011.07.042.

(197) Carroll, J. J.; Slupsky, J. D.; Mather, A. E. The Solubility of Carbon Dioxide in Water at Low Pressure. *J. Phys. Chem. Ref. Data* **1991**, *20* (6), 1201–1209, doi:10.1063/1.555900.

(198) Stegelmann, C.; Andreasen, A.; Campbell, C. T. Degree of Rate Control: How Much the Energies of Intermediates and Transition States Control Rates. *J. Am. Chem. Soc.* **2009**, *131* (23), 8077–8082, doi:10.1021/ja9000097.

(199) Takele Menisa, L.; Cheng, P.; Long, C.; Qiu, X.; Zheng, Y.; Han, J.; Zhang, Y.; Gao, Y.; Tang, Z. Insight into Atomically Dispersed Porous M-N-C Single-Site Catalysts for Electrochemical CO2reduction. *Nanoscale* **2020**, *12* (31), 16617–16626, doi:10.1039/d0nr03044a.

(200) Dumesic, J. A.; Rudd, D. F.; Aparicio, L. M.; Rekoske, J. E.; Trevino, A. A. *The Microkinetics of Heterogeneous Catalysis*; ACS professional Reference Book: Washington, DC, 1993.

(201) Martinez, A. W.; Phillips, S. T.; Butte, M. J.; Whitesides, G. M. Patterned Paper as a Platform for Inexpensive, Low-Volume, Portable Bioassays. *Angew. Chemie - Int. Ed.* **2007**, *46* (8), 1318–1320, doi:10.1002/anie.200603817.

(202) Whitesides, G. M. The Origins and the Future of Microfluidics. *Nature* **2006**, *442* (7101), 368–373, doi:10.1038/nature05058.

(203) Nery, E. W.; Kubota, L. T. Sensing Approaches on Paper-Based Devices: A Review. *Anal. Bioanal. Chem.* **2013**, *405* (24), 7573–7595, doi:10.1007/s00216-013-6911-4.

(204) N. I. Andersen, K. Artyushkova, I. Matanović, D. P. Hickey, S. D. Minteer, P. A. Spectro-Electrochemical Microfluidic Platform for Monitoring Multi-Step Cascade Reactions. *ChemElectroChem* **2019**, *6*, 246–251, doi:10.1002/celc.201800578.

(205) Mendez, S.; Fenton, E. M.; Gallegos, G. R.; Petsev, D. N.; Sibbett, S. S.; Stone, H. A.; Zhang, Y.; López, G. P. Imbibition in Porous Membranes of Complex Shape: Quasi-Stationary Flow in Thin Rectangular Segments. *Langmuir* **2010**, *26* (2), 1380–1385, doi:10.1021/la902470b.

(206) Kronberg, R.; Lappalainen, H.; Laasonen, K. Revisiting the Volmer–Heyrovský Mechanism of Hydrogen Evolution on a Nitrogen Doped Carbon Nanotube: Constrained Molecular Dynamics versus the Nudged Elastic Band Method. *Phys. Chem. Chem. Phys.* **2020**, *22* (19), 10536–10549, doi:10.1039/C9CP06474E.